# Photoacoustic Technologies beyond Medical Imaging—PASA and LGFU

by

Qiaochu Li

A dissertation submitted in partial fulfillment
of the requirements for the degree of
Doctor of Philosophy
(Electrical Engineering)
in The University of Michigan
2019

Doctoral Committee:

Professor L. Jay Guo, Chair
Assistant Professor Somin Eunice Lee
Assistant Professor Becky Peterson
Professor Xueding Wang

Qiaochu Li

qiaochul@umich.edu

ORCID iD: 0000-0002-9042-4434

To my parents, Zhiwei Li and Dongmei Wang, for their selfless love, support and dedication

# Acknowledgements

First and foremost, I would like to express my deepest appreciation to my advisor, Professor L. Jay Guo, for his mentorship, guidance and consistent encouragement throughout my Ph.D. study. He has always been giving me the freedom in exploration of different topics and ideas and providing such a collaborative and intellectual environment in our group. I learnt not only the research methodologies but also critical thinking, positive attitudes and responsibilities from his mentorship. Without his continuous support, this dissertation would never have been possible. I would like to extend my gratitude to all my committee members, Professor Xueding Wang, Professor Somin Eunice Lee, and Professor Becky Peterson, for their suggestions and instructions. I would like to thank Professor Wang for his guidance for the photoacoustic spectrum analysis study, his meaningful instructions and insightful thoughts lead me into the biomedical fields for the first time. I am also grateful for Professor Somin Eunice Lee and Professor Becky Peterson for their great comments to this dissertation work.

I would also like to thank many of my current and previous colleagues in our group, for their inspiring discussion and help through my Ph.D. study. I would like to thank all my labmates Dr. Cheng Zhang, Dr. Taehwa Lee, Dr. Wei Luo, Dr. Hui Xia, Dr. Long Chen, Dr. Jaeyong Lee, Chengang Ji, Xi Chen, Zhenya Meng, Zeyu Lei, Dr. Ashwin Pandey, Yongbum Park, Weijie Feng, Yichun Zhang, Yeonjoon Cheong, Qingyu Cui, Jihun Lim, Sangeon Lee, Kaito Yamada, Tayebeh Sahraeibelverdi, and summer research intern

students Fangping Shi, Gang Yao, Zheng Miao, for sharing their great ideas in collaboration and discussions. Especially, I'd like to thank my mentors Dr. Cheng Zhang and Dr. Taehwa Lee, they have not only generously shared their research experience with me but also trained me with ways of creative thinking. I'd like to acknowledge the collaborations with Dr. Cheng Zhang on micro-ring projects, Dr. Taehwa on photoacoustic lens projects, Dr. Wei Luo and Dr. Hui Xia on LGFU treatment of eye blastoma, Fangping Shi, Gang Yao and Zheng Miao for their great work in developing micro-bubbles detection programs, and Yeonjoon Cheong, Zhenya Meng for their helpful suggestions in PA lens fabrication. In addition, I'd like to thank to the technical support of the Lurie Nanofabrication Facility (LNF), and all the staff and engineers for their tremendous support.

I would also like to thank my collaborators and friends outside our group, for their help in experiments and discussion. I would like to thank Dr. Hakan Demirci, Dr. Gary Fisher, Dr. Jefferey Orringer, for their help in LGFU treatment of eye oncology and acne; Dr. Harish Subbaraman for preparing inks for nozzle-free jetting experiments; Dr. Matthew Lynall for help through the I-Corp program; Dr. Ting Feng for her collaboration on the PASA project; Dr. Chao Tian for micro-ring PAM experiments, Xing Zhou for help on fiber hydrophone calibration, Ken Calderone in imaging and preparing for the histology sections, and Kaiwen Guo for generous help in providing help in experiments.

Last but not least, I would to express my sincere thanks to my family especially my parents my grandparents, and all my friends. Without my parents love and support, especially during my difficult time with study and life, I will never finish my Ph.D. study. I'd also

like to say thank you to all my friends who are always supportive and provide their help in and out of my study.

# Table of Contents

# List of Figures

# List of Tables

# Abstract

The Photoacoustic (PA) effect has been extensively studied as a direct and efficient light-to-sound conversion process. The majority of previous applications of the PA effect are focused on photoacoustic imaging, where the combination of optics and acoustics ensures both optical level resolution and large penetration depth into bio-samples. This thesis aims to explore the possibilities to applying the photoacoustic effects on other fields including non-imaging PA signal spectrum analysis, therapeutic treatment and nozzle-free jetting for printing.

First, in the case of fast and quantitative analysis of bio-samples, a non-imaging approach is preferable to analyze the spectrum of the PA signals. This is referred to as photoacoustic spectrum analysis. We have found a solid relationship between the morphological characteristics of the objects generating PA signals, and the polynomial fit of the measured spectrum of these PA signals. By measuring the signal with an ultra-broad-bandwidth ultrasound detector, we are able to characterize the size and shape of bio-samples in single cell level, paving the way for applications such as flow cytometry, cell counting, disease detection including blood diseases and blood freshness detection. Second, with the development of highly-efficient photoacoustic generation materials, PA transmitters that generate large amplitude, broadband and complex ultrasounds waveforms have been fabricated, extending the PA applications from pure imaging to therapeutic treatment and

other areas. Our PA transmitters are fabricated with simple and inexpensive ways compared with piezoelectric ceramic film fabrication used in conventional transducers or arrays. In this thesis, a self-focusing PA lens, made from candle soot (CS)/polydimethylsiloxane (PDMS) composite has been developed and applied in laser-generated-focused-ultrasound (LGFU). A Pulsed laser illuminates the PA lens to generate a tightly focused PA wave within an ellipsoid of 90μm (minor axis) * 200μm (major axis). Compared with previously developed PA generation layers made from carbon nanotubes (CNT) and metals, candle soot can be deposited with much lower cost and simplicity. Within the focal region, a negative pressure over 27MPa is achieved, which ensures steady bubble cavitation. We demonstrate one way to enhance this cavitation with the help of a superimposed low-frequency, low-amplitude ultrasound field, and get ~30% generation rate enhancement and ~60% cavitation bubble size enhancement. The energy released from bubbles collapse are used for ablation of bio-tissues or generation of thin and high-speed streams.

Taking advantages of these properties, LGFU equipped with CS/PDMS PA lens has been applied in two major areas: 1) Selective treatment, where the LGFU is used for direct ablation and dysfunction of the soft tissues less than 1mm. This treatment enjoys both selectiveness and accuracy and can treat each individual with his/her own need; 2) Nozzle-free jet printing, where the LGFU is used to generate ~10μm jets of materials with various viscosity and density. It has been demonstrated that the 2D materials like graphene and $MoS_2$ can be printed with resolution of ~200μm. This can be applied as a potential nozzle-free high-resolution patterning modality in flexible electronics.

# Chapter 1

# Introduction

## 1.1 Background

Photoacoustic effect is the formation of acoustic waves upon the absorption of modulated or pulsed light through thermoelastic expansion, material state change, dielectric breakdown, electrostriction and the radiation pressure [1]. Considering the thermoelastic expansion alone, it has been widely applied in medical imaging including both microscopy [2]and tomography [3], spectroscopy [4], photoacoustic spectrum analysis [5], material defect detection [6] and therapeutic treatment [7].

The photoacoustic imaging (PAI) combines the advantage of both optical imaging and ultrasound imaging. The contrast is provided by the optical absorbers, which ensures a good signal-to-noise ratio with no speckle noise. Through years of study, PAI has reached resolution of micrometer via microscopy setup—photoacoustic microscopy (PAM), and real-time 3D imaging with submillimeter resolution via tomography setup—photoacoustic tomography (PAT). In PAM, the lateral resolution is provided by the focal spot of the illumination beam, and the axial resolution is determined by the ultrasound detector bandwidth by $\frac{0.88*c}{\mathrm{BW}}$, where c is speed of sound and BW is the ultrasound detector's bandwidth [8]. It has been demonstrated that a lateral resolution of 2 μm by OR-PAM

system [9] and an axial resolution <3μm by using microring ultrasound sensor has been achieved in PAM setup [10]. The imaging depth of PAM can reach ~3mm [11] which exceeds most optical imaging modalities. Additionally, super-resolution systems have also been achieved via mechanisms such as flow-induced absorption fluctuations [12]. In PAT, the imaging depth and resolution are scalable and cover a range of cm to 100μm for the imaging depth and 200μm to several μm for the resolution [13]. The PAT system provides a much larger imaging depth and good enough resolution for 3D imaging. Both systems have been applied in vascular biology[14-17], oncology[18-25], neurology[26-30], ophthalmology[31-33], dermatology[34-37], gastroenterology [38] and cardiology [39] for imaging and diagnosis.

Non-imaging approaches include photoacoustic spectroscopy (PAS), photoacoustic spectrum analysis (PASA) and material defect detection. In PAS, the PA signals are scanned over a range of wavelengths and the corresponding spectra is being analyzed then with the help of spectrometer. It has been applied in depth profiling of mammalian cells [40] and characterizing of DNA-ethidium bromide interaction [41]. Photoacoustic spectrum analysis (PASA) evaluates the calculated acoustic spectrum of the PA signals and has been applied as a fast and quantitative method for cellular size tissue characterization. The idea is similar to the ultrasonic spectrum analysis [42], however, the acoustic spectrum obtained in PASA is directly related with the object itself rather than scattered ultrasound in the case of ultrasonic spectrum analysis. The spectrum of the PA signals contains morphology information including size and shape, moreover, it's not affected by the concentration of the samples. The defect detection is based on the PA

generation and the corresponding A-mode scan, where the PA were used as the high frequency ultrasound source, passing through the objects and got scattered at the defect. It has been demonstrated as a noncontact defect (~500 μm) detection method for drug tablets [43] and silicon wafer [6] .

Except for the imaging and analysis applications, PA waves also induces high pressure fields. By implementing an efficient light-absorbing and thermally expansive layer on a transparent substrate, PA transmitters that generate both broadband and high-amplitude ultrasound signals are fabricated. Some efficient materials include carbon-based materials like CNTs[44,45], candle soot [46], carbon nanofibers (CNFs) [47] and structural metals like silver [48] and gold [49]. Ultrasound imaging equipped with these PA transmitters ensures high resolution due to high frequency components in PA signals and good signal-to-noise ratio due to the large amplitudes. Besides, PA transmitters are able to create complex acoustic wavefront by spatially and/or temporally modulated excitation light via designing of the PA generation layer surface profiles. By using 3D printing [50], spin-coating, dip-coating [51], transmitters including self-focusing PA lens, optic-fiber PA transmitter, acoustic hologram mask [52] and arbitrary tailored optoacoustic surface have been developed. In the LGFU application, the PA lens made from a composite layer such as CS/PDMS is excited by a Nd: YAG 532nm pulsed laser the PA lens generates a highly-intense focused pressure field with negative peak exceeding the cavitation threshold, and the cavitation bubbles are consistently created within the focal point. This cavitation can also be enhanced by another low-amplitude, low-frequency ultrasound field. The energy released from the bubbles collapse have been used to ablate soft tissues non-invasively,

which is referred to as a cavitation-based therapy[53,54]. Compared with existing HIFU techniques using conventional focused ultrasound transducers arrays, LGFU device enjoys much better durability, simple and inexpensive fabrication, tighter focus and the therapy itself is free of thermal toxicity. At the meanwhile, the free-space optics is more compact and flexible. It has been demonstrated that the LGFU is capable of non-invasively and mechanically ablate the gelatin gel phantoms, organoids, pig eye pigment layer [55] and soft-tissues with a focal length of ~1cm. Moreover, equipped with PAT system as an imaging guidance, we propose to apply LGFU as a personalized and precise soft tissue ablation method.

It has also been demonstrated, that the LGFU system is able to jet a super-thin (~10μm) and high-speed (>100m/s) liquid streams including 2D materials such as graphene and $MoS_2$ and CNT solution. The thin stream suggests another high-resolution printing method for flexible electronics and the high speed suggests the potential to inject large molecules such as Botox, DNA, vaccines without a needle. LGFU is considered free of nozzle-clogging issues and can print the ink materials more efficiently at the same time.

## 1.2 Thesis outline

In this thesis, the related physical principles and mechanisms will be introduced first. Then the proposed PA related applications will be discussed, including the photoacoustic spectrum analysis, laser-generated-focused-ultrasound application in micron-level soft tissue ablation, and nozzle-free jetting. These altogether, it will extend the current PA-

based techniques in both non-imaging analysis and therapeutic applications that are not explored much before.

**Chapter 1** presents an introduction of the background and development of the current photoacoustic-related technologies, ranging from traditional imaging applications, non-imaging analysis and other applications such as LGFU, PA-assisted ultrasound imaging and defect detection. Also, the outline for the whole thesis is described here.

**Chapter 2, 3** presents the physics behind the related techniques and one way to enhance cavitation. The photoacoustic effect is introduced first, including the physical picture, the governing equation and parameters that can influence the PA generation efficiency. Afterwards, the focusing mechanism of PA lens and the fabrication process are described. And an initial demonstration of liquid PA lens is shown. Then the laser-generated-focused-ultrasound working principle as well as the cavitation threshold are described, which serves as the basics for both therapy application and jetting experiments. Simulations and analytical solutions of cavitation threshold are also described for a guidance in our experiments.

**Chapter 4** presents the principles and experimental results of PASA, which is used for characterization of microspheres and blood freshness. The working principle of microring and the experimental setup are described first, and then the spectrum analysis results of single microsphere, concentrated microspheres and blood cells are discussed.

**Chapter 5, 6** present the therapeutic and jet-printing applications of PA effect based on the technology LGFU equipped with the CS/PDMS PA lens. The intense pressure field in this region rupture the liquid and induce cavitation bubbles and bubble clouds, whose collapse will release mechanical energy to the surroundings to ablate tissues or to form high-speed and thin streams. These chapters will first start from introduction of related fields and how the LGFU solves the challenges of conventional approaches. Then the experimental setup and sample preparation are described. Afterwards, the experimental results will be discussed. At last, a conclusion and issues are discussed about.

**Chapter 7** will summarize the above techniques and discuss about the optimization of the systems and future works.

# Chapter 2

# Mechanisms and Working Principles

## 2.1 Introduction

This chapter will focus on the physics of photoacoustic generation, working principles of self-focusing photoacoustic transmitters—PA lens, and working principle of laser-generated-focused ultrasound technology as well as cavitation thresholds.

In solid and liquid, acoustic wave generation by light can be explained by five mechanisms: thermoelastic expansion[56-60], material state change[56,61], dielectric breakdown[62-66], electrostriction and the radiation pressure[67,68]. The first three processes occur at different levels of input light intensity. The thermoelastic expansion happens at any input light intensity, where the objects absorb light and convert to heat. The induced temperature gradient produces a strain which then releases a propagating acoustic wave in the medium. At a larger intensity, the material state change occurs, which is accompany with vaporization or ablation of liquid or solid materials. The ejection of the materials induces a recoil momentum that propagates as the acoustic wave. When the input light intensity reaches above ~ $10^{10}$ $W \cdot cm^{-2}$, dielectric breakdown will happen, and a plasma will form, which produces a shock wave propagating into the surrounding medium. Except for these three mechanisms, radiation pressure, electrostriction and Brillouin scattering are also

considered to contribute to photoacoustic generation depend on the absorbing layer properties and excitation source. For example, the momentum exchange while the photons hit onto a high-reflectivity metal surface will induce a radiation pressure, which is usually orders smaller compared to the thermal-elastically generated pressure. In liquids, a movement of atoms or molecules can induce electrostriction force, and an acoustic wave is generated due to the density gradient. Researchers also suggested another effect to take place during the photoacoustic effect, which is Brillouin scattering [64]. It's worth to note that the thermoelastic expansion, state change and dielectric breakdown have much larger generation efficiencies than the other three associate effects in terms of energy conversion efficiency and pressure amplitude in general.

Because the thermoelastic expansion induces PA signals linearly related with the optical absorption coefficient and input light intensity, most of the studies in photoacoustic imaging, photoacoustic spectroscopy and spectrum analysis rely on this generation mechanism. Though studies have shown that the material state change and the dielectric break down have higher light-to-sound energy conversion efficiencies than that of the linear thermoelastic expansion, however, in these cases, the ablation of the generation materials will occur, so there will be an inconsistency when doing the imaging or will damage the PA transmitters made of solid generation layer. Therefore, in most of the applications, the input light intensity is kept within the thermoelastic region. However, we did an initial study on the self-recoverable liquid lens by using liquid form PA generation materials. It generates PA waves by material state change and a higher PA generation

efficiency as well higher damage threshold were achieved. Moreover, it can generate shock waves at large optical power, which can be used as a shock-wave based therapy.

## 2.2 Photoacoustic effect

This section will focus on the mathematical model on thermoelastic expansion since it covers most of the applications of PA effects. The governing equation for the linear thermoelastic expansion in an inviscid medium is given by (when heat conduction is negligible) [69]:

$$\left(\nabla^2 - \frac{1}{v_s^2}\frac{\partial^2}{\partial t^2}\right) p(\boldsymbol{r}, t) = -\frac{\beta}{Cp}\frac{\partial H}{\partial t} \quad (1)$$

Where $p(\boldsymbol{r}, t)$ denotes the pressure at location $\boldsymbol{r}$ at time t, $v_s$ is sound speed, β is the thermal coefficient of volume expansion and $C_p$ is heat capacity. $H$ is the thermal energy converted per unit volume and per unit time, that is proportional to the absorbed optical fluence given by $H = \eta_{th}\mu_a\varphi$. Before diving into the analytical solution to the waveform, we can estimate the initial generate PA amplitude by

$$p_0 = \Gamma\eta_{th}\mu_a F \quad (2)$$

where $\mu_a$ is the optical absorption coefficient, F is the optical energy fluence and $\Gamma$ is dimensionless Grüneisen parameter $\Gamma = \frac{\beta v_s^2}{Cp}$. This estimation is only valid under thermal and stress confinement, where the illuminated light duration is much shorter than the thermal relaxation time a) $\tau_{th} = \frac{d_C^2}{\alpha_{th}}$, where $\alpha_{th}$ is the thermal diffusivity and $d_c$ is characteristic dimension of heated region, and b) stress relaxation time $\tau_s = \frac{dc}{v_s}$.

Under both confinements, the fractional volume expansion is given by the thermal expansion equation (generalized Hook's law) [69]

$$\nabla \cdot \boldsymbol{\xi}(\boldsymbol{r}, t) = -\kappa \cdot \Delta p(\boldsymbol{r}, t) + \beta \cdot \Delta T(\boldsymbol{r}, t) \quad (3)$$

Where the $\boldsymbol{\xi}(\boldsymbol{r}, t)$ denotes the medium displacement, $\Delta p \; and \; \Delta T$ represents local changes of pressure and temperature. The displacement is related with fractional volume change by $\nabla \cdot \boldsymbol{\xi}(\boldsymbol{r}, t) = dV/V$, where $V$ denotes local volume. [70] The total volume change can be expressed as the sum of the displacement of every element on the surface, so that $\delta \mathrm{V} = \mathrm{V}' - \mathrm{V} = \oint \boldsymbol{\xi} \cdot \boldsymbol{d}\mathrm{S}$. Due to the Gauss' theorem, $\delta \mathrm{V} = \int \nabla \cdot \boldsymbol{\xi} \boldsymbol{d}\mathbf{V}$. This shows the total change can be treated as the sum of local volume change, which is equal to the contents in the integral, therefore $\delta(d\mathrm{V}) = \nabla \cdot \boldsymbol{\xi} \boldsymbol{d}\mathbf{V}$, of each particle contained in the volume. Finally, we have $\frac{\delta(dV)}{d\mathrm{V}} = \nabla \cdot \boldsymbol{\xi}$. In our case, we use $V$ to denote local volume instead of the total volume. Then the fractional volume change $dV/V$ can be then expressed as

$$dV/V = -\kappa \Delta p + \beta \Delta T \quad (4)$$

where $\kappa$ is the isothermal compressibility, the left-hand is zeroed, then we have $p_0 = \Delta p = \beta * \Delta T/\kappa$ and the temperature change is given by $\frac{\eta_{th}\mu_a F}{\rho C v}$. Under these confinements, heat conduction and sound wave propagation are negligible during the laser heating, which in turn gives the largest PA amplitude and induces equation (2). In most applications, the excitation light source is nanosecond or even picosecond lasers, which naturally fulfills the above condition. Additionally, it's worth to note that this linear relationship between F, $\mu_a$ and the generated pressure is limited in discussion in thermoelastic region. Therefore, when state change happens, equation (2) will not be valid anymore. That is also true that the conversion efficiency cannot be infinite large when an infinite F is input to the system.

However, for PA generation layer made of solid material, we use the equation (2) as a guidance for material selection. In order to achieve larger PA generation efficiency in thermoelastic region, we need high optical absorbance, thermal expansion coefficient and smaller heat capacity.

To analyze the waveform of the generated PA wave, equation (1) is solved with the Green's function approach

$$\left(\nabla^2 - \frac{1}{v_s^2}\frac{\partial^2}{\partial t^2}\right) G(\boldsymbol{r}, t; \boldsymbol{r}', t') = -\delta(\boldsymbol{r} - \boldsymbol{r}')\delta(t - t') \tag{5}$$

the Green's function is defined here as the response to a spatial and temporal impulse source term $G(\boldsymbol{r}, t; \boldsymbol{r}', t') = \frac{\delta(\mathrm{t}-\mathrm{t}\prime-|\mathbf{r}-\mathbf{r}\prime|/\mathrm{vs})}{4\pi|\boldsymbol{r}-\boldsymbol{r}\prime|}$, which physically represents a response of a point absorber to step heating. It yields the pressure wave solution as

$$p(\boldsymbol{r}, t) = \frac{1}{4\pi v s^2}\frac{\partial}{\partial t}\left[\frac{1}{vs*t}\int d\boldsymbol{r}' p0(\boldsymbol{r}')\delta(\mathrm{t} - \frac{|\mathbf{r}-\mathbf{r}\prime|}{vs*t})\right] \tag{6}$$

For a thin PA generation layer (1D case), the analytical waveform is gate function assuming delta input excitation. A more generalized solution form can be estimated as $p(t) = \int f(c\tau - z)g(z)\,dz$, where τ represents the retardation time and z is the distance along the propagation direction, f(t) is the temporal heating function characterized by the laser pulse while g(z) is the characterized by light absorbers distribution. This solution does not only provide a good approximation, but also gives some insights into the photoacoustic generation. The convolution indicates that in the extreme case, thin absorbing layer and infinite short laser pulse will lead to a gate function, whereas a longer pulse (assuming Gaussian) or thicker layer, will gradually broaden the gate signal to a Gaussian form.

## 2.3 PA lens—A self-focusing PA transmitter

### *2.3.1 Focusing Mechanism*

With the development of high-intensity focused ultrasound (HIFU), many studies have been conducted on different schemes of generating focused ultrasound. A tightly focused pressure field is the most essential element in the HIFU technology, in order to induce either thermal effect or cavitation effect from the acoustic energy [70]. Three main approaches to achieve ultrasound focusing are self-focusing [71], focusing with phased arrays [72] and focusing with an external acoustic lens [73]. To fabricate conventional self-focusing ultrasonic transducers, either tens of micro-machined piezoelectric elements are micromachined onto a concave surface, or the entire transducing material, such as lead zirconate titanate (PZT), is made into a spherically-shaped thin film. The fabrication is usually complicated, and the transducing piezoelectric ceramics are fragile. To achieve smaller focus, the PZT film has to be fabricated thinner. For example, to generate a focus of 100μm, it requires the transducer center frequency to be ~tens of MHz, which requires a very thin PZT film to be fabricated. The fabrication will be even more complicated when arrays of transducing elements are required. On the other side, external acoustic lens for focusing of acoustic waves usually only works for a small acoustic frequency range and are usually bulky.

We developed a self-focusing PA transmitter with PA generation layer uniformly deposited on a concave optical lens. The fabrication is simple and low-cost. Each point on the concave surface is equal-distance to the sphere center—the focus. They can be considered coherently generators interfere constructively with each other and get amplified at the focus, so as to realize self-focusing of the PA wave. Notably, this focusing mechanism is

advantageous for broadband and pulsed PA signal because all the frequency components travel exact same distance, and altogether superimpose at the focus. While other focusing mechanisms such as linear transducer array, can only allow focusing of a narrow band of acoustic frequencies.

The initially generated monopolar PA wave in the far field ($z > D^2/4\lambda$), will transform into bipolar pulses due to diffraction[74,75]. This ensures the appearance of a negative tensile wave following the positive peak and provides the large enough pressure for cavitation threshold. The focal gain or the geometrical gain of the PA lens is measured as the ratio of focal pressure to the surface pressure. With a low-f number=0.61 PA lens, we are able to achieve focal gain of over 200 [76] built from carbon nanotube (CNT). With candle soot deposited on a concave BK7 glass lens, we achieve a focal region of an ellipsoid with major and minor axis of ~230 μm and ~90 μm, and a signal amplitude of ~40 MPa(+), -20MPa(-) at 7.5mJ/cm$^2$ fluence, which is comparable with the previous CNT lens with same light fluence input but much lowered fabrication cost.

### *2.3.2 Laser shadowgraph imaging system*

The laser shadowgraph imaging system is an imaging technique to visualize refractive index vibrations in transparent media such as water and glass [77]. The image contrast is provided by the illumination light and the object's shadow. It is also good for a guidance

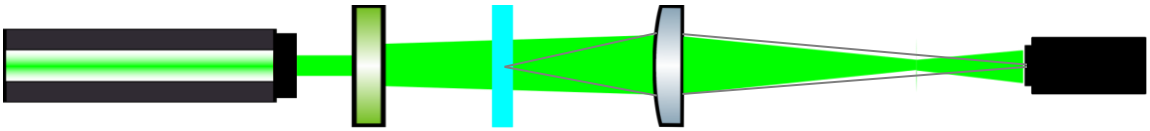

Figure 2-1: Schematic of laser shadowgraph imaging system

for alignment in elevational direction. The laser shadowgraph system in our setup is illustrated as below:

The system consists of a DPSS laser (Tech-527, Laser-export Co. Ltd), light diffuser, reflecting mirrors, object lens and a CCD imager. The CCD imager image the "shadow" of the opaque objects in the sample from the diffused light beam in the vertical plane. The wavefront of the ultrasound can also be visualized on the CCD imager because the intense ultrasound field modulates the refractive index of the water, then there will be a modulated reflection and scattering within the pressure field, which serves as the contrast to the surrounding transparent liquid. It is worth to note that the CCD imager and the laser are synchronized by a trigger generator with time step as small as 1ps. Therefore, by control the time delay of the two, it is possible to keep track of the transient events such as cavitation bubbles or liquid jetting.

### *2.3.3 Candle soot/PDMS lens fabrication and characterization*

Equation (2) derived in **2.2,** provides us an intuitive guideline of how to increase the generated PA signal amplitude. From the expression, we need to maximize the optical absorption coefficient, the thermal coefficient of volume expansion and minimize the heat capacity to generate a larger PA signal. It is difficult to achieve all these properties in one material; therefore, composite or structural metals are applied. Many studies have been conducted into making efficient PA generation layer, ranging from structural metal films including gold nanoparticle/polydimethylsiloxane (PDMS) composite, silver plasmon enhanced nanostructure, to carbon layers such as CNT/PDMS, CS/PDMS, Carbon nanofiber (CNF) composite and graphene oxide. Metal-based PA generation layer shows

a selective optical transmission and can be employed when specific band absorption is required. Such metal/dialectic or structured metal layer shows resonance effect rather than pure absorbing, in order to realize the narrow band selection. However, carbon-based materials have relative broad absorption band, so as its appearance of black and usually carbon material generates larger PA amplitudes.

In our case, we use carbon-based material due to its large optical absorption coefficient and broad band absorption. Carbon layer only provides good optical absorption but is expands little after heat absorption and it is easy to delaminate in water. Therefore, we use a carbon/PDMS composite layer to provide both large optical absorption and expansion coefficient. The absorbed light will transfer to heat and dissipate fast via the carbon into PDMS layer, which has a large thermal expansion coefficient. Among all the carbon materials, we've tested CNT and candle soot. To grow a good and uniform CNT layer, it's required to use PVD sputtering to grow a seed layer of Fe as the catalyst [78]. Afterwards, the Fe on the substrate will be put into a CVD furnace to grow the CNT through decomposition of C2H4. Then a PDMS layer is spin coated onto the substrate. Then the long cylindrical forms of multi-wall CNT are then embedded in the PDMS layer. This 2D thin and long cylindrical thermal conductors dissipate the heat very fast and realize good PA conversion efficiency. Similarly, the CS layer consists of connected 3D nanospheres also provides efficient heat diffusion. The fraction of the thermal energy η within these absorbers after the laser can be estimated as [7]

$$\eta = \frac{\tau_{HD}}{\tau_L} \cdot [1 - \exp(-\frac{\tau_L}{\tau_{HD}})] \quad (7)$$

where $\tau_{HD}$ and $\tau_L$(~6ns) are the heat diffusion time or the relaxation time and the laser pulse duration. In the CNT 2D cylinder case, $\tau_{HD} = d^2/16\chi$ [79], and in CS 3D sphere case, $\tau_{HD} = d^2/24\chi$ where $\chi$ is the thermal diffusivity of the surrounding medium ($\chi = 1.06 \times 10^{-7} m^2/s$ for PDMS), and $d$ is either CNT cylinder diameter, which is around 25nm, or CS nanospheres mean diameters, which is around 45nm. This leads to a relaxation time of ~0.4 ns for CNT and ~0.8 ns for CS. In CS case, the $\eta$ is calculated to be 0.13, meaning that 87% energy is transferred to the PDMS for expansion. Compared to the previously demonstrated CNT material of an 94% energy conversion efficiency, this is not degraded much, and moreover, the CS layer can be fabricated directly with a technique named flame synthesis. Basically, the CS is deposited on the substrate by putting the substrate in the flame, which is referred as flame synthesis deposition. Both materials demonstrate as great optical absorbers, however, compared to the fabrication complexity of CNT, the CS is employed here because of its simple fabrication process and low cost, at the same time, CS/PDMS maintains a similar level generation efficiency as the CNT/PDMS.

The flame synthesis mechanism is described as below:

The substrate is firstly hanged at some distance below the flame tip. During the reaction of O2 and hydrocarbons, heat are released, and a plasma flame will be formed. The heat vaporizes the liquid wax and breaks down the unreacted long chained hydrocarbons into small radicals such as C2, C3 C2H2. In the incomplete combustion, the six-membered aromatic rings will deposit onto the substrate because of its stability at high temperature, and these serve as the basic building unit of the later on nanospheres [80]. Therefore, the

CS layer is a layer of connected nanospheres, which dissipate heat as fast as the previous mentioned CNT long cylinders. From the SEM picture in Fig. 2-2(b), the connected nanospheres are of diameters of 30-50nm. The small sphere diameters and the large thermal conductivity of carbon ensure the heat to diffuse immediately into the PDMS surroundings upon light illumination. We also see a good infiltration of PDMS into the gaps between the connected spheres in Fig. 2-2(c). The thickness of CS layer can be easily controlled by adjusting the time of flame synthetic, usually in few seconds. We achieved the CS layer thickness from several hundreds of nm to around 5μm by varying the deposition time from 2s to 5s. However, it should be noted that uniformity is not ensured if a larger curved surface is used. In our case, the lens has a diameter of 1.5cm, which is similar to the flame diameter, therefore the uniformity of the deposited CS layer is good. Otherwise, CVD of MW-CNT or PDMS-CNT, PDMS-CNF solutions can be used as the alternative fabrication method to achieve uniform carbon layers for larger lenses.

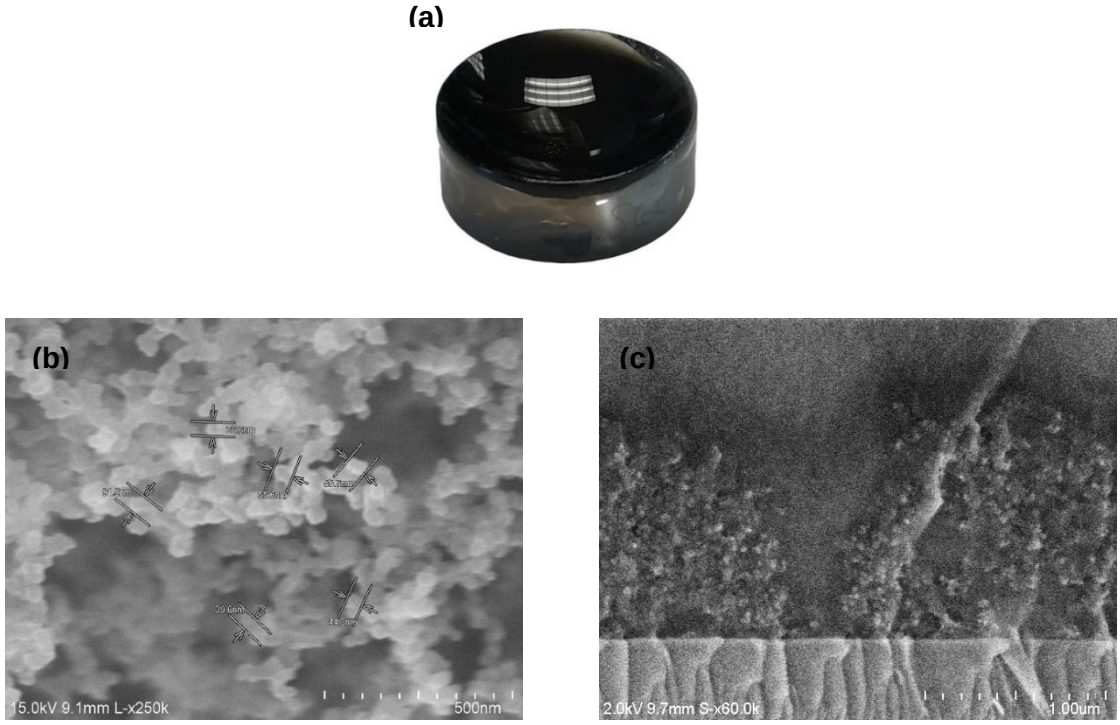

Figure 2-2:(a) CS/PDMS PA lens fabricated by flame synthesis. (b)SEM picture of carbon nanospheres deposited on glass substrate by flame synthesis. (c) The interface between the CS/PDMS composite layer and glass substrate, the vertical crack along the cleave edge is the evidence showing a good infiltration of the PDMS into CS layer

By using flame synthesis, the fabrication of this CS/PDMS lens is described as below: a BK7 glass concave lens (φ=15mm, concave surface radius=9.2mmm, Optosigma) was ultrasonic cleaned by IPA then Acetone. Then the lens was treated with O2 plasma in order to increase the adhesion of PDMS and the glass surface. Afterwards, the lens was hanged 2 mm below the fire tip for 4s in order to deposit a carbon layer of ~1.5 μm. Finally, a PDMS was poured on the carbon layer and spin-coated at 3000 rpm for 60s, and thermally cured for 20 min at 115 ℃, the fabricated PA lens is shown in Fig. 2-2(a). This CS/PDMS

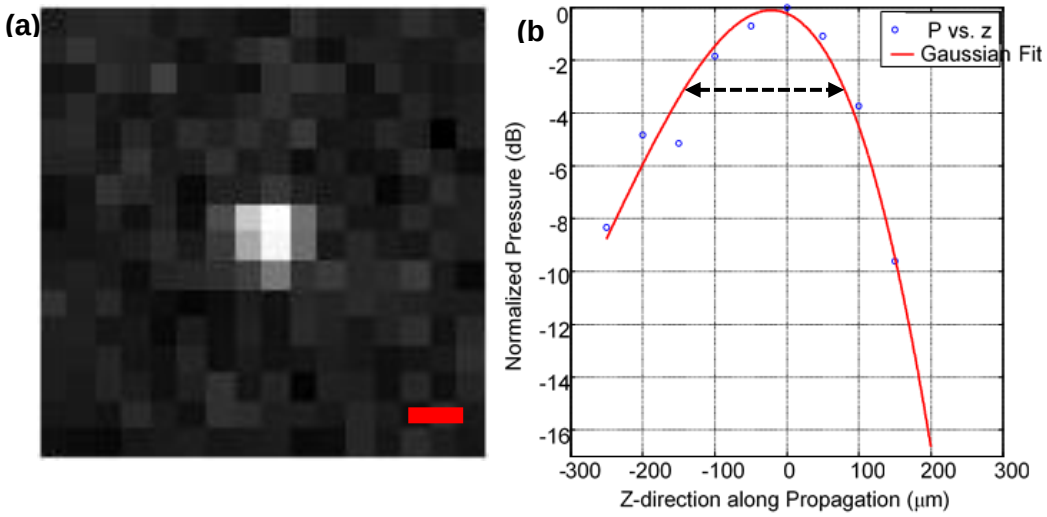


Figure 2-3: Characterization of the PA lens focal spot: (a) focused normalized pressure distribution in lateral plane, scale bar 100μm; (b) z-direction (along propagation) pressure distribution

layer generates a PA wave with frequency centered at 13MHz at the focal spot, and this is translated to a focal spot size estimated by $d = 1.27\lambda f\#$ . Taken into the speed of sound of 1500m/s in water at 25℃, f=13MHz, and f number of the lens to be 0.61, the focal spot diameter is estimated to be 89.39 μm, which is close to the measured lateral focal spot size of ~100 μm. The broadening is due to the contribution of other frequency components as well as the water attenuation which is $f^2$ dependent. A measured focal spot in both lateral

and perpendicular direction is shown in Fig. 2-3, by a calibrated fiber hydrophone [81] detector (The calibration is done by ONDA HNC-1500 hydrophone, ultrasound signal triggered by 5073PR) scanning over the focal plane, showing a focal ellipsoid ~100µm by 230µm, at -3dB. A focusing PA wave before focus and a free-space cavitation bubble shown in the Fig. 2-4 recorded by the shadowgraph.

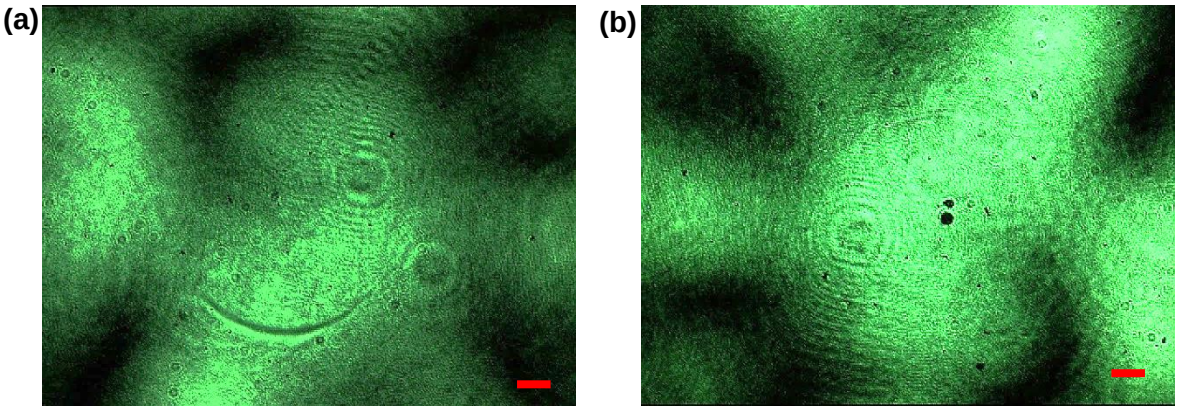


Figure 2-4: (a) Shadowgraph image showing the focusing photoacoustic wave and b) Free-space cavitation bubbles are generated within focal region, scale bar 100µm

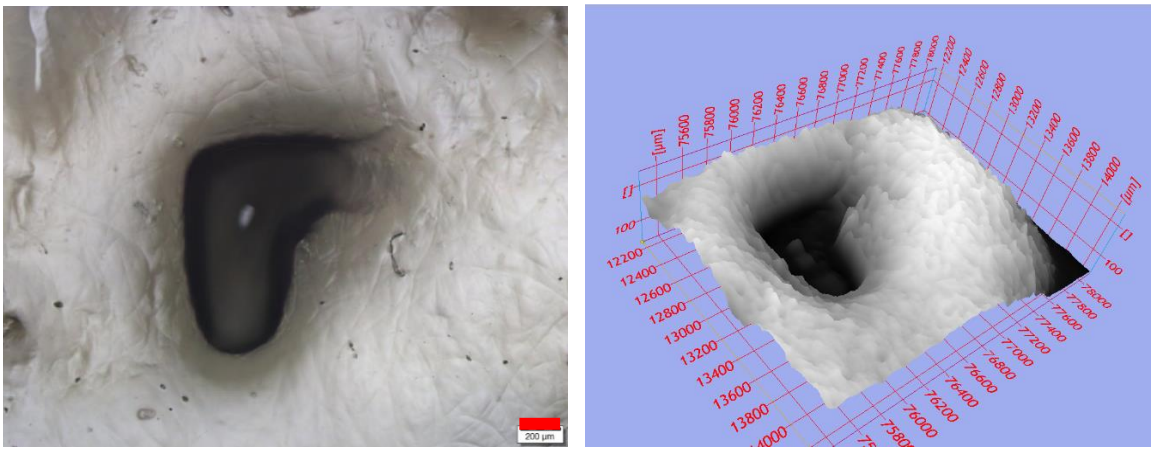

Figure 2-5: Ablated L-shaped pattern on gelatin gel phantom, imaged by Olympus BX51 microscope, BF, scale bar 200µm

To demonstrate the ablation effect, the focal point is scanned over a L-shaped pattern and a resultant depleted area is shown in Fig. 2-5. This proves a repeatable and accurate ablation effect of the PA lens. It should be note that, in the bio-tissue treatment, the cavitation threshold is higher rather than that in pure water [82].

As mentioned in **2.1**, the light-to-sound conversion can not only happen through thermoelastic expansion but can also occur when the material experiences a state change, where a recoil force will contribute in generating a pressure wave. It has been demonstrated that the conversion efficiency is higher than thermoelastic expansion alone and it is a non-linear activity. The advantage of using liquid material is not only because of a higher conversion efficiency, but also there exist no permanent damage for the generation layer. That is because the solid PA generation layers such as CS/PDMS or metal/PDMS will get ablated when the input light intensity is too large. In the case of liquid lens, some area of the liquid will be evaporated through boiling effect and some bubbles will be generated, however, while the bubbles are gone, the liquid generation layer will recover itself. Therefore, it is fair to say that the maximum generated PA signal will be larger since a larger input light intensity can be applied. Furthermore, by using a larger input laser power, that could damage the normal solid form PA generation layer, the liquid absorptive layer is able to generate a shock wave and can be used for shock-wave-based lithotripsy. We observed shock wave generated during the state-change PA generation, which can be applied to lithotripsy applications.

In the selection of the liquid absorbing material, carbon black particles(details) in acetone, water and sumi ink (Yasutomo Black Sumi Ink 12 oz, Yasutomo) were tested, where the sumi ink showed the best uniformity and generation efficiency. The ingredient in sumi ink is mainly carbon soot burned from pines and mixed in water, some binders are added for the uniformity. It is non-toxic and low cost.

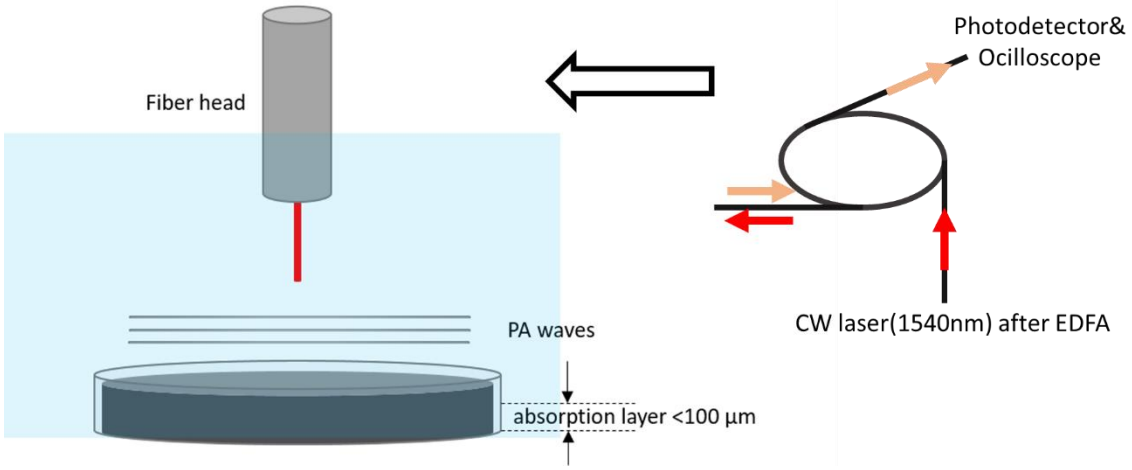


Figure 2-6: Schematic of fiber hydrophone ultrasound detection system and liquid PA material (sumi ink) generation of PA waves

To characterize the shock wave formation and the PA signal generation efficiency corresponding to different laser power, we sealed a thin layer of sumi ink in a cylindrical container with PVC plastic wrap film on the top. The PA signals were detected with the previously mentioned calibrated fiber hydrophone that can endure large pressure wave. The schematic of the experiment setup and the measured PA signals are shown below. It is worth to note that we demonstrated that the penetration depth of the sumi ink is <100μm, therefore, we can consider the generation layer is thinner than 100 μm rather than the actual depth of the cylinder. As shown in the Fig. 2-6, the fundamental working principle of fiber hydrophone is illustrated. A circulator is input at the first port of a CW laser of 1540nm,

amplified by an EDFA, then output to the next port. The output light will be connected to a cleaved fiber head and get reflected and output to the final port connected to photodetector. While the acoustic wave hit the fiber tip, the reflection coefficient will be changed due to the change of the water refractive index at the interface, therefore, the output signal will be related with the acoustic intensity.

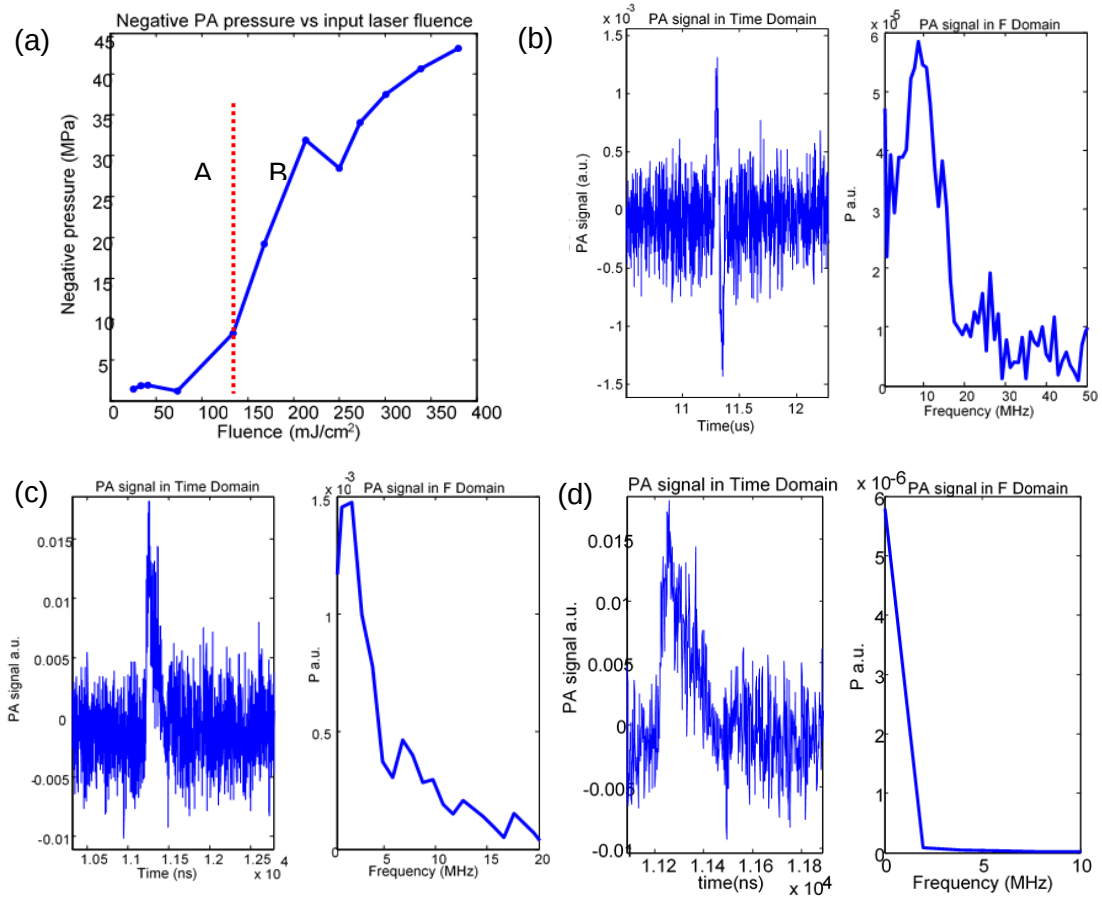


Figure 2-7: PA signal measured by fiber hydrophone: (a) Negative pressure of the sumi-ink material illuminated by 6ns laser pulse of different fluence. (b) PA signals in region A, the center frequency was at 8.8MHz, waveform showing bipolar shape. (c) PA signal at the red marked line, the center frequency was at 2MHz, waveform changed to monopolar, a shock front appeared. (d) PA signals in region B, center frequency was <1MHz, clear shock front appeared.

The PA signals generated by the sumi ink are divided into two regions, which corresponds to normal bipolar PA signal due to thermal elastic expansion and monopolar state change signal, where a shock front was observed. There are three main difference characterize the change: 1) the PA amplitude increases faster from region A to B, which is due to the larger generation efficiency of the state change mechanism than thermoelastic expansion; 2) Beyond the fluence of 134 mJ/cm$^2$, marked by the red dashed line in Fig. 2-7, an explosion sound would appear, which we understand as both recoil momentum force onto the bottom and the lower frequency components in the state change signals; 3) The waveform of the signals changed from bipolar to monopolar, and a sharp shock front appeared. When the phase change happens, the absorbed energy not only thermal expands the layer but continues to evaporate the liquid layer. This rapid evaporation of the bottom layer in the liquid pushes the fluids and transferred the momentum to the liquid layer, which counts for the positive pressure [1]. Therefore, we saw this phase change signal followed the first generated PA positive peak, and the negative peak of the diffracted PA signal is overwhelmed by this large positive pressure signal. This force will stop once the laser passes through the region and the temperature is lowered below the boiling point to support such motion. At the same time, the center frequency of the signal changed rapidly from 8.8MHz to 2MHz (at the dashed line) and gradually moved to lower frequency part to 1MHz. This explains the lower frequency components such as the explosion sound and matches with the spectrum of the shock wave, which is a broadband acoustic signal covers from DC to high frequency. In a conclusion, with large enough laser input, we can apply such liquid PA generation material in shock wave generation and extends the application of the PA lens.

For the liquid PA lens application, a cylindrical guide was put onto the concave lens to store the ink, then a plastic film is sealed at the top of the cylinder top opening, then this lens together with the container was immersed in water for ultrasound propagation. The laser-shadowgraph image showed a tight focal point from this ink lens. However, with the same laser fluence onto the liquid lens, the focused PA amplitude is 1/3 of that of CS/PDMS lens, which could be due to the larger attenuation when the PA wave propagates through the ink. The picture below shows the focusing spot and a small cavitation bubble generated, Therefore, in order to generate larger amplitude for the liquid PA lens, we need to decrease the ink layer thickness. It is worth to note that it doesn't reach the zone of phase change region because the light that illuminated the whole piece of PA lens was expanded for 25 times to cover the whole lens, therefore, the fluence decreased same amount accordingly. In order for further study on phase change PA lens, we will use a much higher power laser. But this initial test demonstrated the focusing capability of liquid PA lens.

Last but not least, we compare the sumi-ink liquid PA lens, CS/PDMS lens with previous CNT/PDMS lens and Cr/PDMS lens. Among those, the carbon-based material: CS/PDMS, sumi ink and CNT/PDMS shows a much larger PA generation efficiency. The liquid PA lens has the potential to generate the largest PA pressure because it more than 3-fold damage threshold for the 6ns laser and as stated before, it has larger generation efficiency when the laser fluence is high enough to achieve phase change. For the solid materials, the CS/PDMS can generate almost same level pressure compared with CNT/PDMS lens, moreover, it has much lower material cost and fabrication simplicity.

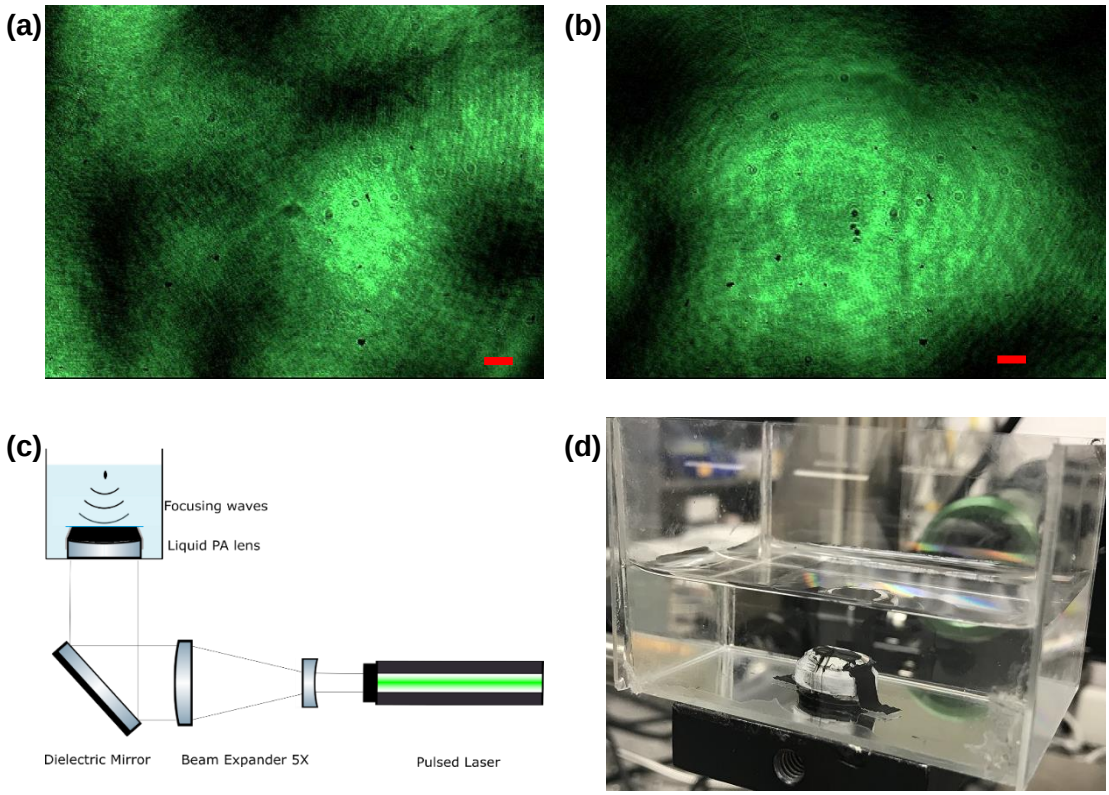


Figure 2-8: Shadowgraph imaging showing the focus spot of liquid PA lens at the center (a) and (b) cavitation bubbles generated slightly below the center of the image, scale bar 125μm, (c) scheme of liquid lens setup: an absorbing liquid is stored in a container on top of transparent concave glass lens, sealed by UV epoxy and plastic film, illuminated by expander pulsed laser from the bottom (d) photo shows the setup of the liquid PA lens

Table 2-1: Comparison of different generation layer of PA lens

| | Fabrication cost | Focus (ellipsoidal major and minor axis)/μm | PA generation efficiency MPa/mJ $cm^{-2}$ | Cavitation | Damage threshold for 6ns laser |
|---|---|---|---|---|---|
| CS/PDMS | Low | 90*230 | 1.34 | Y | <280mJ/$cm^2$ |
| CNT/PDMS [83] | High | 90*200 | 1.62 [84] | Y | <280mJ/$cm^2$ |
| Cr/PDMS [44] | High | N/A | 0.09 | N | <47mJ/$cm^2$ |
| Sumi ink liquid lens | Low | 100*200 | 0.62 | Y | N/A (we've tested up to 870mJ/$cm^2$) |

## 2.4 Laser-generated-focused-ultrasound and cavitation-based PA therapy

### *2.4.1 Laser-generated-focused-ultrasound technique*

With the help of focusing PA lens with CS/PDMS as the generation layer, we are able to generate and control cavitation bubbles within ~100μm. The technique that uses PA lens to focus acoustic wave and generate cavitation bubbles is referred here as LGFU. It is a non-invasive way to ablate soft bio-tissues with collapse energy from cavitation bubbles. We believe LGFU to become the counterpart of the existing HIFU techniques using piezoelectric transducers. The major advantage of this technology is the simple fabrication of the transmitter, ability to achieve focusing in submillimeter level, free of thermal toxicity and free-space optics setup.

Conventional therapeutic ultrasound treatment like HIFU is achieved either by coagulative thermal necrosis [85] due to the absorption of ultrasound energy during propagation or pure mechanical disintegration (or liquefy) of tissue by short and high amplitude ultrasound [86]. In the latter case, bubbles are generated near the treatment area either thermally by boiling histotripsy or non-thermally by negative pressure-induced cavitation. The cavitation-based histotripsy has proven the potential to successful treating of diseases such as disintegrate blood clots to relieve the thrombolysis [87], kidney stone liquification [88] and so on. However, current systems are targeting on a scale of mm, but some diseases related with glands, small vessels, or eye related operations require much tighter focus to avoid damage on the healthy neighboring tissues. To achieve tighter focus, a very thin piezoelectric ceramic layer is required in order to provide tighter focusing, and usually it cannot provide

a large amplitude at the same time to induce cavitation. As a result, the LGFU providing a much tighter focusing will be a good candidate in treating these diseases. Moreover, the cavitation-based therapy is free of thermal toxicity because the induced cavitation life-time is ~15 μs, therefore, not much heat is accumulated during each excitation pulse. The pain will be much reduced during the treatment. We have employed this technology in ablation in water-rich gelatin gel and demonstrate a fine cut on the gel phantom. Later on, we demonstrated an ablation effect on organoid made from hepatocyte cells. The ablation effect can be clearly seen from Fig. 2-9, that a cube area 0.8mm*0.8mm*0.8mm of cells were depleted in the organoids.

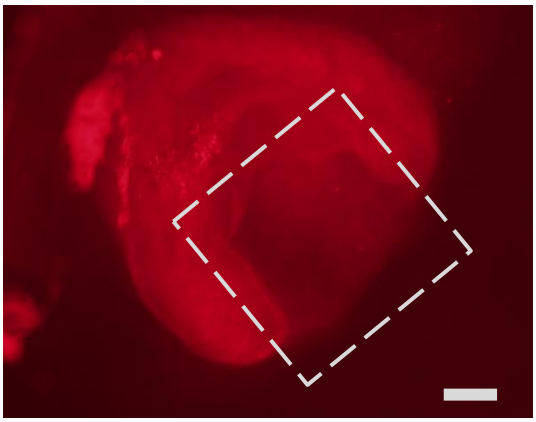

Figure 2-9: Fluorescent microscope image showing a depleted cube area of 0.8mm*0.8mm*0.8mm from the organoids, scale bar 200μm

*2.4.2 Cavitation*

A physical image of cavitation bubble formation can be illustrated by starting with the phase diagram of a water. In the phase diagram, phase change of liquid to gas occurs by crossing the curves of phase equilibrium, either due to temperature increase at fixed pressure (boiling) or pressure decrease at fixed temperature. The latter process is called

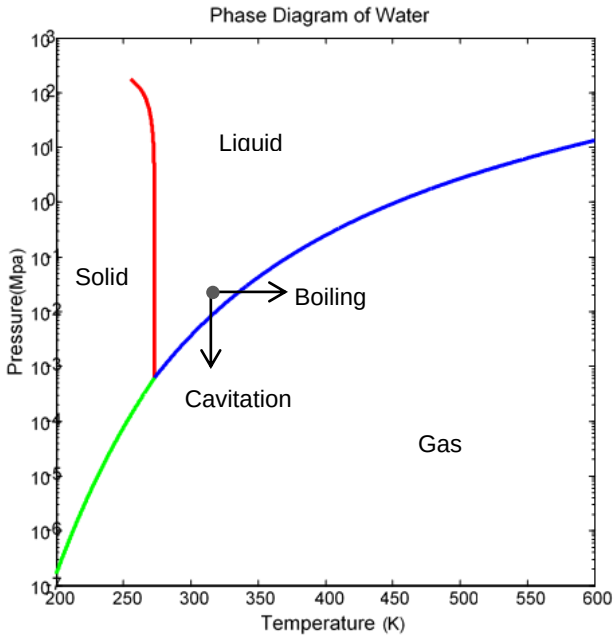


Figure 2-10: Phase diagram of water, equilibrium curves plotted from W. Wagner et al *[149]*.

cavitation. However, if we consider a pure water without any existing defects, it takes ~3GPa tensile pressure (negative pressure) to counteract the attractive force between two molecules. Experimentally, however, people found the cavitation happens just at tens of MPa or even lower. That is because there are always pre-existing bubble seeds and/or impurities in the liquid which lowers down the threshold. Cavitation nucleation starts from these minute sites through being excited by negative pressure. To understand the principles of bubble dynamics, people excite the bubble seeds, or these nuclei with a negative pressure pulse(usually a sinusoidal pulse with negative peak coming first) to study the cavitation nucleation. It simplifies this complex problem and make it possible to derive analytical

expression for threshold for cavitation. The motion of the wall of these bubbles during this pressure pulse can be described by the Rayleigh-Plesset equation[89-91], which is derived from conservation of mass and conservation of momentum, considering the viscosity, surface tension, and ambient pressure and the excitation pressure,

$$R\ddot{R} + \frac{3}{2}\dot{R}^2 = \frac{1}{\rho}\left((P_0 + \frac{2\sigma}{R_0})\left(\frac{R_0}{\mathrm{R}}\right)^{3\gamma} - \frac{2\sigma}{R} - \frac{4\mu\dot{R}}{\mathrm{R}} - P\infty\right) \quad (8)$$

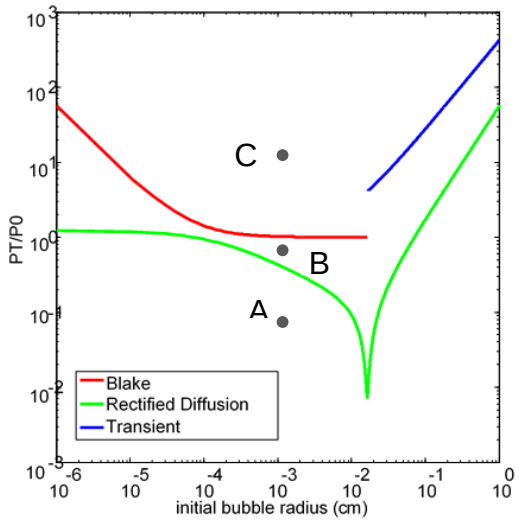


Figure 2-11: Cavitation thresholds diagram used to predict cavitation behavior, at pressure sinusoidal pulse of 20kHz frequency

where the R(t) is the radius of the bubble, dot represents the derivative to time, ρ is the fluid density, σ is the surface tension of the liquid, $R_0$ is the initial radius of the bubble and μ is the viscosity, $P\infty\,(t) = P0 + P(t)$ is the summation of ambient pressure and the external pressure and γ is the adiabatic coefficient. Assumptions are made here as:

1) Spherical bubble
2) Uniform gas distribution inside the bubble
3) Small compressibility

4) Gravity is neglected

5) And negligible vapor pressure inside

By solving this equation, we are able to describe how this cavitation nucleus grow and collapse after the excitation of the pressure pulse. The bubble seeds either get cavitated or die quickly after the external pressure field passes by. Once cavitated, depending on the bubble behaviors, it can be divided into stable cavitation and transient cavitation. These behaviors can be mapped to different regions separated by threshold curves in Fig. 2-11. The behaviors can be divided into three regions: transient cavitation above the red and blue curve; stable cavitation below the red, blue curve and above the green curve or the dead zone below the green curve. It should be note that there exists a resonant radius of the nuclei, where the excitation frequency matches the bubble size with $\rho{\omega_r}^2{R_r}^2 = 3\gamma P_0$ [92], threshold curves near this resonant zone are ill-defined. We first simulate the bubbles in the bottom zone of the diagram, e.g. point A ($P_A$=40kPa, $R_0$=10μm), where the bubbles excited by such pressure pulse described above cannot grow but oscillate around its original radius and died soon after the excitation, this "dead" behavior is described in Fig. 2-13(a). If the pressure amplitude of the excitation is increased to point B ($P_A$=80kPa, $R_0$=10μm), then it reaches the stable cavitation zone.

Stable cavitation bubbles oscillate around a specific equilibrium size in a relative stable manner. The threshold pressure or rectified diffusion for stable cavitation is characterized by the green curve in Fig. 2-11, which is defined by

$$P_B = P_0\left(\frac{3}{2}\left(1+\frac{2\sigma}{R_0P_0}-\frac{C_i}{C_0}\right)\left(1+\frac{2\sigma}{R_0P_0}\right)^{-1}\left((1-\frac{\omega^2}{{\omega_r}^2})^2+\left(\frac{b\omega}{\omega_r}\right)^2\right)\right)^{1/2} \qquad (9)$$

Basically, when the bubble oscillates, the outflow of the gas inside the bubble will overcome the inflow of the gas during one cycle, but the pressure field will compensate or reverse the effect. Therefore, once above the rectified diffusion threshold, the net flow of gas is inwards, and the bubble get grown. The bubbles in stable cavitation can grow and

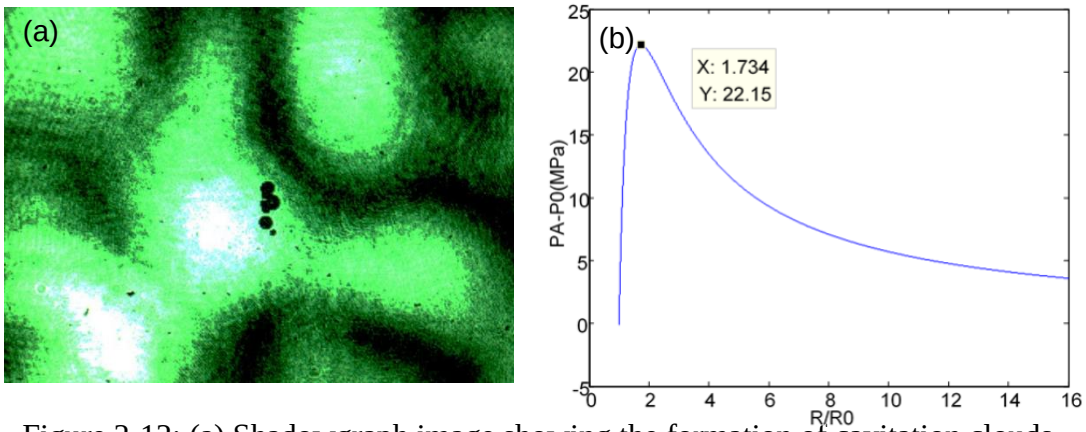


Figure 2-12: (a) Shadowgraph image showing the formation of cavitation clouds surrounding the focal region. (b) $P_A$-$P_0$ as a function of R when bubble growth is considered as a quasi-static process (e.g. Initial bubble seed sizes smaller than resonance diameter)

then oscillate with a radius larger than its original size, however, the collapse speed will never reach speed of sound, the size will not grow larger than 2.3R0 either, and the collapse will not complete meaning the radius cannot reach to a radius of 0. But it will oscillate at some stable frequency and last a few cycles. Stable cavitation is regarded as a relative stable behavior because no shock wave will be generated during collapse and the growth is not explosive. This behavior is described in Fig. 2-13(b).

If the excitation pressure is even higher, then the bubble reaches the transient cavitation, such as at point C ($P_A$=1MPa, $R_0$= $R_0$=10μm), and the behavior will be described with Fig. 2-13(c). The bubble will collapse to a radius of 0, and it will implode at the speed of sound, and the cavitation bubble generally exist for less than or around one period of the excitation pulse. The transient cavitation is regarded to have the most damage power to the

surroundings and is applied to the cavitation-based therapy. During the collapse of the transient cavitation bubbles, there always accompany both liquid jets and shockwaves. We take the advantage of the large shear force from the shock wave and utilize these to disintegrate the target tissue and utilize the liquid jet to realize nozzle-free printing and injection. Besides, the bubbles collapse into small bubbles have the chance to grow in a cycled motion—and cavitation clouds is then formed. Compared with single cavitation bubble, the clouds contain much larger energy and can ablate the bio-tissues more effectively, though the treatment region will be a little larger than the focal spot itself then, a bubble clouds around the focus is shown in Fig. 2-12.

The transient zone cavitation needs to be discussed careful. Small bubbles above Blake threshold [92] and larger bubbles above transient threshold are considered as transient cavitation. When the initial bubbles of interest are much smaller than the resonance frequency mentioned in the rectified diffusion, and the viscous and inertial effects are neglected because while R and $\dot{R}$ are small, the acceleration and viscosity terms are considerably small, so the incoming excitation pressure field can be treated as a static field during the bubble growth and the problem is regarded as a quasi-static problem. Therefore, the Rayleigh-Plesset equation is simplified to:

$$0 = \left(P_0 + \frac{2\sigma}{R_0}\right)\left(\frac{R_0}{\mathrm{R}}\right)^{3\gamma} - \frac{2\sigma}{R} - P\infty \tag{10}$$

Where $P\infty = P_0 - P_A$ and $\mathrm{P_A}$ is the amplitude of the applied negative pressure. Under the quasi-static situation, the bubble grows from one initial equilibrium state to another equilibrium state in a gentle behavior. Equation 10 leads to $\left(P_0 + \frac{2\sigma}{R_0}\right)\left(\frac{R_0}{\mathrm{R}}\right)^{3\gamma} = \frac{2\sigma}{R} + P_0 - P_A$ which relates the R (bubble radius of the achieved equilibrium state) and $P_A$. To find the

threshold of the external pressure for explosive growth for a bubble, we find the peak of R-$P_A$ curve, which is at $\frac{\partial(P_A-P_0)}{\partial R}$=0. Above this pressure, there is no equilibrium state(since no solution for R when excitation pressure is higher than this point) can be achieved, so we consider the pressure at this point as the cavitation threshold. This leads to $P_A - P_0 = \frac{4}{3R^*}$ and $R^* = (\frac{3{R_0}^3(P_0+\frac{2\sigma}{R_0})}{2\sigma})^{1/2}$as the critical radius. Above this pressure, the bubbles grow explosively. Expressing $P_A$ in terms of initial bubble size $R_0$, we define the Blake threshold pressure, which defines the "left boundary" of transient cavitation as

$$\frac{P_B}{P_0} = 1 + \frac{4}{9}X_B\left[\frac{3X_B}{4(1+X_B)}\right]^{\frac{1}{2}}, X_B = \frac{2\sigma}{P0R_B} \qquad (11)$$

The top-right side of the transient cavitation zone in Fig. 2-11 is defined by the transient threshold, where the bubble sizes are larger than resonance radius and we cannot ignore the inertial and viscous effect, therefore the pressure threshold for bubble growth $P_T$ and $R_{max}$ are constructed by solving equation (8), and this threshold is set when the maximum bubble radius size to be 2.3 times the original one, and this threshold is derived by Apfel as an explicit expression to estimate the transient behavior, described by [92-94]

$$R_0 = \frac{2}{3\omega}(\frac{P_A}{P_0} - 1)\left(\frac{2P_0}{\rho P_A/P_0}\right)^{1/2}\left(1 + \frac{2}{3}(\frac{P_A}{P_0} - 1)\right)^{1/3} \qquad (12)$$

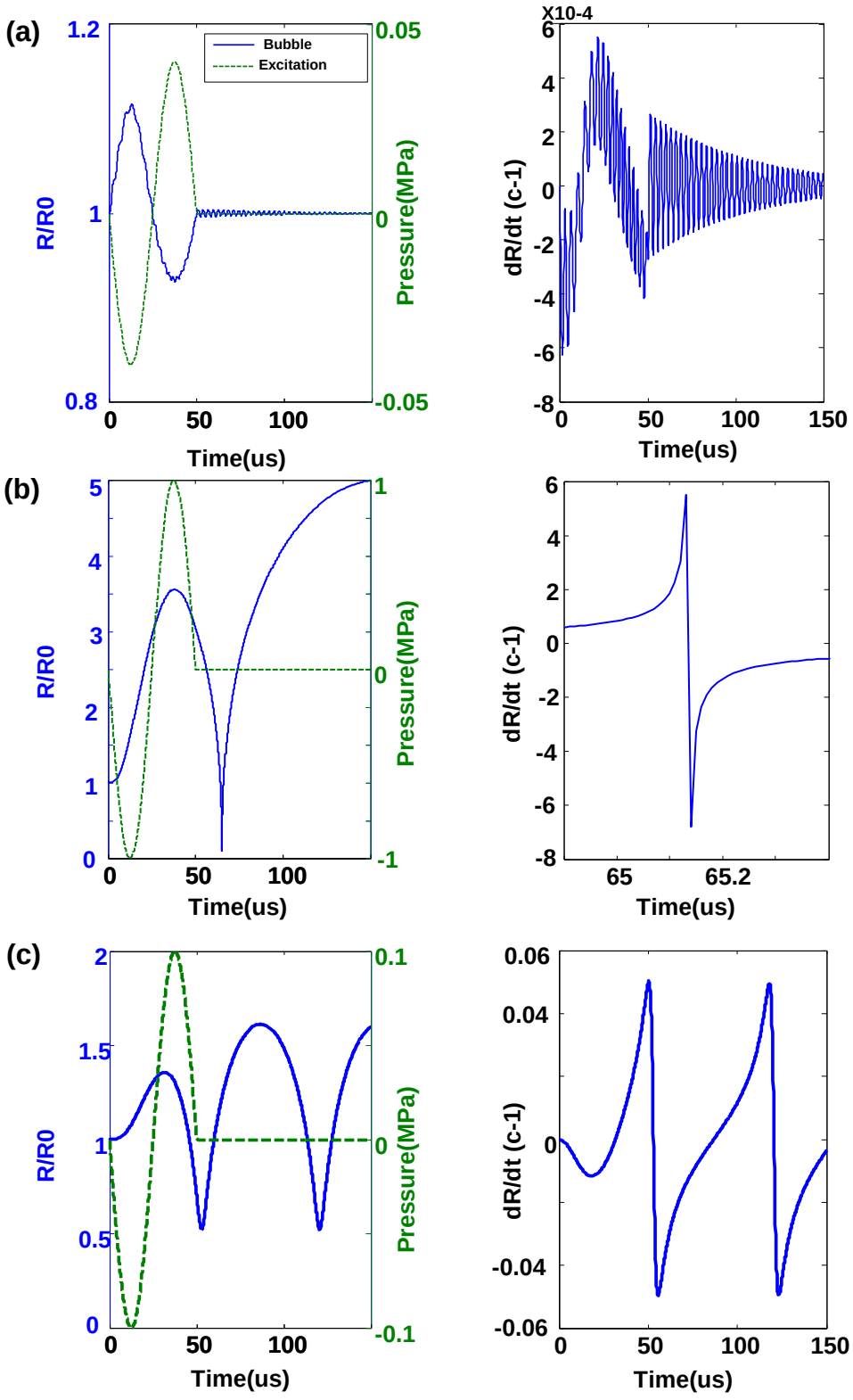


Figure 2-13: Bubbles wall radius and speed after excited by the sinusoidal pressure pulse at point A(a), B(b) and C(c).

where $P_A$ is the transient threshold pressure (negative peak) with respect to different nuclei diameter $R_0$. Additionally, we understand the main difference between the stable cavitation and transient cavitation is the maximum grown radius and the final collapse speed, which can be related with the acceleration dependence during the bubble collapse, that is $\ddot{R} = (-\frac{3\dot{R}^2}{2R} - \frac{4\mu\dot{R}}{\rho R^2}) + (\frac{1}{\rho R}\left((P_0 + \frac{2\sigma}{R}\right)\left(\frac{R_0}{\mathrm{R}}\right)^{3\gamma} - \frac{2\sigma}{R} - P\infty))$ , where the first term is speed dependent, called the inertial function which is highly depend on the bubble wall speed and the second term is called the pressure function because it's modified by the applied pressure only. From the figures below we can find that , during the collapse, the bubble wall speed of the transient cavitation is keep accelerating(and negative is inwards), because the inertial is always negative when speed is large enough and it dominates the second term, see Fig. 2-14(a); however in stable cavitation, when bubble collapse to a small radius, the inertial term becomes positive and the summation is then positive, stop the fast shrinking, see Fig. 2-14(b). And by plotting the negative pressure versus the bubble wall speed and the final bubble radius, we can see the collapse speed reaches speed of sound (1c) almost at the same pressure that enlarge the bubble to $2.3R_0$, which confirms the statement by Apfel in Fig. 2-13(c).

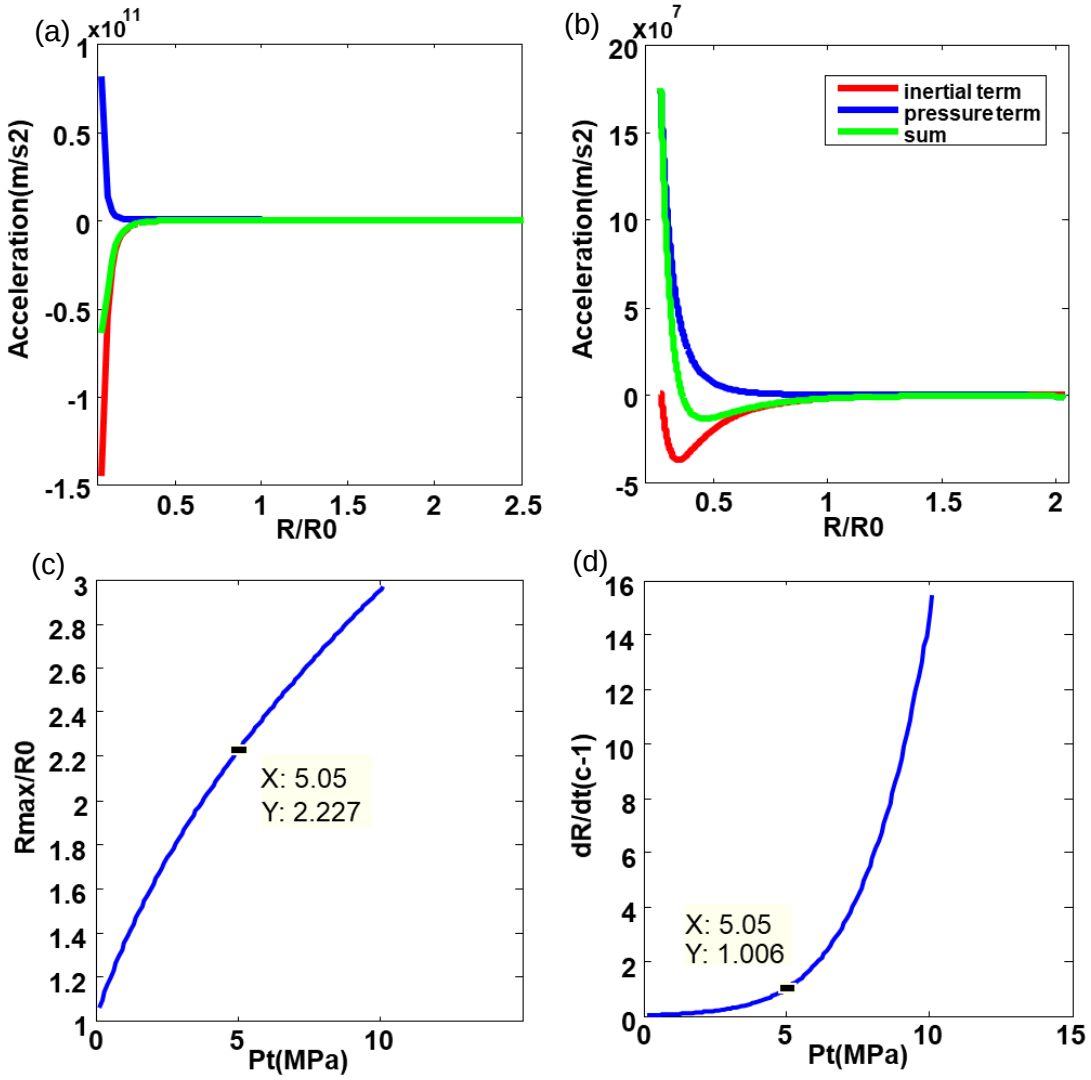


Figure 2-14: Acceleration during the bubble collapse in transient cavitation and stable cavitation (a) for point C, (b) for point B. (c) Final bubble radius $R/R_0$ for different excitation pressure(negative). (d) Collapse speed dR/dt(normalized by speed of sound c) for different excitation pressure

According to our experience and the previous work in exploring cavitation threshold in water [95], we realize the cavitation in pure water at room temperature happened almost at

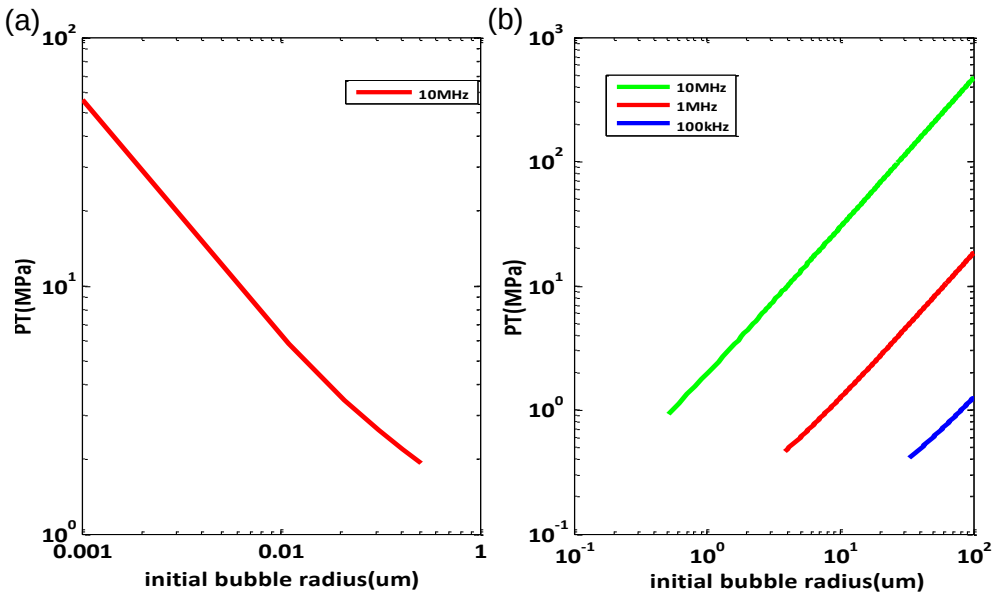


Figure 2-15: (a) Blake threshold at excitation ultrasound of 13MHz. (b) Transient threshold at different excitation pulse frequency.

similar pressure level of ~26-28MPa(negative pressure) regardless of the excitation frequency—which means the threshold is frequency-independent, which complies with the Blake threshold introduced before. It is understandable that the Blake threshold is independent of the excitation pressure frequency since a quasi-static problem is considered; while the "right boundary" is frequency dependent because when solving the Rayleigh-Plesset equation, higher frequency pulses spends less time for pulling, thus the max radius is smaller. Therefore, the right-side boundary set for the bigger bubbles are highly frequency dependent, see Fig. 2-15(b), the threshold could be orders higher for high frequency pressure pulse. Therefore, it is reasonable to assume most of the bubble seeds in water are assumed to be nm to tens of nm sizes, much smaller than the resonance radius for 13MHz (~180nm). Therefore, we focus our study in the left side of the diagrams of Fig. 2-11, which is plotted in Fig. 2-15 (a), set for excitation pressure of 13MHz. Our observed cavitation threshold of 26MPa corresponds to initial bubbles size in Blake estimation of 2.63nm. For the following discussion in Chapter 3.

## 2.5 Summary

This chapter mainly discussed about the physics of photoacoustic generation, the self-focusing PA transmitter, basic principles of LFGU and cavitation bubble generation mechanisms. It also includes a study of the liquid PA lens and using a low frequency ultrasound to improve the cavitation probability. These principles will serve as the fundamental support for exploring the further application either in PASA, acne treatment, nozzle-free printing and other potential applications.

# Chapter 3

# Cavitation Enhancement by Low-frequency, Low-amplitude Ultrasound

## 3.1 Introduction

Laser-generated-focused-ultrasound (LGFU) has been demonstrated as a micron-level ablation method using cavitation effect, with a lateral resolution of <100um and an axial resolution ~200um [55]. Such high accuracy opens the possibility of applying cavitation therapy towards malignant tissues in complex organs such as eyeball, skin glands and capillaries. Compared with traditional high-intensity focused ultrasound(HIFU), cavitation method is free of thermal lesions [82], truly non-invasive [96], and is compatible with ultrasound imaging techniques. One current challenge with LGFU induced cavitation is that the for some bio-tissues, especially tissues with fewer water contents, have higher cavitation threshold than that of aquatic environment [95]. This impedes the ablation effect due to inefficient cavitation and limits the treatment speed. Several methods have been explored to enhance the cavitation, including injection of gold nano-particles that provides heterogeneous cavitation nuclei [97]; microbubble injection [98]; or by optical heating of the medium [99]. These methods either undermine the non-invasiveness nature or is limited by optical dispersion depth in bio-tissues. *Baac et al* found that by imposing a 7.5MPa with lower-frequency tensile pressure on LGFU focus could enhance the generation rate of

cavitation bubbles [44]. Meanwhile, the cavitation zone was still confined within the tight focus of LGFU. In this work, we demonstrate that by providing much low-frequency ultrasound field as low as ~1MPa (negative peak), referred as assisting ultrasound (AU), the cavitation generation rate can still be effectively enhanced. Secondly, the cavitation bubble sizes under AU field are larger and this implies more mechanical energy stored. Both enhancements lead to larger ablation efficiency. Thirdly, we simulate the bubble dynamics of LGFU-induced cavitation with Rayleigh-Plesset(R-P), and qualitatively explain the enhancement. Finally, we explored the AU frequency, amplitude influence on the cavitation enhancement. The study provides a better understanding of the LGFU induced cavitation and paves the way for further application in cavitation treatment.

## 3.2 Experiment

### *3.2.1 Experiment Setup*

The system consists of the LGFU, laser shadowgraph for cavitation visualization and the PZT transducer to provide AU field. LGFU subsystem consists of the CS/PDMS PA lens, the excitation pulsed laser (Nd: YAG, 6ns, Surelite I-20, Continuum), and the optics to expand the beam and direct the beam onto the PA layer from the bottom of the PA lens. The PZT transducer (Olympus A381S) provides 2.6MHz sinusoidal ultrasonic pulse with amplitude up to ~1.04MPa and is excited by the function generator and amplified by 50dB RF power amplifier. The laser shadowgraph is widely used for visualizing the refractive index difference in transparent media such as water and glass. The image contrast is provided by the object's silhouette. The laser shadowgraph sub-system consists of a DPSS

pulsed laser, zooming lens and the CCD camera, focuses on the plane of the LGFU foci. With the help of laser shadowgraph and delay generator, the two focused ultrasound is visually aligned overlapping with each other, and cavitation bubbles are captured in the field of view (FOV). The delay generator triggers the excitation source of PA lens, PZT transducer, the light source of CCD camera and exposure of the camera.

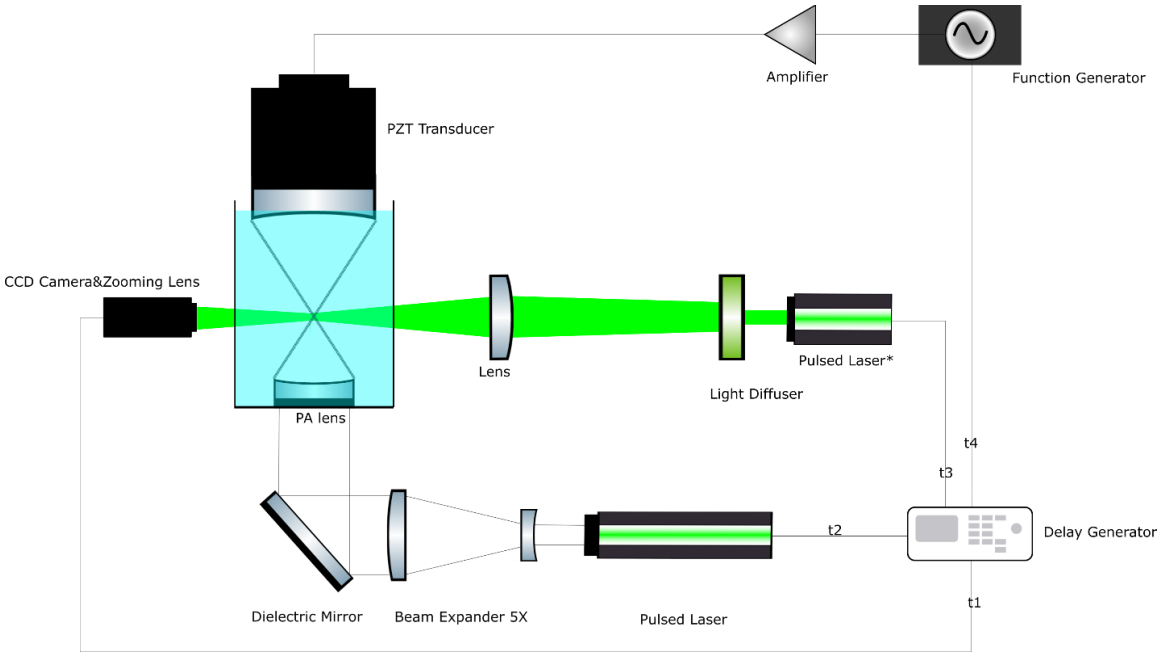


Figure 3-1: Schematic of the experiment setup

### *3.2.2 CS/PDMS PA lens and PZT characterization*

The CS/PDMS lens was characterized by a calibrated fiber-optic hydrophone which is widely used for intense pressure field or shock wave detection [81]. The LGFU focused pressure was calibrated up to 5mJ/cm$^2$ of excitation laser fluence. Similarly, the PZT transducer focused pressure was calibrated at voltages input 0-900mV (voltage measured out of the function generator).

### *3.2.3 Cavitation bubble characterization*

The cavitation bubbles were recorded with the camera continuously video for 30s (frame rate 20Hz). Deionized water was the medium for ultrasound propagation and cavitation generation at room temperature. The cavitation bubbles in the video are counted and sized by an OpenCV-written program based on adapted KNN background segmentation algorithm[100,101]. The program used machine learning approach and yielded satisfying result for the bubble counting. In addition, we also bring forward a method for counting overlapping bubbles that KNN cannot handle, a situation frequently encountered when bubbles are of larger sizes.

## 3.3 Results

### *3.3.1 Cavitation generation rate enhancement*

Firstly, we counted the cavitation bubbles generated within 30s video with and without the AU. The bubbles were counted at the moment right after the negative peak passed the focal point. It shows that with the AU applied (2.6MHz and amplitude 1.04MPa, sinusoidal pulse)

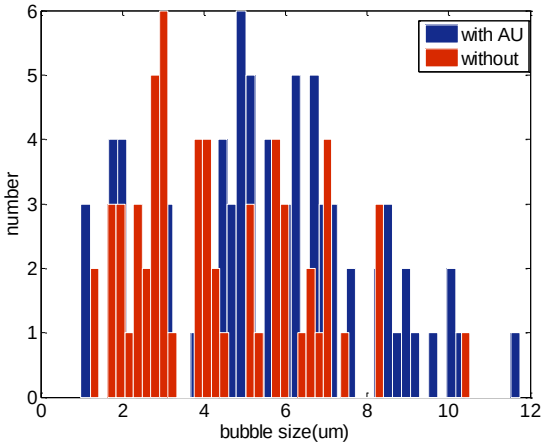


Figure 3-2: Counted bubbles with and without AU

more cavitation bubbles were generated. The video was taken at excitation laser fluence of ~13mJ/cm$^2$, at which the LGFU negative pressure peak was around ~27MPa. From the histogram, we found total bubble number increased by ~32%(from 61 to 81), which implies a lowered cavitation threshold was achieved with the AU overlapping with LGFU.

### *3.3.2 Cavitation bubble size enhancement*

We monitored the bubble size at different time after the nuclei was excited and characterized the max size at each time moment in the video with and without AU (2.6MHz and amplitude 1.04MPa, sinusoidal pulse). We found that the maximal size the bubble can reach (happened between 2μs to 3μs after excitation) increased when AU was applied, see Fig 3-3. Meanwhile, with larger-amplitude-AU, the size increase was larger. With 1.04MPa AU, the maximum size bubble can reach was improved 68% (at 3μs after nuclei excited), see Fig. 3-3(a); while with 0.7MPa AU, the improvement is 48% (at 2μs after nuclei excited), see Fig. 3-3(b). We measured the maximal size increase% at AU negative peak of 0.55MPa, 0.7MPa and 1.04MPa and find the positive effect of the AU amplitude on the increase, see Fig. 3-3(c). Moreover, from the bubble size data, it's clear to see the bubble's growth and collapse during the time range of the video. The results showed that even with an AU of ~0.5MPa, the size increase can be 10%.

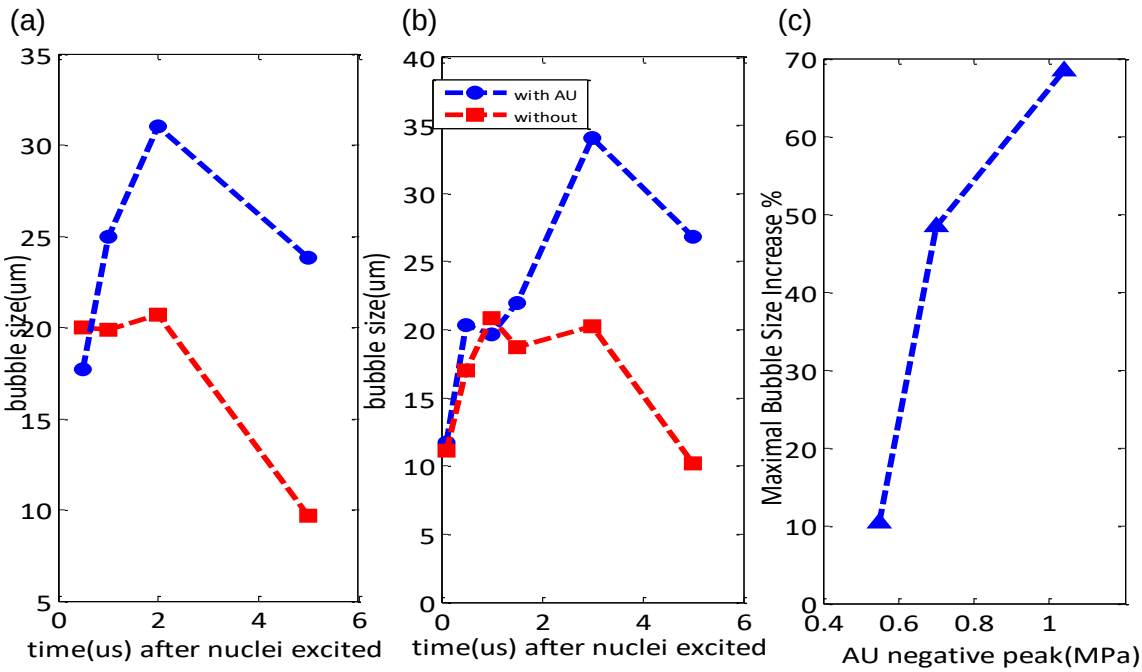


Figure 3-3: Bubble size at different time after nuclei is excited with and without AU of (a) 1.04Mpa, (b)0.7Mpa. (c) Maximal bubble size increase% versus the applied AU amplitude

## 3.4 Discussion

### *3.4.1 Simulation model*

In this section, we solve the Rayleigh-Plesset equation to simulate the cavitation enhancement while AU is applied on LGFU. The cavitation considered here is homogeneous cavitation, or cavitation from temporal and random bubble nuclei in the medium. This is a valid assumption since impurities or defects were never captured in any recorded videos. The dynamics of the bubbles can be described by solving the Rayleigh-Plesset equation [89] with Matlab ode45, which describe the bubble's response to transient pressure field.

$$R\ddot{R} + \frac{3}{2}\dot{R}^2 = \frac{1}{\rho}\left((P_0 + \frac{2\sigma}{R_0})\left(\frac{R_0}{\mathrm{R}}\right)^{3\gamma} - \frac{2\sigma}{R} - \frac{4\mu\dot{R}}{\mathrm{R}} - P\infty\right)$$

In which, $R$ is the bubble radius, dot represents the derivative to time, ρ is the fluid density, γ is the adiabatic coefficient, σ is the surface tension of the liquid, $R_0$ is the initial radius of the bubble nuclei and μ is the viscosity, $P\infty\,(t) = P0 + P(t)$ is the summation of ambient pressure and the excitation pressure pulse where $P(t)$ is the excitation pulse. In our case, $P(t)$ is the sum filed of LGFU and AU. Several assumptions are embedded in this equation to simplify the calculation: all bubbles are considered spherically-symmetric; there is uniform gas distribution inside the bubble; compressibility, gravity and vapor pressure are neglected inside the bubble.

We first simulate nuclei's response to pure LGFU, where the LGFU focus is approximated as two sequential temporal Gaussian pulses, see Fig. 3-4 (a). Fig. 3-4(b) and (c) show the bubble's response to the LGFU pulse with different negative peak, where the larger peak pressure makes the bubble grow explosively. Fig. 3-4(d) shows for a 2.5nm bubble nucleus, how the maximal size bubble can reach at different negative peak pressure and a critical pressure is found ~ -28.5MPa. Above this threshold, the bubble is able to expand more than $10^4$ original size(from initial 2.6nm to 27um) and collapse at supersonic speed (Mach number amplitude>1, Mach number is defined as the ratio of the bubble wall speed over sound speed, here positive sign refers the bubble is contracting, and negative sign refers to the bubble is expanding). This "turning point" found is set as the cavitation threshold in simulation. By locating these turning points, we simulated the threshold pressure of bubble nuclei of diameters from 1.5nm to 10.5nm and compared it with the Blake threshold in Fig. 3-4(e), where Blake threshold [92] is defined as

$$\frac{P_B}{P_0} = 1 + \frac{4}{9} X_B \left[\frac{3X_B}{4(1+X_B)}\right]^{\frac{1}{2}}, X_B = \frac{2\sigma}{P_0 R_B}$$

Both simulation and Blake thresholds shows exact same trend with an error of 27%. We understand this error is due to the fact that the Blake threshold is purely semi-static estimation.

Experimentally, the cavitation threshold of pure LGFU was determined whenever the probability of cavitation happens due to one excitation laser pulse is 50%, and the probability was fit in a sigmoid function introduced in previous study [76].

$$P(p\_) = \frac{1}{2}[1 + erf(\frac{p\_ - p_t}{\sqrt{2\sigma^2}})] \quad (13)$$

$P(p\_)$ is the probability of cavitation bubble occurrence at negative peak of $p\_$ , $p_t$ is the pressure at which the probability equals 50%. Each probability point was measured as the cavitation occurrence frequency in 20 excitation pulses. In this way, we found the threshold ~-27MPa in experiment, which corresponds to cavitation nucleus of 2.63nm in simulation model and the number is consistent with previous recorded measurement threshold for pure water at room temperature [16]. Therefore, in the following simulation, we will use 2.63nm as the averaged nuclei size and -27MPa as the cavitation threshold in this medium without further demonstration.

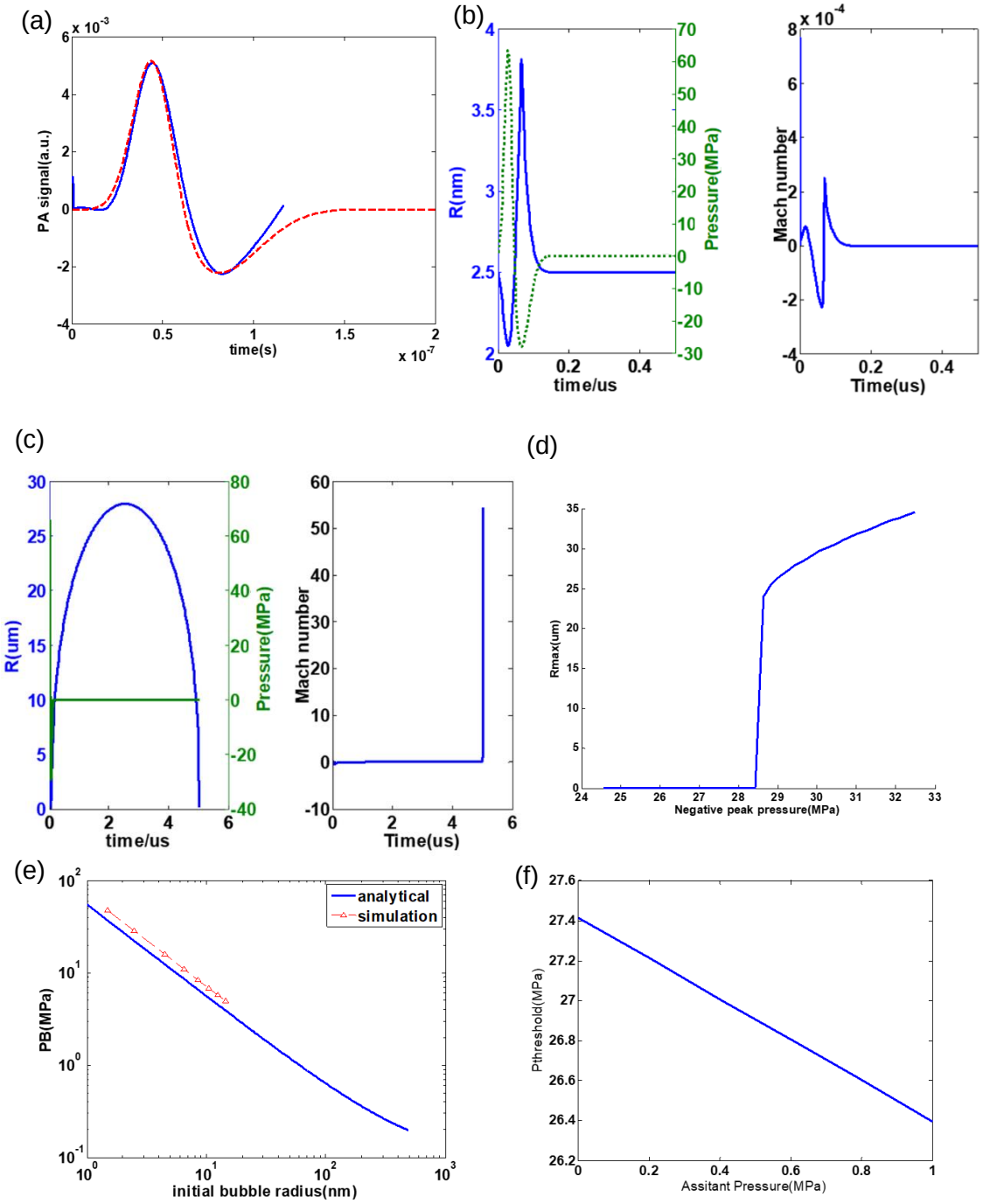


Figure 3-4: Simulation of homogeneous cavitation. (a)Excitation LGFU pulse approximation with two Gaussian pulses. Bubble radius and bubble wall speed(blue) after excitation(green) with excitation pressure (b) smaller than threshold or (c) larger than threshold. (d)Maximal radius the bubble can grow with LGFU excitation pulse of different negative peak pressure. (e) Cavitation threshold for different initial bubble radius by locating turning point in simulation(blue) and Blake threshold(red). (f)Cavitation threshold with AU of different amplitude applied

*3.4.2 Simulation vs Experiment*

When lower-frequency sinusoidal pulse is superposed onto the original LFGU, it both reduce the threshold pressure and increase the max bubble radius, so the cavitation rate(probability) and size increases. For the generation rate enhancement, we found in simulation that the pressure threshold is decreased linearly with respect to the AU amplitude, shown in Fig. 3-4 (f), and this manifest itself as the increase of cavitation occurrence probability. For example, in our case, assuming the averaged nuclei with size 2.63nm, we should expect cavitation threshold to be 27.15MPa. This pressure is fit on the

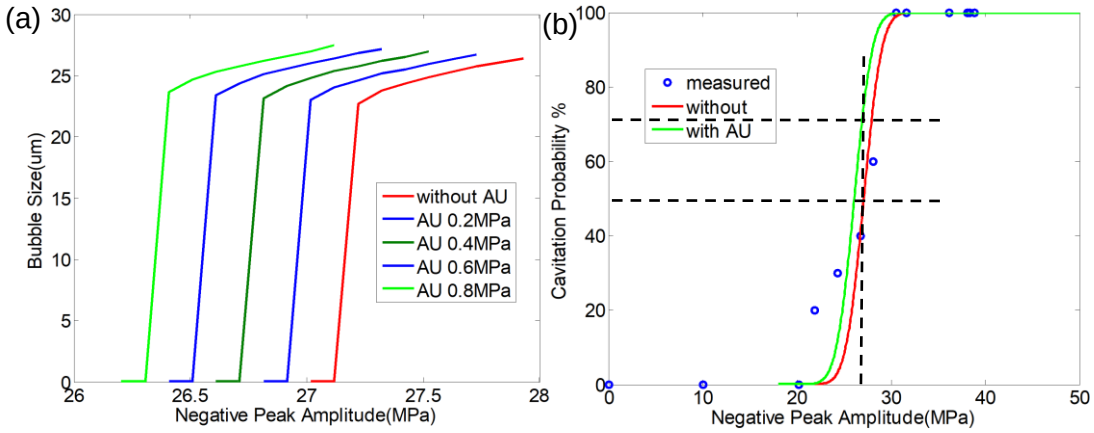


Figure 3-5: Cavitation threshold decrease with AU applied for different amplitude

50% cavitation probability point on the sigmoid curve. While the threshold is decreased from 27.15MPa to 26.1MPa due to AU~1MPa, the cavitation probability will be increased by 26%. Moreover, this enhancement on generation rate doesn't depend much on the AU frequency in the range of 2.6MHz to 3.5MHz(in experiment). This is because the negative part(while cavitation nuclei are excited) in LGFU duration is <50ns, and that of AU is much longer(>150ns), so the AU field can be treated as a constant pressure field during the LGFU, and it doesn't vary much as long as it's duration is longer than that of LGFU. Both

simulation and experiments agree with the enhancement is linearly related with the applied AU.

In experiment, however, we experienced a larger enhancement of 32% instead of 26% in simulation. This underestimate is likely due to the ideal model we used where no heterogeneous cavitation is considered. Besides, the collapse of bubbles also induces shock waves, which can excite nuclei efficiently in reality [17]. We conclude that for a qualitative

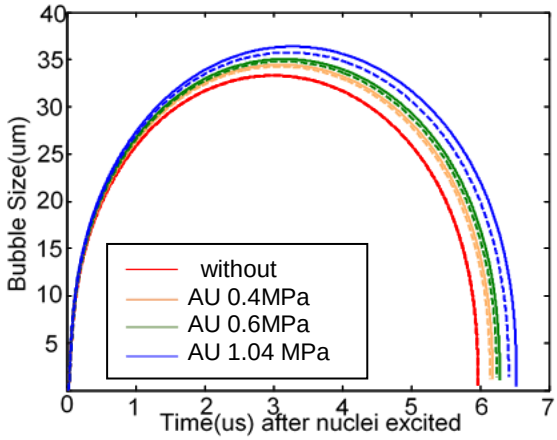


Figure 3-6: Bubble growth after nuclei excited under different AU amplitude, where solid line is 2.6MHz AU, dashed is 3.5MHz AU

study, this model is valid, but we will study more on the modeling of the cavitation probability in future work. Then we characterized the maximal size the bubble can reach with and without AU and found that the bubble sizes increased when AU(up to 1.04MPa, 2.6MHz(solid line) and 3.5MHz(dashed line) sinusoidal pulse) is applied, see Fig. 3-6. The bubble first expands to a maximal size, and collapse at final stage, this trend is similar as we saw in experiment. Both simulation and experiment showed the maximal bubble size increase with the AU amplitude. Moreover, the increase also doesn't vary much with the AU frequency, see Fig. 3-6. However, the measured data shows 60% increase in size for 1.04MPa AU while the simulated data shows much less increase, which is ~10%. We

believe that is due to the merging effect of bubbles that bubbles in the focal region merge into one larger bubble. The actual size increase should be a sum of all increase of each individual bubble.

## 3.5 Conclusion

In this work, we for the first time, applied CS/PDMS lens for the generation source of LGFU, and demonstrated with an assisting pressure field with of only ~-1MPa, we can achieve cavitation enhancement of ~30% in generation rate and ~60% in maximal size. We found the cavitation enhancement is proportional to the amplitude of the assisting field and is independent of the frequency. Compared to other cavitation enhancement, this AU enhancement doesn't require any injection, therefore, the non-invasive nature is preserved. Both the increase of the number and size of the cavitation imply larger mechanical ablation energy.

Additionally, we used the Rayleigh-Plesset equation to simulate the dynamics of this enhancement for this combined field for the first time. The future work will be focused more on the model to help predict better the bubble behavior, such as merging effect. However, it illustrates itself as a good model in explaining the physics under this enhancement. Moreover, we believe this enhancement method provide a new way to enhance the current LGFU for real phantom/tissue treatment. The generation rate implies a faster treatment speed and maximal size increase implies a larger mechanical ablation energy, both of which will help LGFU application.

# Chapter 4

# Characterizing Cellular Morphology by Photoacoustic Spectrum Analysis with an Ultra-broadband Optical Ultrasonic Detector [5]

## 4.1 Introduction

Photoacoustic Imaging (PAI) is a hybrid medical imaging modality based on light-induced thermo-acoustic effect in biological tissues. PAI combines the advantages of both optical and ultrasound imaging as it provides both optical resolution and enough penetration depth. Previous studies on PAI were mainly focused on measurements of photoacoustic (PA) signal amplitude, which reflects the overall optical absorption of the target tissue. Recent studies have shown that the power spectrum of the PA signal also contains the micro-structural information of the tissue[96-103]. Aiming at quantitative tissue imaging and characterization using spectral information, photoacoustic spectral analysis (PASA) was developed. PASA is based on the fact that the frequency components of the PA signals are closely correlated to the morphological properties of optically absorbing objects in tissues, including their sizes, shapes, and densities [104]. For example, smaller objects generate shorter PA signals in the time domain, which have broader power spectra containing more high frequency components than PA signals of larger objects. Quantitative analysis of the PA signals in the frequency domain would

enable an objective evaluation of the morphologies of optically absorbing objects stochastically distributed in biological tissue [105]. Previous study borrows the idea from ultrasound spectral analysis (USSA), using the *slope*, *mid-band fit*, and *interception* of the linear regression model to characterize the main features of the signal power spectrum [99]. However, linear regression fitting might sometimes experience larger error and we use $4^{th}$ order polynomials to fit the PSD of the PA spectrums for these cases. The coefficients of $1^{st}$ order were found to be able to relate the diameter and the spectrums. PASA offers solutions to a number of practical issues faced by PAI. Firstly, the averaged power spectrum provides a robust method of quick characterizing the stochastic nature of tissue microstructures and can lead to measurements that are more quantitative and repeatable. Also, PASA separates the contributions of system components from tissue properties on image features and obtains system-independent results.

Previous PASA system used conventional piezoelectric transducers for ultrasound detection, which usually had limited acoustic response bandwidth. For example, by using commercially available or home-fabricated piezoelectric transducers, PASA has been explored for applications in diagnosis of prostate cancer [105] and evaluation of liver conditions [102]. In these studies, PASA was performed on the tissue level, and the targeted biological tissues (e.g., small vessels, cellular groups, and lipid clusters) have features on the scale of over 100 microns. In order to achieve unambiguous evaluation of cells with sizes on the order of a few microns, the ultrasound detector must have a bandwidth of a few hundreds of MHz Photoacoustic microscopy systems with specially-designed high-frequency piezoelectric transducers have been used to study the morphology of single red

blood cells[103, 106, 107]. Detecting high-frequency ultrasound signals (e.g., ~hundreds of MHz), however, usually requires carefully manufactured transducers with thin and fragile piezoelectric elements. Besides, due to the resonance effect in the piezoelectric part, these transducers usually have maximum responses at a high frequency, and therefore, a reduced response at the low frequency regime[108-110].

In this chapter, we demonstrate an all-optical PASA system using a polystyrene (PS) micro-ring optical resonator as the ultrasonic detector[111, 112]. Micro-ring resonator has been demonstrated as a high-performance ultrasound sensor with both broad bandwidth and good detection sensitivity. Our previous studies have shown the detector has an intrinsic acoustic response from nearly DC up to 350MHz at -3dB [10], and a noise equivalent detectable pressure over this bandwidth as low as 105 Pa, which is comparable to that of conventional piezoelectric transducers. PA signals from biological samples contain information of both micro- and macro-size structures and are broadband in nature. Micro-ring ultrasonic detectors largely improve the performance of PASA for tissue characterizations by extending its scope from the tissue level to cellular level. With such a system, we have achieved size characterization of microspheres below 20 μm, and successfully differentiated fresh and aged blood cells due to the difference in their shapes.

## 4.2 Principles

### *4.2.1 Working principle of micro-ring*

A micro-ring resonator consists of a ring-shaped waveguide coupled with a straight bus waveguide and light will be coupled in and out of the ring through the gap region. The output intensity spectrum contains dips occurred at specific wavelengths when the corresponding round trip phase accumulation in the ring waveguide equals to multiples of $2\pi$ radians. This round-trip phase accumulation depends on parameters, such as the ring radius, cross-section size, intrinsic refractive index of the polymer waveguide core/cladding, all of which can affect the effective index of the propagating mode. While the ultrasound hit the waveguides, the intrinsic refractive index will be changed through elasto-optic effect. At the same time, the ring is deformed by the ultrasound waves. Both effects altogether shift the ring resonant dip, therefore the output intensity when input light wavelength is fixed at the sharpest slope of the transmission dip. The output intensity is measured by a high-speed photodetector (125MHz, Model 1801, Newport). Micro-ring has been applied in high-resolution photoacoustic imaging[113,114], as well as real-time THz pulse detection [115]. It has an ultra-broadband intrinsic acoustic response from nearly DC to 350 MHz at -3dB. However, the whole system acoustic response bandwidth is further limited by the bandwidth of 5ns laser pulse and photodetector's bandwidth. To evaluate the performance of the PASA system equipped with the micro-ring, the laser beam was illuminated on a thin Cr film (200-*nm* thick), which could be approximated as an impulse response, and the generated PA signals were detected by the micro-ring placed at 3 mm away from the film. The PSD of the PA signal from the Cr film is in Fig. 4-1(b), which shows the system bandwidth of 123 MHz (at -10dB).

### *4.2.2 Fabrication of micro-ring*

A silicon mold is fabricated by E-beam lithography for defining the ring pattern at first: E-beam first define the pattern on the PMMA mask on silicon substrate and then the PMMA get developed. It's worth to note that after the PMMA development, a thermal reflow process (115℃, 90s) is introduced to reduce the imperfections and hardens the PMMA feature edge. Afterwards, the PMMA mask is used in plasma coupled reactive ion etching (RIE) to transfer the pattern down onto silicon substrate. Then this silicon mold is applied in thermal imprinting process as the mold pressing onto polystyrene (PS) resist on SiO2/Si substrate. During imprinting, the temperature of the resist is increased above glass transient temperature by ~70℃ to ensure the low viscosity at first, then a uniform pressure is applied onto the mold and the resist flows into the trench to form the pattern. At last the temperature is cooled and the PS microring device is demolded from the silicon mold.

### *4.2.3 Working principle of PASA*

The working principle of PASA on size characterization is based on least squares polynomial fit on the power spectra of PA signals of optical absorbers. The power spectra represent the distribution of power into frequency components, which is calculated as the square of the Fast-Fourier transform of the time-domain PA signals. PA signals from spherical objects have been derived analytically and the power spectrum of those time-domain bipolar signals show periodic dip pattern at certain frequencies [116]. A general approach to differentiating two spheres in spectrum with different sizes is to compare the difference in the locations of the dips in spectrum. This method becomes ineffective when

sample concentration goes up and the details("dips") in the spectrum are smoothed out, leaving only a contour of the curve.

Aside from locating the dips, G. Xu *et al.* [117] found the spectrums of microspheres descend almost along a linear fit (1st order polynomial) after the first peak in the spectrum and larger objects decay faster because they contain less high frequency components. We also found the same trend of increasing coefficient of the 1st order term for 4th order polynomial curve, which can be used to describe the PSD curve with less error. We fit the data into $y= p_1x^4+ p_2x^3+ p_3x^2 +p_4x+p_5$ with least-squares fitting where $S = \sum_{i=1}^{n}(y_i - ( p1xi4 + p2xi3 + p3xi2 + p4xi + p5))\text{^}2$. All the fit lines are within 5% errors of the original data, and we found the coefficients of all the terms can be used as a parameter to differentiate spectrums of concentrated microspheres' samples, where we select the $p_4$ coefficient, which is sensitive to the size of PA generator more than other coefficients. It is worth to note that in principle, higher order polynomials can fit the PSD even better, but with 4th order polynomial, we already achieved an error smaller than 5% for the frequency range we are interested in. Additionally, the PSD of microspheres becomes more different at higher frequency because all sizes contain similar amount of low frequency component therefore the difference is larger at higher frequency.

*4.3 Experiment setup and sample preparation*

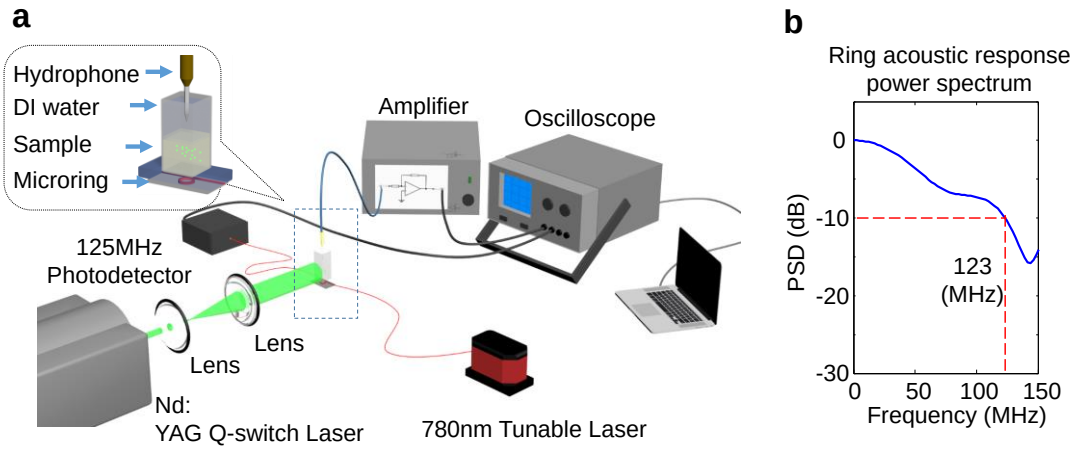


Figure 4-1: (a) Schematic of the PASA system equipped with a micro-ring detector beneath the sample. A calibrated needle hydrophone was hung above the sample at same distance for comparison. (b) The power spectral density (PSD) of the PA signal versus frequency produced by illuminating 5-ns laser pulses on a 200-nm thick Cr film received by micro-ring, which we used as the acoustic intensity response for this whole ring-based PASA system. It demonstrated a -10 dB bandwidth of 123 MHz.

The setup for our PASA system for tissue characterization is shown in Fig. 4-1(a). Laser pulses from an optical parametric oscillator (OPO) pumped by a Nd:YAG laser(Vibrant B, Opotek) were used to illuminate the sample and to generate photoacoustic signals. The pulses had a wavelength of 532 *nm*, pulse duration of 5 *ns*, and repetition rate of 10Hz. The laser beam was expanded and illuminated the sample. The sample was a cube of 10% (volume ratio) porcine gel held in a plastic container and contained stochastically distributed polystyrene-based latex microspheres or red blood cells (RBCs). The container had openings at both top and bottom and the PA signals propagated through acoustic coupling gel downward to the ring and upwards through the DI water to the hydrophone for comparison. The micro-ring was placed underneath the sample, and was covered by a thin light-blocking film (silver Mylar balloon) to be protected from damage by the scattered laser light. DI water was injected between the micro-ring and the film for better coupling

of acoustic signal. To compare the performance of the micro-ring to conventional piezoelectric transducers, a calibrated needle hydrophone (HNC-1500, Onda) with a detection band from 0 to 37 MHz (-10dB) was placed on the top of the sample for measurement of PA signals. The distances from the center of the laser beam to the two ultrasonic detectors (i.e., the micro-ring and the hydrophone) were kept the same (3 *mm*). The PA signals received by the micro-ring and the hydrophone were recorded at the same time by a digital oscilloscope (TDS 540B, Tektronics, sampling frequency 500MHz) and averaged 300 times to increase the signal to noise ratio (SNR).

To prepare the phantoms with stochastically distributed microspheres or blood cells, we mixed the samples in a porcine gel. The densities were controlled so that the particles were distributed randomly without aggregation (for blood samples, we used phosphate buffered saline (PBS) to dilute the samples at first). The properly controlled density also allowed light beam to pass through the entire phantom without much attenuation, and therefore, the illumination intensity is uniform over the whole phantom. The microspheres or the blood cells were added while the gel was in liquid form, and the gel was stirred using a magnetic stir bar to achieve stochastic distribution. After the gel cooled down and became concrete, a phantom containing randomly distributed samples was prepared.

## 4.4 Results and discussion

### *4.4.1 PASA of individual microspheres*

The performance of the PASA system was first evaluated by measuring signals from individual microspheres (Fluoresbrite plain YG micro-spheres, Polysciences) of different

sizes (*i.e.*, 20 $\mu m$, 45 $\mu m$, and 100 $\mu m$ in diameter, respectively). In the case of individual microspheres, we can evaluate the size by locating the first dip location in the spectrum of the PA signal which preserves the details of the whole spectrum. The analytical expression for the spectrum of the initial PA signal generated by microspheres is given by $S(\omega) = A^2 \cdot \{1 + \sin[2\omega \cdot (R_s/v_s) + \gamma]\} \cdot [\frac{2}{\omega^2} + \frac{2}{\omega^4 (R_s/v_s)^2}]$, where $\gamma = \tan^{-1}\{[\omega(R_s/v_s) - 1/\omega \cdot (R_s/v_s)]/(-2)\} - \pi$ and therefore, the first dips occurs when $varying\ phase\ term = 2\omega \cdot (R_s/v_s) + \gamma = \frac{3}{2}\pi + 2k\pi$, where k=0,1,2… [117] The measured PA signals from the individual microspheres with different sizes are shown in Fig. 4-2(a-c) respectively, which have characteristic bipolar shapes for each signal. Larger spheres generate longer bipolar signals and in turn, narrower spectrum "lobes", so the first dips happen at smaller frequencies. The normalized PSD versus frequency curves for microspheres with three different sizes are shown in Fig. 4-2(e-f) with solid line. In this study, facilitated by the ultra-broad detection band of the micro-ring, the PSD from 20 μm, 45 μm and 100 μm microspheres were all matched well with simulation results (using a k-wave toolbox in Matlab), as shown in Fig. 4-2(e-f) with dashed line. Experimental results (Fig. 4-2(d-e)) showed the first "dip" in the PSD profiles at 113MHz, 48MHz, and 26MHz for 20-$\mu m$, 45-$\mu m$, and 100-$\mu m$ microspheres, respectively, which matches well with the simulated PA signal spectrums as well as the numerical solutions for the first dips, shown in Fig. 4-2(g).

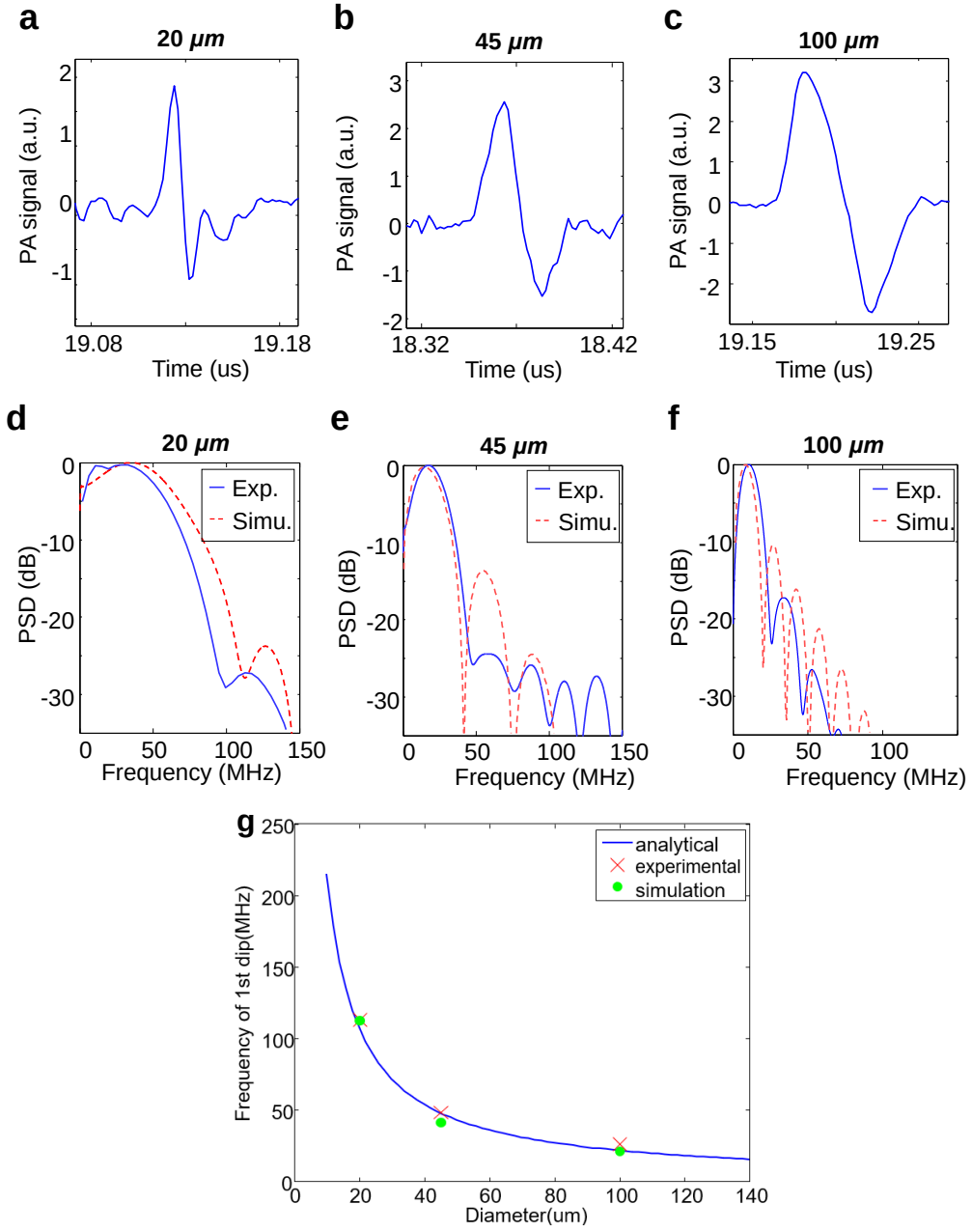


Figure 4-2: PA signal power spectrum of individual microspheres. (a) (b) (c)Time domain PA signal from the microspheres with different sizes (i.e. 20 μm, 45 μm and 100 μm). (d) (e) (f) Normalized PSD curves from each individual microsphere measured by the PASA system equipped with the micro-ring (solid line). Simulated PSD curves from the individual microspheres with sizes same as the ones in the experiment (dashed line). (g)Frequency of first dip for microspheres with different diameter with analytical, experimental and simulated data.

*4.4.2 PASA of stochastically concentrated microspheres*

Different than single microspheres, it's difficult to locate a specific dip in the spectrum to characterize the size information because in the PSD, the dip that refers to zero PA intensity can be smoothed out by a slightly larger or smaller sample. These concentrated samples were prepared using the methods provided in section 2.3. The densities of microsphere particles in the gel were 1.7×106, 2.1×105, 4.6×104, 1.9×104, and 1.7×103 particles/mL, for particles with sizes of 3 μm, 6 μm, 10 μm, 20 μm, and 45 μm (with diameter variation coefficients of 5%, 5%, 5%, 4% and 6%), respectively. For each particle size, 4 phantoms were measured to calculate the averaged response and the standard deviation.

PA signals from each phantom were recorded by the micro-ring and the needle hydrophone simultaneously. As discussed in section 2.3, all the dip features of the power spectrum curves of individual spheres are smoothed out and $4^{th}$ order polynomial fitting was conducted within systems' 0 to -10dB response range to fit the spectrum curve with error <5%. Additionally, The PSD below 2MHz was excluded in the linear regression to remove the interference noise from the low frequency. Therefore, the frequency range of the fitting by the micro-ring based PASA system was from 2 to 123MHz, and that of the hydrophone-PASA system was from 2 to 37 MHz. The spectral parameter *slope* of the linear regression fitting line described the overall descending trend of the signal power spectrum, and directly related to the sizes of the studied microstructures.

The normalized and averaged PSD curves of the PA signals from phantoms with different-size microspheres are plotted in Fig. 4-3, where (a) and (c) are the measurements from the micro-ring and the hydrophone, respectively. The $p_4$ coefficient of the first order term in the fitting polynomial is exponentially increasing with respect to diameter of microsphere,

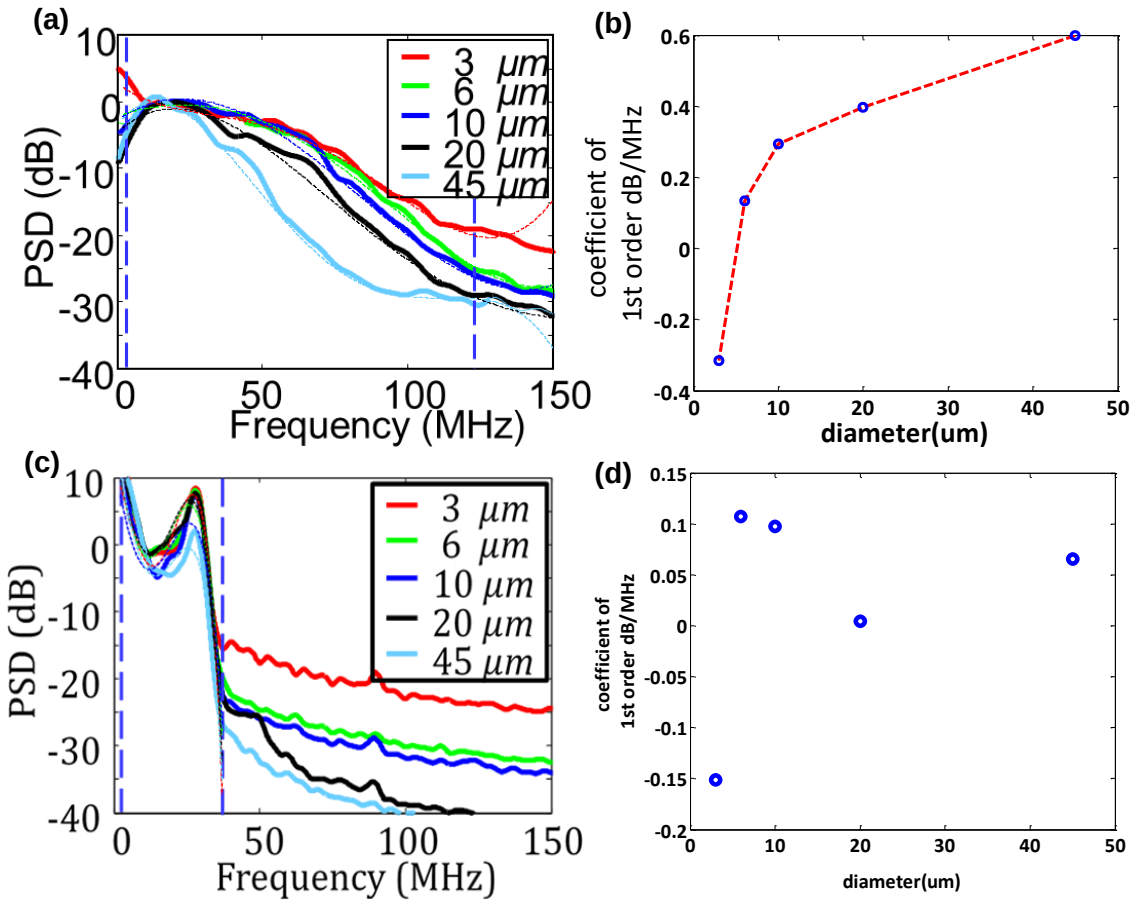


Figure 4-3: PASA of phantoms containing different sizes of microspheres (including 3 μm, 6 μm, 10 μm, 20 μm, and 45μm). Each size contains 4 phantoms. (a) Normalized and averaged PSD curve for each group as measured by the micro-ring. The fitted line was made as an example for each PSD in the range of 2-123MHz. (b) p4(coefficient of first order term) of the polynomial fitting curve of the data measured PA signal detected by the micro-ring. (c) The normalized and averaged PSD curve for each group as measured by the hydrophone. (d) p4(coefficient of first order term) of the polynomial fitting curve of the data measured PA signal detected by the hydrophone.

which is used to characterize different object sizes from 3 to 45μm from measured data of microring. In contrast, the measurements from the hydrophone with narrower detection bandwidth, are not able to find a consistent relation of the coefficient of any terms in the

fitting polynomial with the microsphere size. The qualified spectral parameter *p4 coefficient* for the results from the micro-ring and the hydrophone are compared in Fig. 4-3(b) and (d). It should be noted that using coefficient of other terms, there will still be a consistent relation of the coefficient with diameter with the measured data from microring, but failed to find a consistent trend with data of hydrophone due to the limited bandwidth, This is due to the reason that the PSD of all the sizes contain low frequency components, however, the larger samples contains less high frequency components, where the fitting polynomial curve start to become more different. It can be seen that PASA using the hydrophone can hardly distinguish the phantoms containing microspheres smaller than 20 $\mu m$. In contrast, PASA using micro-ring shows an excellent capability in differentiating the phantoms with microsphere sizes ranging from 3 to 45 $\mu m$. This study of phantoms with well-controlled particle size indicates that micro-ring's ultra-broadband response facilitates reliable PA characterization of micron-size objects which are stochastically distributed in samples.

### *4.4.3 PASA of ex vivo human blood specimens*

To explore the ability of PASA with micro-ring in characterizing cellular level microfeatures of biological samples, an experiment on *ex vivo* human blood specimens was conducted. Human blood contains red blood cells (RBCs), which have a biconcave, disc-shape. They are approximately 7-8 microns in diameter, 1-2 microns in height, and 80-100 femtoliters (fl) in volume [118]. Certain diseases, infections, or exposure to toxic chemicals can alter the morphological features of RBCs, impairing their functionalities. Since various morphological abnormalities of RBCs are closely correlated with specific disease states,

studies have been focused on developing techniques that can characterize the morphological changes in RBCs *in vivo* or *ex vivo*[119,120].

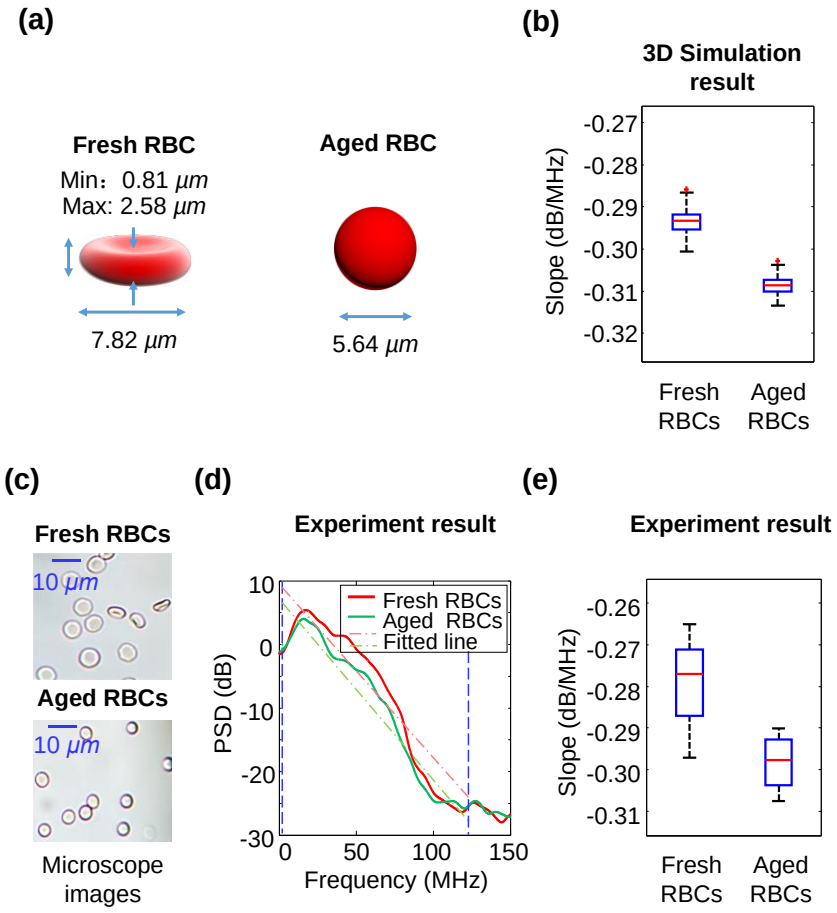


Figure 4-4: PASA of ex vivo human blood specimens. (a) The geometries and dimensions of biconcave (fresh) and spheroid (aged) RBCs used for simulation. (b) PA spectral parameter slopes for the two groups of blood samples (i.e. fresh blood and aged blood), as quantified in the simulation (N=100). The fitted line was made as an example for each PSD in the range of 2-123 MHz. (c) Microscopy images of the fresh and the aged blood specimens used in the experiment, showing the morphological changes in RBCs as a result of storage. (d) PSD curves from fresh RBCs and aged RBCs samples, as measured in the experiment. (e) Spectral parameter slope qualified for the two groups of samples (fresh vs. aged) measured in the experiment (N=4). The two groups can be differentiated with a p value $< 0.05$.

We explored the feasibility of PASA in evaluating the morphological change of RBCs as a function of the blood storage time. Previous studies have shown that the geometry of RBCs becomes more spherical with storage, and therefore have a smaller surface area to

volume ratio [121]. This morphology change can be reflected in the power spectrum of the PA signals. It's worth to note that for the blood sample spectrum, we fitted them with linear line instead of $4^{th}$ order polynomials, simply because the fitting error is small enough. We use the *slope* of the fitting line to evaluate the sample size. Before the experiment, we performed simulation using same toolbox in section *3.2*. Two groups of samples each containing different shapes of RBCs (biconcave, and spheroid) reflecting different levels of freshness (fresh and aged) were studied. The detailed geometries of biconcave and spheroid RBCs are shown in Fig. 4-4(a). The biconcave shape used to describe normal RBCs has a diameter of 7.82 $\mu m$, a minimum height of 0.81 $\mu m$, a maximum height of 2.58 $\mu m$, and a volume of 94 $\mu m^3$ [122]. When RBCs are aged, their shapes are changed first to oblate and then spheroid, as described in Fig. 4-4(a), while their volumes are kept the same [123]. In simulation, each sample contained stochastically distributed RBCs with a concentration of $1.7\times10^6$ *cells/mL*. The orientations of the RBCs in each sample followed a gauss distribution. The density, the speed of sound, and the ultrasound attenuation of the sample were set as 1000 $kg/m^3$, 1540 *m/s*, 0.2 $dB/(MHz\cdot cm)$, respectively, in simulation. The effects of the ring response and pulse duration of the laser were also taken into account. For each group (*i.e.*, biconcave and spheroid), 100 samples (N=100) were studied for statistical analysis of the findings. The PA spectral parameter *slopes* for the two groups, as quantified in the simulation, are compared in Fig. 4-4(b). It's worth to note that for the fresh RBCs, most of them were lying flat as disks when they were stable, therefore the PA signal contains very large high frequency components due to the small vertical thickness (smallest feature in the sample). For the aged RBCs, even though the diameter appears smaller, the vertical thickness, which is the smallest feature, is actually larger than that of

fresh ones since it's spherical. This difference in shapes gives us the chance to differentiate them and explains why the visually smaller aged RBCs has smaller high frequency part and smaller *slope*. This is basically how shape differentiation is realized for such geometries.

As an experimental demonstration, two groups of samples were prepared, one using fresh human blood specimens (< 2 weeks in storage) and the other using aged human blood specimens (3 months in storage). The RBCs in the fresh and the aged blood specimens were photographed under a microscope (FMA050, Amscope), as the example pictures shown in Fig. 4-4(c). The blood samples were diluted 1:100 in PBS at first, and then mixed 1:30 with 10% porcine gel. Then we followed the other procedures in section 2.3 for phantom preparations. The concentration of RBC ($1.2\text{-}1.8\times10^6$ *cells/mL*) in each sample is consistent with the concentration we used for simulation. The number of samples in each group (i.e. fresh and aged) was 4. Fig. 4-4(d) shows an example PSD curve from each group. As expected, aged RBC sample has slightly high frequency component in the PSD. By performing the linear regression fit of the power spectrum in the range of 2-123MHz, the quantified spectral parameter *slope*s from the two groups were obtained, as compared in Fig. 4-4(e), where aged RBC sample showed reduced *slope*. The experimental results matched well with the simulation.

## 4.5 Conclusions

The study described in this chapter demonstrates that PASA system equipped with micro-ring ultrasonic detectors, which have an ultra-broad and flat detection band, has the ability of characterizing morphological features including both size and shape in biological samples in the micron-size level analyzing PSD. And the system has demonstrated the ability to differentiate microsphere's down to ~3μm and differentiate the morphology difference in aged and fresh blood cells.

Table 4-1 compares this PASA system equipped with microring with several other spectrum analysis systems based on photoacoustic signals and our systems demonstrates a relative high resolution and the ability for concentrated micron-size tissue characterization.

Table 4-1: Comparison with other PASA systems

| | PASA | PASA | PASA |
|---|---|---|---|
| Analysis parameter | Coefficient of $4^{th}$ order polynomial fitting or *slope* when use linear fitting | Coefficient of $4^{th}$ order polynomial fitting | dips location |
| Ultrasound detector | microring | hydrophone | piezoelectric transducer |
| Bandwidth(-6dB)/MHz | 0-123 | 0-20 | 296-453 |
| Characterization size | ~3μm | 100μm | 2.8μm |
| Ability for analyze ~DC signals for macro structure | Y | Y | N |

Additionally, compared to extremely high-frequency piezoelectric transducers that usually involve elaborated fabrication ,and hence expensive, PS micro-ring is fabricated with much lower cost and better repeatability using nano-imprinting technology[112, 124]. The micro-

ring based PASA system holds potential to detect morphological abnormalities of cells and relate them with corresponding pathological conditions. Unlike existing technologies such as flow cytometry and peripheral blood smear examination, which are based on the complete imaging and analysis of individual cells, PASA is essentially a statistical method and, hence, may better deal with the stochastic nature of biological samples much faster. Moreover, PASA technique could be further developed into a fast-speed cell morphology analysis system for clinical use and could provide quantitative diagnostic information that is not accessible by the current qualitative imaging methods. One potential application, as explored initially in this study, is the *in vivo* diagnosis of RBC-related diseases or *ex vivo* characterization of donated blood. Besides RBCs, other cells providing strong intrinsic optical absorption contrast, such as melanoma cells, could also be evaluated with PASA working at proper optical wavelengths.

# Chapter 5

# Micron-size Soft Tissue Ablation with LGFU

## 5.1 Introduction

Laser-generated-focused-ultrasound (LGFU) has been demonstrated as a non-invasive mechanical ablation technique for water-rich materials such as organoids and gelatin gels phantoms [55]. The relative controlled manner of the cavitation generated within the focal region have been applied to as a noninvasive "scalpel" to cut or ablate the tissue mimicking phantoms. Compared to other cavitation-based ablation techniques, LGFU has advantages such as less thermal damage and higher accuracy. Laser microsurgery also generates highly focused cavitation area for tissue ablation, however, it is limited to tissue surface because of the light diffusion limit in biological tissues [125]. Compared with other therapeutic ultrasound ablation techniques such as histotripsy and high-intensity-focused-ultrasound (HIFU), LGFU can achieve a much higher resolution that is below 200μm taking the advantage of high frequency components in generated photoacoustic wave: HIFU taking advantage of thermal energy deposition by ultrasound or uncontrolled cavitation cannot reach resolution below 1mm; Histology equipped with conventional piezoelectric transducers cannot focus easily below mm range while keeping enough ultrasound intensity. [126] Additionally, LGFU is compatible with PAI systems, which ensures an optical resolution imaging guidance and a system of imaging and therapy towards selective

treatment. Furthermore, equipped with the newly-developed CS/PDMS PA lens, we can reduce the device cost for the treatment system. The focus of the LGFU can reach target down to ~1cm below the skin surface, which extends the potential application from ophthalmology, dermatology and some early-stage skin cancers. We propose the techniques to be applied to dermatology issues such as acne[127-131], spider veins [132] and surface malignant tissues on eyes such as ocular surface squamous neoplasia(OSSN) [133].

Though we have demonstrated the ablation power on phantoms mimicking biological tissues, the real biological tissues still differ from the gelatin phantoms in both water contents and mechanical strength. In this chapter, we conducted a feasibility study using LFGU equipped with CS/PDMS lens to ablate soft tissues in skin including glands wall structure (vesicles consist of lipid membrane), collagen and fat by treating sectioned human skin tissues *in vitro*, and mouse ear tissues and pig fat tissues *ex vivo*. These tissues are representative of either protein-based or fat-based biological tissues, and are not necessary water-rich. For the first time, we achieved <200μm ablation for such structures. This paves the way for further treatment purpose towards dermatology issues where skin structures consist of most collagen, glands and fat. Additionally, we demonstrated a 2D high resolution photoacoustic microscopy (PAM) system which is proposed to be applied in imaging guidance module.

## 5.2 Experiment setup and sample preparation

*5.2.1 System setup*

As stated above, our final goal is to build a therapy system that is able to achieve both imaging guidance as well as treatment. For this initial study, we constructed and demonstrated the imaging and treatment modules separately. The imaging system consists of an excitation 532nm DPSS pulsed laser, Galvo mirror, the microring ultrasound detecting system consists of microring, a 780nm tunable laser and high-speed photodetector and the data acquisition part consists of an oscilloscope, DAQ card and all components in the system is synchronized and controlled by a computer, the system schematic is shown in Fig. 5-1(a). The excitation laser of 5ns was first expanded, reflected by a Glavo mirror then focused to a <5μm spot onto the sample top surface. The sample is scanned by the Galvo mirror and the PA signal was detected by the broad band microring system described in Chapter 3. The signal is then processed by the DAQ card and image is reconstructed in 2D. This imaging system can image chromophores that are interested in dermatology. For example, by selecting the excitation laser with wavelength of 532nm, it can image the red vessels around acne, which comes from the increase in blood circulation caused by acne inflammation. Green light is also greatly absorbed for the black pigment, therefore, it can image the hair shaft in any follicle points. The combination of the two can be then used for the recognition of pimples in acne application. The treatment module is shown in Fig. 5-1(b), consists of a 532nm, 6ns pulsed Nd:YAG laser, the laser was first expanded to the diameter of the PA lens and reflected onto the back of the PA lens to generate focused PA wave. The sample was scanned by a 3D scanning stage with step size of 50 μm. By computer designed scanning pattern input to the stage, we realized ablation onto the samples in various pattern.

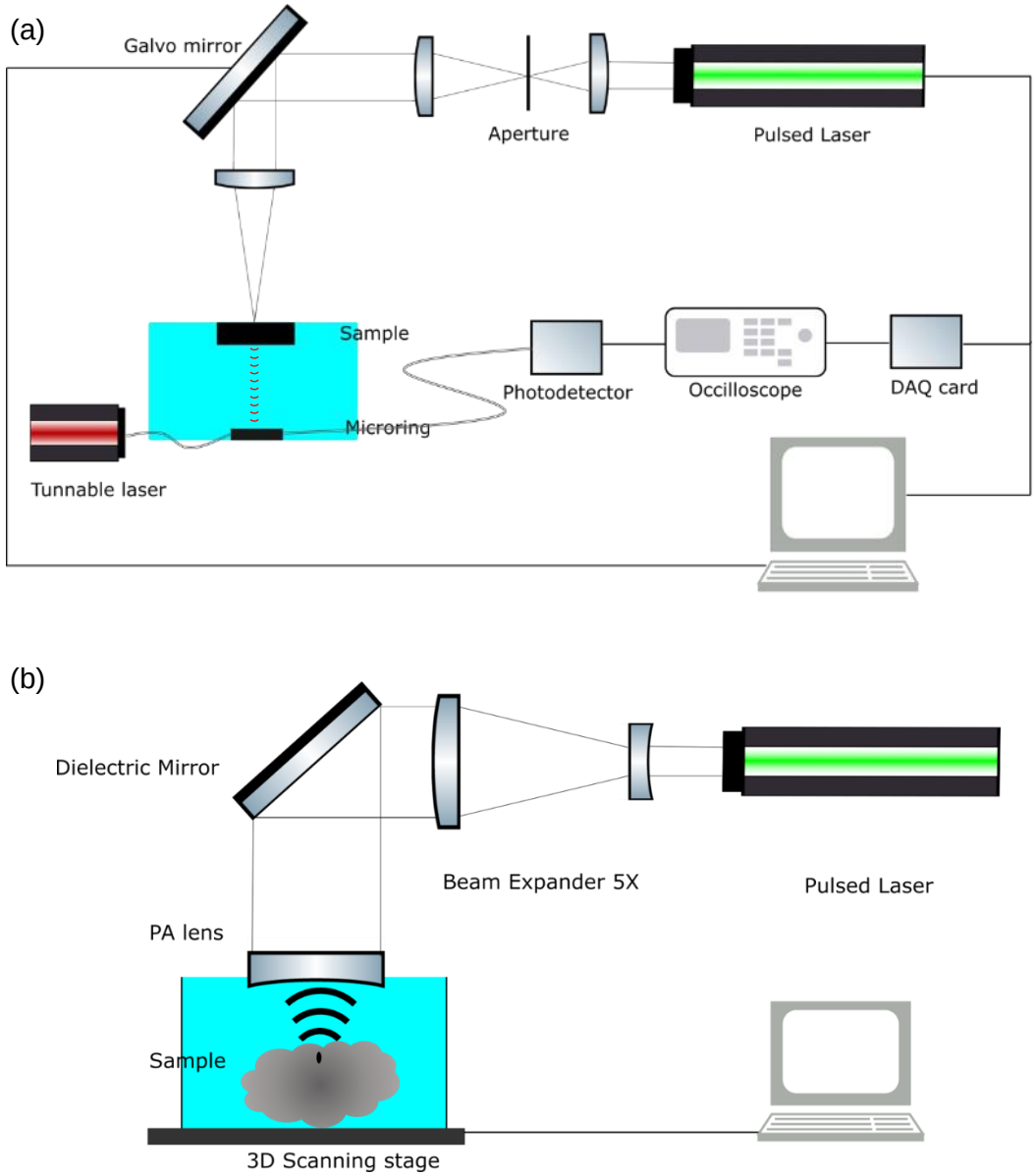


Figure 5-1: Schematic of setup of (a) imaging guidance module of 2D PAM imaging system, (b) treatment module of PA lens and scanning stage

### *5.2.2 Sample preparation*

The samples in the study for treatment are collagen, fat and sebaceous glands, which represents the most interested dermatology soft tissues. We used the human skin cut tissues

for collagen treatment, pork fat for the fat treatment and mouse whole ears with follicles for glands treatment. To prepare the sectioned human tissues, the human tissues were cut from facial skin from Mohr operation, see Fig. 5-2. Each tissue is of a thickness of ~5mm and triangular-shaped with the side of ~1cm. To get sectioned skin tissues, the fresh-cut tissues were first frozen in liquid N2 for 2mins and got sliced by the microtome into thickness of 25μm, 100μm and 150μm. The tissues were fixed on cover glass. Before the treatment, the samples were kept in the -4℃ to prevent any degradation. The samples were imaged before and after the treatment by optical microscope for comparison.

Figure 5-2: Human facial skin sample cut from Mohs surgery of skin cancer patients

For the pork fat tissue preparation, we bought the pork with skin and fat from the market and froze until the treatment. Before treatment, the pork fat was cut into a cube sample and then unfrozen to the room temperature and then ultrasonic coupling gel was applied on the surface of the pork fat tissue. After the treatment, the sample was taken right away for imaging to minimize the deformation of the soft tissue.

Mouse ears samples were cut from killed mouse right after mouse death and chemical depilatory (Nair hair remover, Nair) was applied to the surface ears for 10 minutes. This ensured complete removal of the hairs and provide better acoustic coupling. Afterwards, the ear samples were put into Hanks solution and stored at -4℃ refrigerator before treatment. During the treatment, the ears were laid on a gelatin hydrogel at the back side

and ultrasonic coupling gel (Lithoclear scanning gel, NextMedical) was applied on the top of the ears, both for reducing the reflection of the energy. The whole sample was then taped to the glass shown. Before and after the treatment, the samples were imaged by optical microscope for comparison.

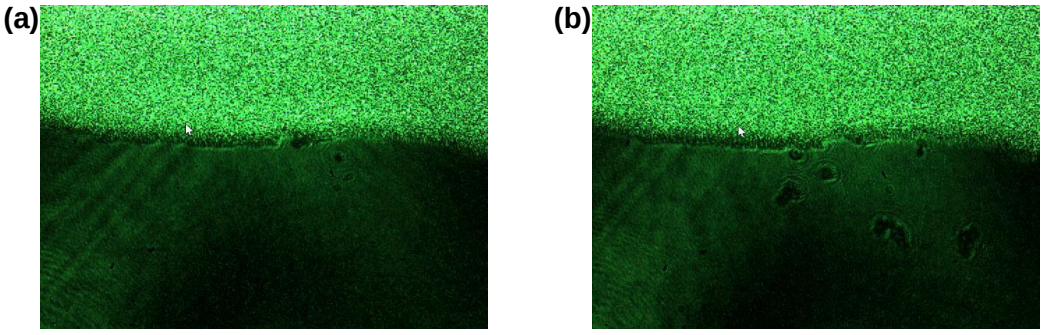


Figure 5-3: Shadowgraph images showing debris of some soft tissues were ablated by the LGFU focus

## 5.3 Results and discussion

### *5.3.1 Overview*

Firstly, we demonstrated the ablation effect on sectioned human skin *in vitro* for collagen ablation. The tissue is exposed to the focused ultrasound directly to the collagen region. Then we treated the pork fat tissues *ex vivo*, which contain the skin structures and components very close to human beings, to demonstrate the ablation effect on fat and fat cells. Finally, we treated the mouse whole ear with thin epidermis layers *ex vivo*, these ear tissues contain much more concentrated hair follicles and sebaceous glands than human skin, therefore, serving as a potential object for acne treatment study. The alignment of

focus was assisted by the laser shadowgraph system in the elevation direction. Fig. 5-3 shows when the cavitation happens at the skin tissue surface, some soft-tissue debris are ablated away from a defect or wound area of the skin. The laser shadowgraph system provided a guidance of the treatment in the initial stage and we are able to track the location of focused ultrasound in elevation direction

Each treatment was controlled within one hour and sent for imaging within 24 hours, which is considered good enough to prevent any degradation of the samples. And the samples are kept in Hank's salt (HBSS) buffer solution in refrigerator all the time other than during the treatment. Afterwards, the samples will be sent for imaging. Expected treatment effect will be deployment or rupture of the cells within the treating area.

At last, we demonstrate the 2D PAM imaging system for guidance purpose for LGFU for future application. We reconstructed images of phantoms of printed black mesh grid with linewidth of ~100μm and Cr on glass substrates with linewidth of 4μm. The quality and resolution of the system is considered well enough for the imaging of structures in micron size with black or red absorption.

### *5.3.2 in vivo collagen sample ablation*

We explored the ablation effect on the collagen using sectioned skin tissues with thickness of 25μm, 100μm and 150μm, and examined the treatment area under optical microscope in bright field before and after treatment for comparison. The below figures show ablation effect on the samples with different thickness. The ultrasound focus is located below the

slice at first and then scanned upwards with different doses for different thickness samples. A negative ultrasound pressure of ~60MPa is applied to guarantee cavitation clouds formation at the focal point. We define the treatment dose here as number of pulses/step and the samples is scanned over pre-defined patterns with step size of 50μm controlled by a 3D scanning stage.

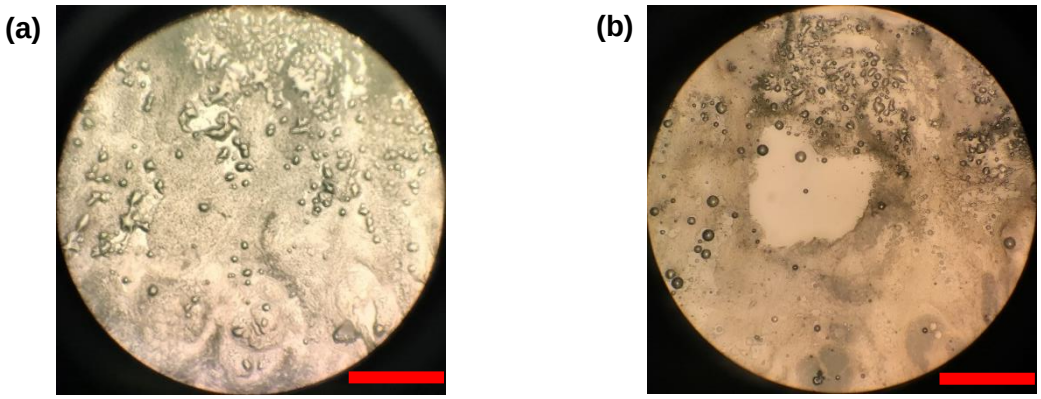


Figure 5-4: 25μm sectioned human skin sample, was treated of square area of 0.8mm*0.8mm with 30 pulses/step, before treatment(L), after treatment(R), imaged under reflecting light microscope, scale bar 1mm

For the 25μm sample in Fig. 5-4, a square area of collagen area was fully depleted with 30 pulses/step; for the 100μm sample in Fig. 5-5, a pre-designed L-shaped region of collagen was fully ablated with 45 pulses/step. We are able to see the 90°corner of the pre-designed L-shape in the cut region, and also the cut region has matched shape of the designed pattern, which has the width of 200μm. This demonstrate the potential ablation resolution <200μm; For 150μm samples, it requires at least 55 pulses/step to fully ablate the area. It's worth to note that for 150μm sample in Fig. 5-6, four pre-defined square patterns were treated with different doses. We found that the ablation effect is directly related with the dose and can be controlled by adjusting the pulse numbers on one scanning step. For the #1 square, 55

pulses/step doses are applied, and the section was fully ablated, for #2(45 pulses/step) and #3(35 pulses/step), the bottom layer of the collagen tissue was still partially connected. #3 showed a better ablation, but it could be due to the fact that the sample was not held perfect flat so that some region is treated more in vertical direction. For #4 square, only the upper layer was destructed. This series of experiments show the LGFU ablation effect on the soft tissues including glands and collagen in the skin structure, and the ability of the system to control destruction degree by varying the dose.

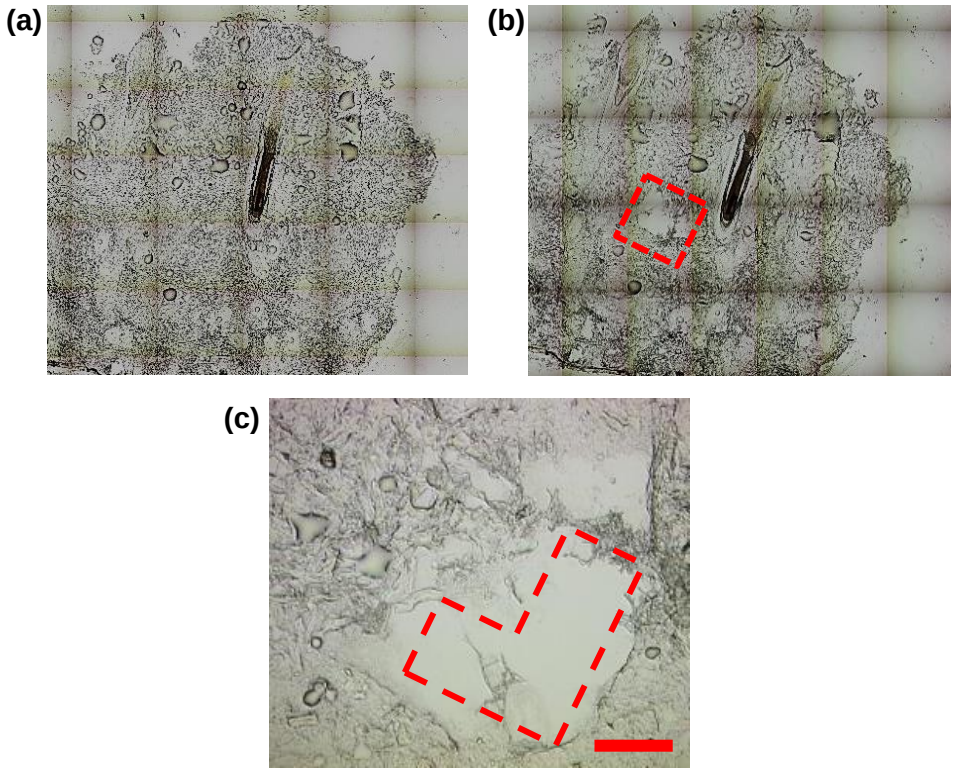


Figure 5-5: 100μm sectioned human skin tissues, was treated of an L-shaped region with 45pulses/step. Images taken with transmitted light microscope: (a) Before treatment, magnification 5X (b)After treatment, magnification 5X (c) After treatment, treated area, magnification 10X, scale bar 200μm

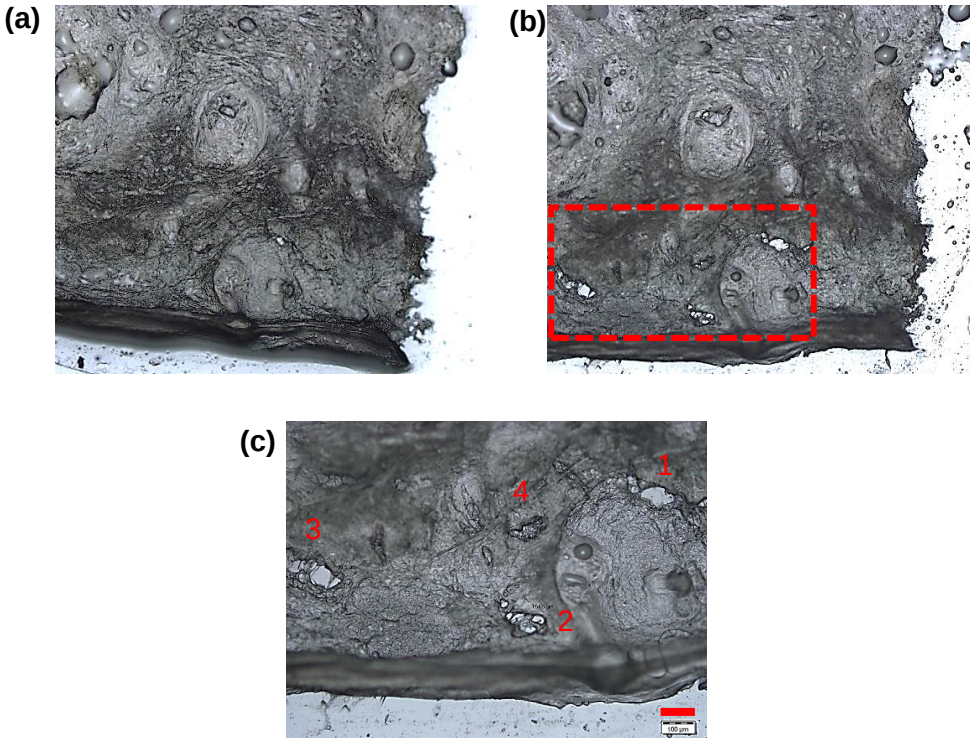


Figure 5-6: 150 μm sectioned human skin tissues, four squares of 200 μm were treated with a decreasing dose, square 1 with 55 pulses/step, square 2 with 45 pulses/step, square 3 with 35 pulses/step, square 4 with 25 pulses/ step. Images were taken with Olympus BX-51 microscope, bright field: (a) Before treatment, magnification 5X (b) After treatment, magnification 5X (c) Treated area, magnification 10X, scale bar 100 μm

The averaged dose for ablation of a collagen layer is 1.93μm/pulse based on the data we observed, at a peak negative pressure of ~60MPa. And this series of experiments demonstrates not only the ablation on strong protein-based tissues, but also proved the possibility of a controlled ablation speed by simply control the treatment dose(pulse/point).

*5.3.3 Fat ablation with pork fat ex vivo*

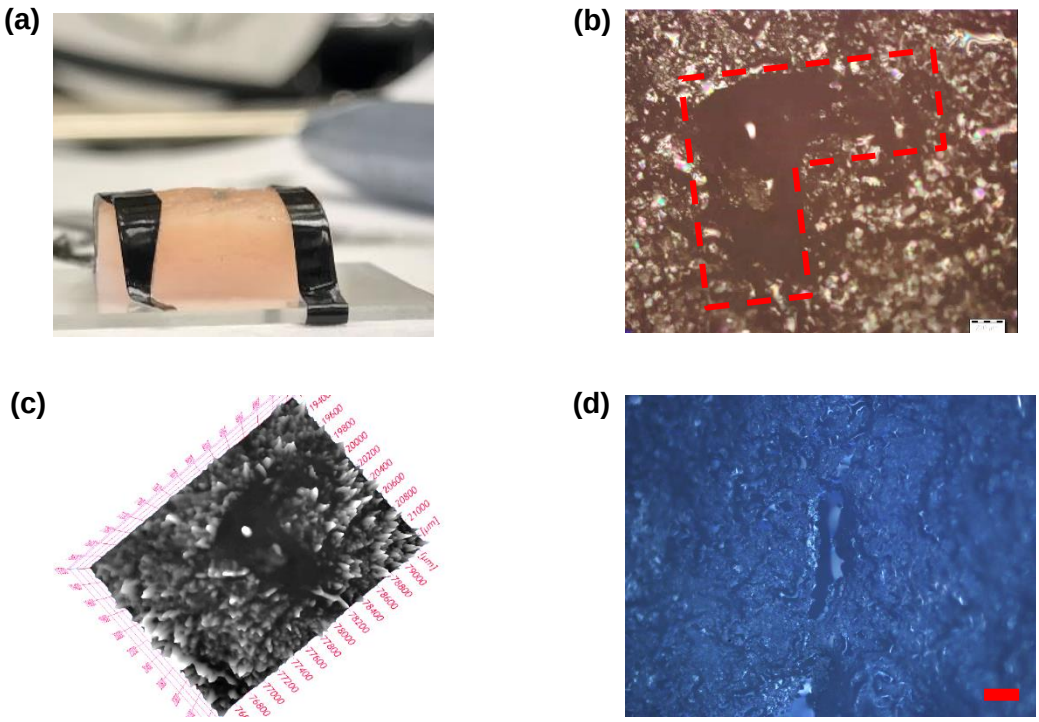


Figure 5-7: (a) Photo of the pork fat tissue. (b) An L-shaped area is ablated from the fat tissue surface under microscope X5. (c) 3D image showing the ablated area on the surface

We treated fat tissue *ex vivo* using port belly because of the similarity of the components in the pork skin and human skin structure [134] . And this demonstrate a direct ablation effect on the fat. 100 pulses/step pulses are applied to the fat tissue and after the treatment, the pork tissue is examined by the microscope in either bright field, dark field or 3D imaging, whichever provides the most contrast for the ablation. From Fig. 5-8(a), (b), and (c), we can tell a L-shaped region is directly ablated from the pork fat surface, demonstrating the effective ablation on fat cells. We then decreased the treatment dose to explore the best ablation resolution the system can reach on fat. Above a dose of 40 pulses/step, we are able to define a 100μm line on the surface of pork fat. From the picture, it's shown as a uniform dark region in the microscopy reflection mode. This

suggests a minimal resolution ~100μm, which is close to our focus spot size. Below this threshold, the damage is difficult to get visualized under microscope because the fat tissue surface is relative rough with too much scattering light. It is also worth to note that the ablation area isn't as clear as the cut in Fig. 2-5, because the fat cells were expected to be ablated away in clusters, therefore, the ablated surface is not perfect flat.

### *5.3.4 Glands vesicle structure with mouse whole ear ex vivo*

At last, we did LGFU treatment on mouse whole ear samples *ex vivo* to test the LGFU effect inside tissues onto glands, including both vesicle structure and cells. The mouse ear is selected because of it's concentrated of hair follicles and therefore sebaceous glands. The sample was treated with 90 pulses/step for an L-shaped region. Fig. 5-8 shows that after the treatment, the original glands area near the treatment area, marked by the red ellipse in the picture, appeared lightened color, suggesting potential destruction of the gland's vesicle structure, for example, the lipid outside layer was destructed.

Then, we applied oil red o staining after LGFU treatment to demonstrate that the treatment can destruct the oil components and oil cells within the glands, which is manifested by the unsuccessful staining with Oil-Red-O on fat component. Oil-Red-O is diazo dye used for lipids staining. The treatment area was a rectangular region of 450μm by 300 μm, after the treatment, the whole ears was fixed in 5% neutral-buffered formalin for 5 minutes, washed in DI water, and stained with oil-red-o working solution (0.5% in propylene glycol, Sigma-Aldrich), then washed and stored with HBSS solution before microscope imaging. The resultant microscope image showed a rectangular region was not stained red as well the surrounding region: instead of defined glands in sharp red color, the region is in light red

color. This suggests the potential liquify effect on the glands membrane structure so that the staining failed and spread.

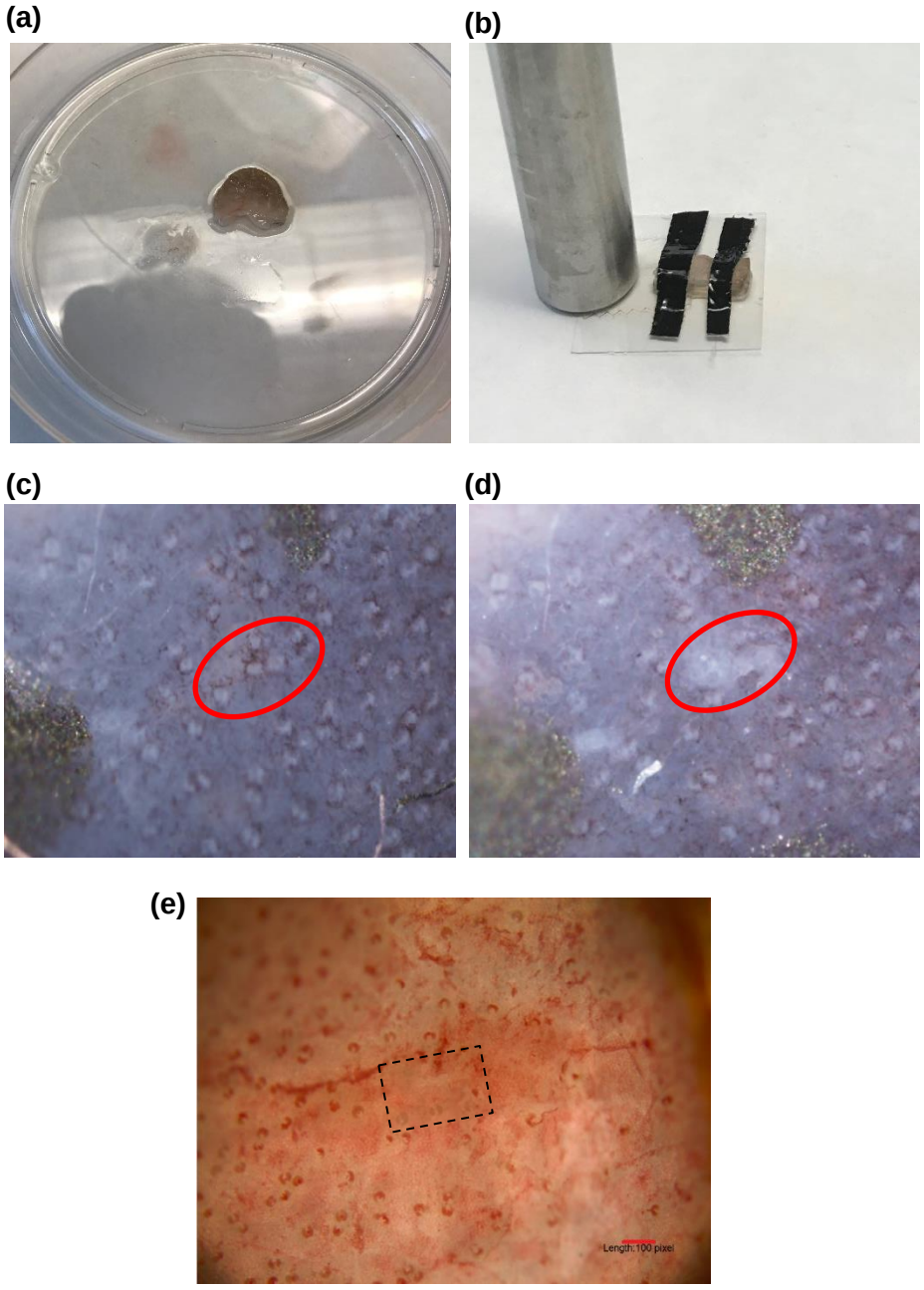


Figure 5-8: (a) Photo of the cut mouse whole ear, (b) the ear sample is backed with the hydrogel and taped on a glass substrate. (c) and (d)Mouse whole ear sample before and after LGFU treatment, treated area showing light color (less contrast) on the sebaceous glands. (e) A treated rectangular region of 450μm*300μm appeared lightened color on whole mouse ear, stained with Oil-Red-O work, scale bar 200 μm

*5.3.5 PAM guidance system*

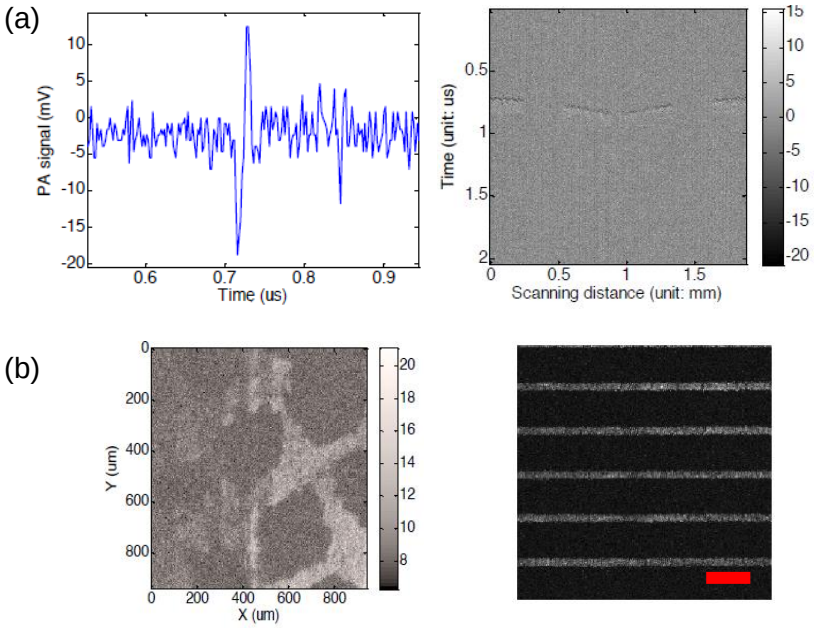


Figure 5-9: (a) Example A scan and B scan of the detected PA signal of the Cr phantom. (b) Reconstructed 2D PA image of printed black mesh grid and the Cr lines phantom, scale bar 50μm

Furthermore, we demonstrated a high resolution 2D PAM system equipped of the microring which was used in PASA system in Chapter 3. Fig. 5-10 shows the reconstructed image of phantom made of printed black mesh grid pattern with feature size of 100μm and 4μm Cr line pattern lithographed on glass. The reconstructed image is clear, and the resolution is well beyond the target for hair shaft. Also, it demonstrates the availability of imaging black target with ~100μm size, which is very close to the size of the hair shaft.

We propose to combine the two modules by sharing the same excitation laser, and since the PA lens focus is along the chief axis of the laser beam, the lateral collimation of the laser focus and the acoustic focus (the treatment point) will be naturally fulfilled. We will

remove the Galvo mirror and use the 3D scanning stage for scanning in imaging module. Although this will degrade the lateral resolution down to 50μm (which is the step size), however, it is still considered enough for our targets of scales of 100μm. During imaging, the laser will output small energy pulses below 20mJ/cm$^2$, the samples are scanned by the stage and detected by the microring, then the 2D PAM image will be reconstructed and a coordinate will be set. During treatment, the PA lens will be collimated with the center of the laser beam and the laser energy will be increased to ensure cavitation bubble clouds occurrence during the treatment. The recognized targets in the reconstructed image during imaging module will be moved by the 3D stage to the focus ellipsoid of PA lens. In this way, a personalized and selective treatment is achieved, and this is proposed to be tailored to each individual's acne distribution in clinic usage.

## 5.4 Conclusions

We have demonstrated the 2D PAM system that has resolution down to 5μm and the treatment module of the LGFU has the capability to ablate soft tissues including fat, collagen with resolution <200μm and glands vesicle structure destruction within mouse ear samples. The ablation effect dependence on power are controllable by applying different dose of ultrasound. Compared with other ablation techniques, LGFU can reach a smaller resolution non-invasively and will not induce thermal necrosis around the area, see Table 5-1.

Table 5-1: Comparison of different ablation techniques

| | LGFU | Histotripsy with | HIFU | Micro-Phakonit [135] | Laser surgery [125] |
|---|---|---|---|---|---|

| Ablation mechanism | Cavitation by focused ultrasound | Cavitation by focused ultrasound | Thermal deposition by focused ultrasound | Mechanical ablation | Cavitation by focused laser |
|---|---|---|---|---|---|
| Tool | 13-MHz Focused PA lens | Up to 1.1-MHz Piezoelectric transducer [95] | Up to 3.3-MHz Piezoelectric transducer | Micro-phakonit knife | Focused laser |
| Highest resolution on biological tissues | <200μm | >1mm | 0.6mm | 0.7mm | 70μm |
| Invasivity | Non-invasive | Non-invasive | Non-invasive | Invasive | Non-invasive |
| Imaging guidance | PAI | Ultrasound imaging | MRI, ultrasound imaging | Optical imaging | Optical imaging |

Among histotripsy (up to 1.1-MHz transducer), HIFU (up to 3.3-MHz transducer) and micro-phakonit operation, LGFU provides the highest resolution on biological tissues. This opens the possibilities for minimal malignant tissue ablation in dermatology such as acne, ophthalmology such as OSSN and some early-stage cancers in skin. The future work will be focused on *ex vivo* treatment of human skin tissues and explore the side effect such as damage on the surrounding tissue and temperature increase. Then the system combined of the imaging module and treatment module will be constructed and *in vivo* experiment on alive animal to explore the efficiency and safety of the treatment. Finally, we will study the clinic treatment effect with the help of human volunteers with acne. We believe the system will be in good clinical usage after these studies and provide a personalized and selective treatment for acne.

# Chapter 6

# Nozzle-free Jet Printing

## 6.1 Introduction

Flexible electronics is an emerging field where the functional electronic circuits are patterned on flexible plastic substrates, such as polyimide [136], poly ether ether ketone (PEEK) [137] and transparent conductive polyester film [138]. Conventional lithographic processes such as nanolithography or photolithography can be used for micro/nano patterning, but they are usually relative time-consuming and expensive. As an alternative to current lithographic processes, non-lithographic direct fabrications like inkjet printing [139] and roll-to-roll printing are preferred because of their high throughputs and good resolutions.

High resolution inkjet printing by micron-sized liquid jets is one of the most promising techniques for large-area fabrication of flexible electronics, including thin film transistors [140], photovoltaic devices [141] and organic light-emitting diodes [142]. Printed devices show advantages such as they can be printed on flexible substrate, non-lithographic, high throughputs and can be processed at relatively low temperature. Most inkjet printing mechanism is based on the incompressibility of the liquid, where a small liquid jet is pushed out of a nozzle due to the volume change induced by piezoelectric-driven

membrane deformation. Other techniques such as Electrohydrodynamic (EHD) [143] jet printing applies an electric field between the conducting nozzle tip and the substrate, the liquid inks are pulled out by the electrostatic force. EHD can achieve a very fine resolution down to 0.3μm. However, these approaches require nozzles either to eject liquids from containers or to form a concave liquid meniscus, or use conductor for applying the electric field, making these techniques vulnerable to nozzle clogging, especially when jetting inks contain flakes, particles or surface-adhesive biological molecules. Besides, EHD requires a conducting plate be placed beneath the substrate, therefore, for insulating materials or thick substrates, it can lead to bad printing quality. Researchers came up with several ways to realize jetting without nozzles to solve the problem of clogging. Most existing nozzle-free jetting mechanisms are either based on utilizing collapse of boiling bubbles induced by a focusing laser pulse onto the air-liquid interface or by applying non-focused acoustic fields into the ink. These approaches either or require optically transparent material or cannot produce thin stream and high-enough speed.

In this chapter, a new nozzle-free jet printing method is demonstrated that can realize patterning at low temperature with the help of LGFU. We take the advantage of the relative controlled manner of cavitation bubbles by LGFU to generate super-thin micro-jets at the liquid-air interface. These micro-jets have the potential to construct high resolution functional electronic structures of 2D materials such as graphene flakes and $MoS_2$. We have succeeded in printing patterned water, sumi-ink, CNT solution, graphene, and $MoS_2$ lines on paper, glass, acetate as well as PET at relative low temperature. The finest

resolution of 90μm is achieved for sumi-ink on premium paper, with substrate heated to 157℃, see Fig. 6-1.


Figure 6-1: Sumi-ink on premium paper, at 157℃, a resolution of 90μm is reached

In this chapter, we first explore the printing quality and resolution of the system demonstrated with sumi-ink, and then demonstrated the $MoS_2$ patterning on hard and soft substrates as 2D material printing. The former serves as the most studied metallic material being applied in transparent electrodes, energy storage, solar cells and flexible electronics; the latter serves as the semiconductor material that is applied in field-effect transistors (FETs), memory devices, photodetectors, solar cells and lithium ion batteries.

## 6.2 Methodology

### *6.2.1 Experiment setup and jetting mechanism*

The system consists of the previous mentioned CS/PDMS PA lens for the jetting head, a 3D-printed polylactic acid (PLA) guide as the inks container, Nd: YAG pulsed laser for excitation of the PA wave and laser shadowgraph system for jet monitor. The laser beam is expanded and illuminates the PA lens, and the lens is covered by a 3D printed polylactic-acid (PLA) container for ink storage and alignment guidance. The system is illustrated in the Fig. 6-2: Continuous cavitation bubbles is formed at the air/liquid interface as the result of the effect of the overlap between the reflected first peak of the bi-polar ultrasound and The following negative peak in the wave trail, shown in Fig. 6-3(b).

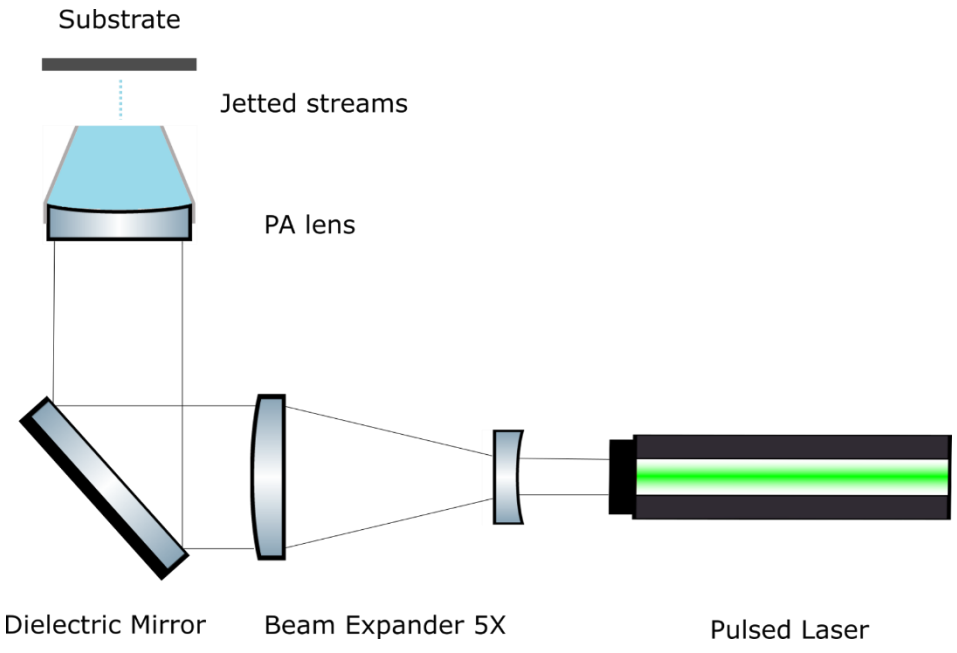


Figure 6-2: Schematic of nozzle-free jetting system

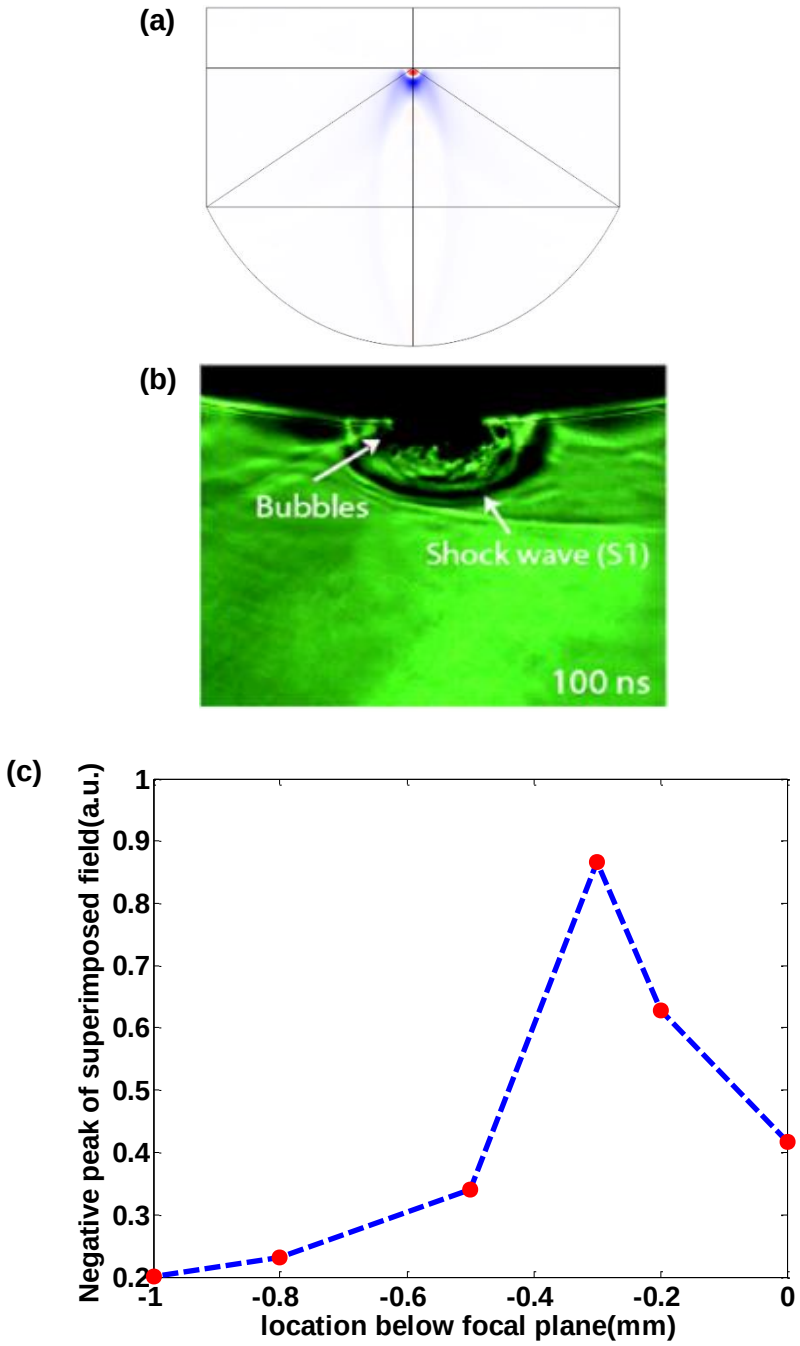


Figure 6-3: Simulation and demonstration of the superposition of negative pressure below the interface of water/air at focal plane: (a) COMSOL 5.3 acoustic simulation model. (b) Shadowgraph image showing violent cavitation events happens near the interface due to superposition effect *[150]*. (c) Negative peak pressure of the superimposed field monitored at different location below interface, at ~0.3mm, the superimposed field reaches maximum

Because of the reflection at the liquid/air interface, there exist a superimposed filed below the focal plane which is even higher than the original field. The positive half of the bipolar wave reflected at the liquid/air interface, phase shifted and changed the sign to negative, and then overlapped with the negative half of the wave. We monitored the points at different location below the liquid/air interface in simulation (Comsol 5.3) and found this superimposed field reaches the maximum at -0.3mm below the interface, shown in Fig. 6-3(c). From the simulation, it can be seen that the superimposed negative pulse below the focus is ~twice the original field at focal plane(the point at 0mm in Fig. 6-3(c) .

The superimposed negative tensile stress will exceed cavitation threshold easily because of the overlap of the two peaks. Therefore, compared to the excitation laser energy used in tissue ablation, we applied a lower light energy so that the power consumption is lowered for the printing. Compared with by utilizing just the focused ultrasound to push the liquid out without cavitation formation, the bubbles collapse will release much more energy and generate a much stronger and thinner stream, which is explained by the shock wave released upon bubble collapse. Because of the tight focusing of our technique,

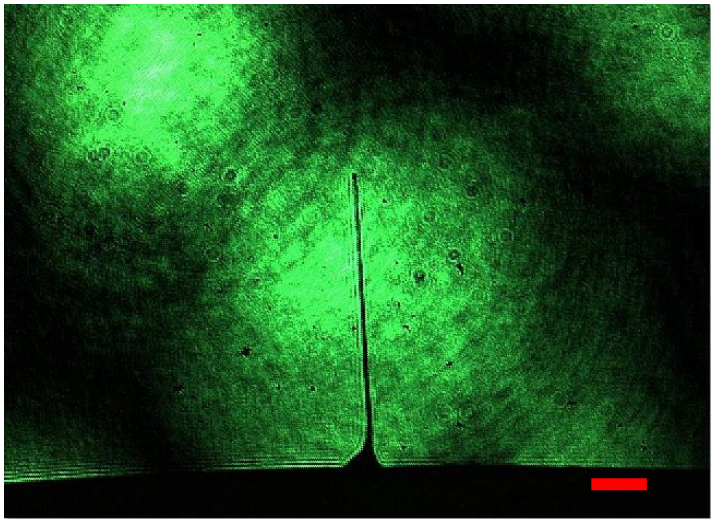

Figure 6-4: Jetted streams taken after cavitation bubble collapse, scale bar 100μm

the region that exceeds the cavitation threshold will be confined within ~100μm. An image showing the jetted stream ~10μm is shown in the Fig. 6-4.

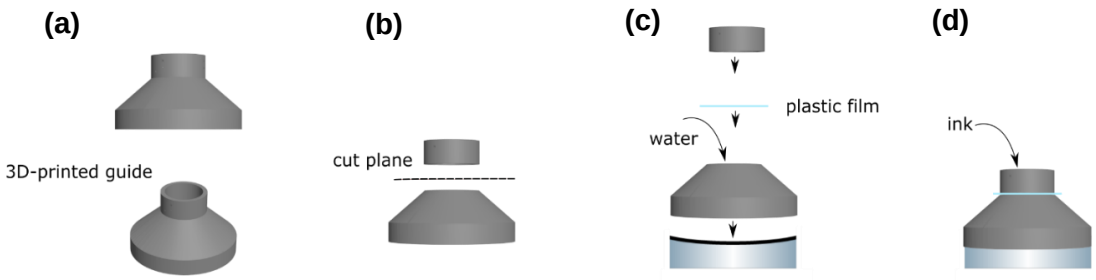


Figure 6-5: Schematic of fabrication process of the ink container guide: At first, the PLA guide is printed with 3D-printer, then the guide was cut into two part, a plastic film was inserted between; The lower part covered the PA lens and was filled with water, then the plastic film was attached to both cut parts with UV epoxy; At last the ink was injected to the top part of the guide

It's worth to mention that in case of some liquid such as 2D material inks of graphene and $MoS_2$, there exists much more ultrasound attenuation in the form of scattering and absorption, therefore, if the ink is filled up in the container, the pressure field at the focus will be much attenuated. In order for compensate this, we insert a plastic film to separate the container into two parts: the lower part filled with water and a small upper part to store the ink. Because most of the propagation is within the water, the attenuation will be minimized. A fabrication of this guide container via 3D printing is illustrated in Fig. 6-5.

In traditional inkjet printing, there is a relationship between the printing quality and a defined Z number $Z = \sqrt{\gamma \rho a}/\eta$ , in which a is nozzle diameter, $\gamma$ is surface tension and $\eta$ is the viscosity. Only when $1<Z<14$, inkjet printing is successful. It gives us an illustration of how the physical property of the ink including viscosity, boiling temperature, diffusivity and surface tension will influence the printing quality. In nozzle-free printing, we found the substrate and ink contact angle $\theta_c$, substrate temperature, and ink concentration will be the most essential factors related with the printing quality. The viscosity will influence on the cavitation threshold and the bubble collapse energy, however from our experience, it affects the jetting very little compared with inkjet printing, which maybe because the viscosity matters most on inducing frictions at the nozzle wall, but in nozzle-free case, the viscosity will not. This also suggests that the system is able to handle materials with large range of viscosity without worrying about the jetting as in inkjet printing case. To study the factors that affect printing quality and resolution, we used dilute sumi-ink in DI water at substrates of premium paper, glass and PET at different temperature.

### *6.2.2 Preparation of ink*

We referred to the $MoS_2$ and Graphene ink preparation process developed by *D. J. Finn et al* [144], the ink based on defect-free graphene and $MoS_2$ nanosheets can be produced by exfoliation of such material in organic solvent such as cyclohexanone and NMP. One advantage of these nanosheets is that they don't require thermal or chemical treatment to remove oxides. In our experiments, we used solution of $MoS_2$ in cyclohexanone for the

demonstration. The selected test substrates are glass and PET, which represents both the hard and soft substrate.

### *6.2.3 Jet stream characterization*

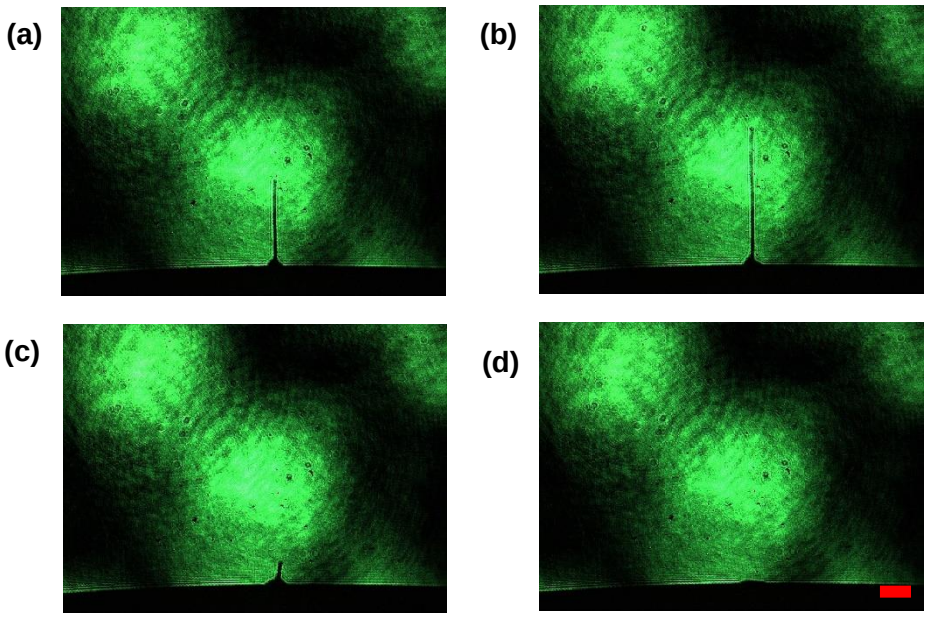


Figure 6-6: Whole process of the jetting stream captured by shadowgraph at (a) 0ms (denoted by appearance of jetting). (b) 12ms. (c) 16ms and (d) 22ms, scale bar 100 μm

The complete jetting process are jetted in form of continuous streams whose lifetime highly dependent on the input power as well as the ink property. This denotes a clear difference than the conventional inkjet printing, where inks are jetted in the form of periodic drops. The whole process of jet lasts for 0.15-0.25ms, corresponding to the cavitation bubble creation, growth, combination, collapse and disappearance. Each stage represents by a unique morphology of the jet stream. Shown in Fig. 6-6 (a) and (b), at the first several stages (0-0.12ms), the jet stream is stable and thin. It is worth to note that, the initial jetting happens 2us after the PA wave arrives the liquid/air interface. This suggests the jetting is accomplished by the cavitation bubble collapse instead of pure positive focused pressure.  The whole stream is almost of the same thickness, instead of

any spreading or drop formation the tip of the stream. At the ending stages (0.12-0.16ms) in Fig. 6-6 (c), the combined cavitation bubbles begin to collapse into small bubbles, and the jetting energy is lowered down, the shadowgraph image shows a much shorter and unstable jets. At the very end (0.16ms-) in Fig. 6-6 (d), the energy is so small that no jet can be formed instead of a vibration at the liquid surface. Therefore, the substrates should be placed at least 100 μm from the liquid surface, in order to avoid the unstable streams in the end stage to print on the substrate. The best printing distance between the substrate and liquid surface is between 500 μm to 1mm, where stable jets during the first stable stages.

Additionally, the jet stream width and maxim jetting height are almost constant with respect to different input power, indicating that the cavitation bubbles or the cavitation probability saturates fast after a threshold, which matches with our observation and previous study on cavitation probability [145]. The jet stream is almost a constant about 10μm, and this also suggests the very limit on the theoretical resolution of the system.

## 6.3 Results and Discussion

### *6.3.1 Factors influence printing quality*

We used diluted sumi-ink at different substrates to explore the printing quality of this nozzle-free jetting, and realize the drying effect, resolution and concentration influence the printing quality most.

1) Drying effect:

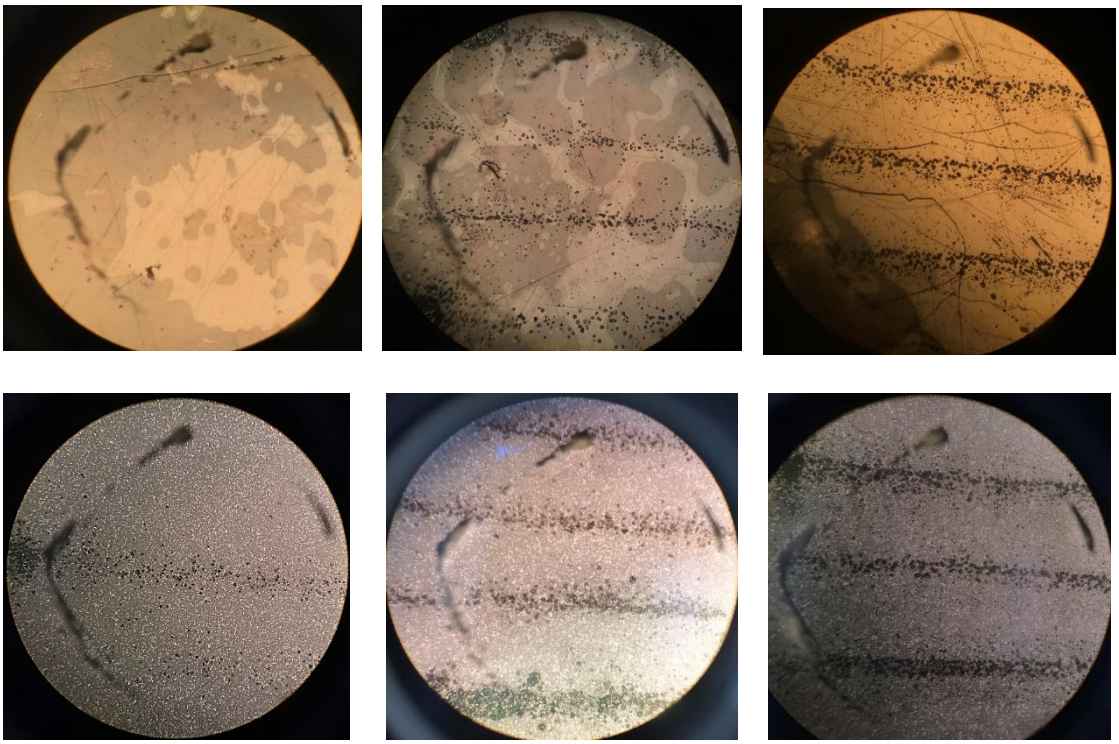

Figure 6-7: Printed sumi-ink line on PET (top) and premium paper(bottom): from the left to right, the substrate temperature was room temperature, 85℃ and 145℃, set with hot plate, scale bar 1mm

Drying is a crucial factor that impacts on printing quality in terms of uniformity and electronic property. An ideal drying process removes the solvent from the surface and promotes the adhesion between the ink and the substrate. It prevents degradation of the pattern such as broadening or liquid drop gathering. Both heating and using porous substrate help efficient drying. In Figure 6-7, we showed that at room temperature, diluted sumi ink (1:8 volume ratio of sumi ink and DI water) can be patterned on premium paper (EPSON Premium Luster Photo Paper) but cannot be patterned on PET substrate. Because of the porous structure of the paper, the solvent could permeate to lower layer, therefore, the drying was faster than the case of PET, where after printing, the ink solution gathered as liquid drops and easily flowed around before evaporation.

At an increased temperature, the pattern was printed at both paper and PET. Because the solvent evaporation was accelerated at heated substrates, inks could be deposited before degradation such as gathering into drops or broadening. At the same time, the uniformity of the printed pattern on both substrates was improved. It can be inferred that by choosing a lower boiling temperature solvent will benefit the drying efficiency.

2) Printing resolution

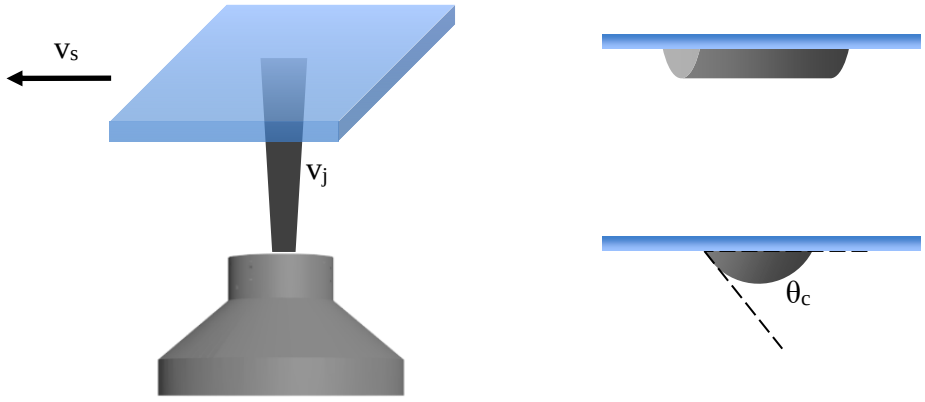


Figure 6-8: Illustration of model of line patterning on the substrate in ideal case

Under a proper drying condition, the resolution of the printing can be ideally modeled as a function of jetting stream speed $v_j$, stream cross section A, substrate moving speed $v_s$ and contact angle θc between the substrate and ink material, which is temperature and material determined. The line patterning on substrate is illustrated in the Fig. 6-8. But it is worth to note that, the resolution is degraded by other factors such as ink splash, vibration of the streams, inefficient drying, etc., which could be modified by an error function.

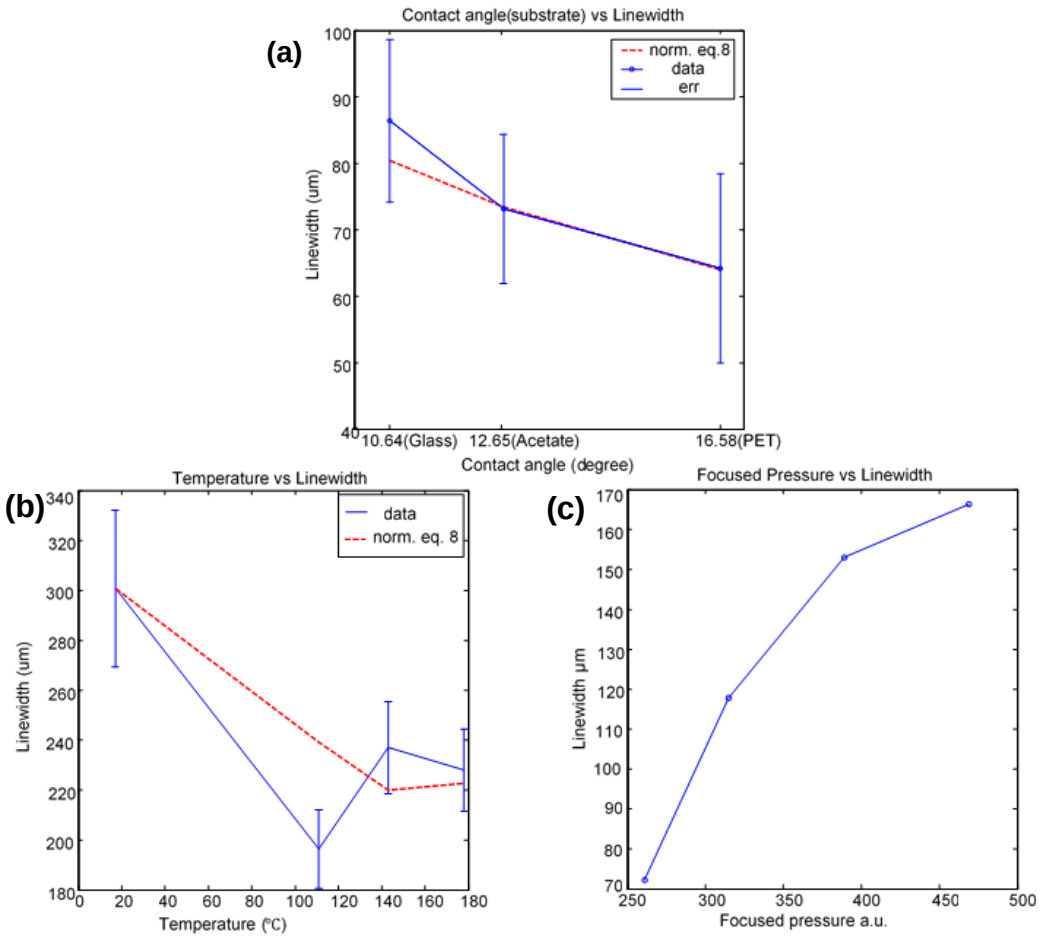


Figure 6-9: Printed linewidth dependence on (a) Substrate (contact angle), with ink of graphene/NMP of 40.43mg/ml, substrate temperature 144℃ (b) Temperature, ink of graphene/NMP of 40.43mg/ml on glass (c) Focused pressure (input laser fluence), ink of diluted sumi-ink on premium paper

The volume of the cylinder segment of ink deposited on the substrate in $\triangle$t is V $= v_j \cdot A \cdot \triangle$ t, the length of the segment is L $= v_s \cdot \triangle$ t, and the cross section of the segment is $\frac{v_j \cdot A}{v_s}$. Geometrically, the cross-section area is $\frac{w^2}{4}\left(\frac{0.0175\theta_c}{\sin \theta_c{}^2} - \frac{1}{\tan \theta_c}\right)$, where w is the resolution or the linewidth. Finally, the resolution can be estimated as

$$w = 2\sqrt{\frac{v_j \cdot A}{v_s \cdot \left(\frac{0.0175\theta_c}{\sin \theta_c{}^2} - \frac{1}{\tan \theta_c}\right)}} \tag{14}$$

Here, we conclude that, thinner stream, smaller jetting speed, faster substrate moving speed and larger contact angle will results in a higher resolution and therefore smaller linewidth. And the contact angle of solid-liquid interface will be a function of temperature and surface tension of both ink and substrate, given by Young's equation $\cos\theta_c = \frac{\gamma_{SG}-\gamma_{SL}}{\gamma_{LG}}$, where γ is the interfacial tension and the subscripts SG, SL and LG refer to solid gas interface, solid liquid interface and liquid gas interface, of all the three terms are temperature dependent.

From a series of study on the linewidth dependence on several parameter of the system, we prove the validity of the proposed model. From 5.9(a), the linewidth ratio of contact angle agreed with the prediction in the equation 8 by normalizing the linewidth at 10.84° to experimental data. From 5.9(b), the temperature influences the linewidth by changing the contact angle and drying speed. At room temperature, the contact angle is small and linewidth but it's worth to note that the contact angle did not change much at high temperature, and the experimental data coordinate with the prediction of equation 8 by normalizing the linewidth at 17℃, and all the contact angle at corresponding temperature were recorded. For 5.9(c), it is understood that as the higher focused pressure induces more cavitation bubbles, then more bubble collapse energy jets more volume of the ink.

3) Other factors:

Except for the factors mentioned above that can affect the printing quality, concentration of the ink needs to be selected carefully. For too much concentrated

solution, the ink in the storage guide will get clogged and impede the ultrasound propagation and the following bubble formation, and the jetted stream becomes unstable, therefore the printed lines are not uniform and discontinuous. On the contrary, for too much diluted solution, the drying of the solvent will be slow, which not only requires a longer drying time, but also sacrifice the resolution. Additionally, due to the relative unstable nature of the cavitation bubble collapse, the printed lines can be discontinuous. This can be alleviated by scanning the pattern repeatedly. Fig. 6-11 shows that for a single scan of undiluted sumi-ink, the printed pattern lines are broken, however, by scanning the line repeatedly for several times, the broken points in the line can be compensated. When scanning the same line pattern at same location for 5 times, the printed line is intact without broken.

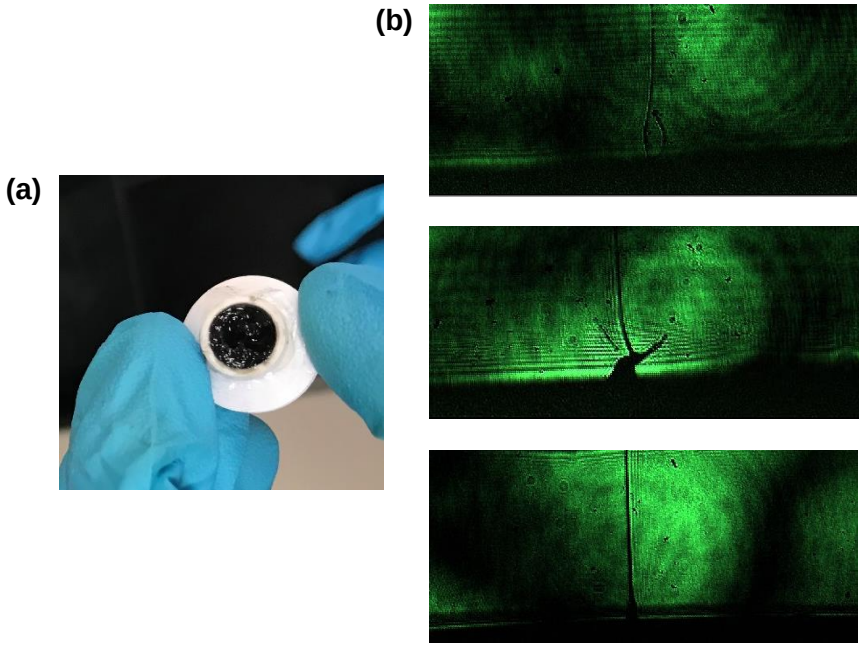


Figure 6-10: (a) photo showing clogging happens at high concentrated ink of graphene/NMP 40.38mg/ml. (b) top and middle shows the unstable jetting due to the

clogging inside the ink container, demonstrated with high concentrated graphene/NMP ink in (a), the bottom shows a well-mixed sumi-ink jetted from container.

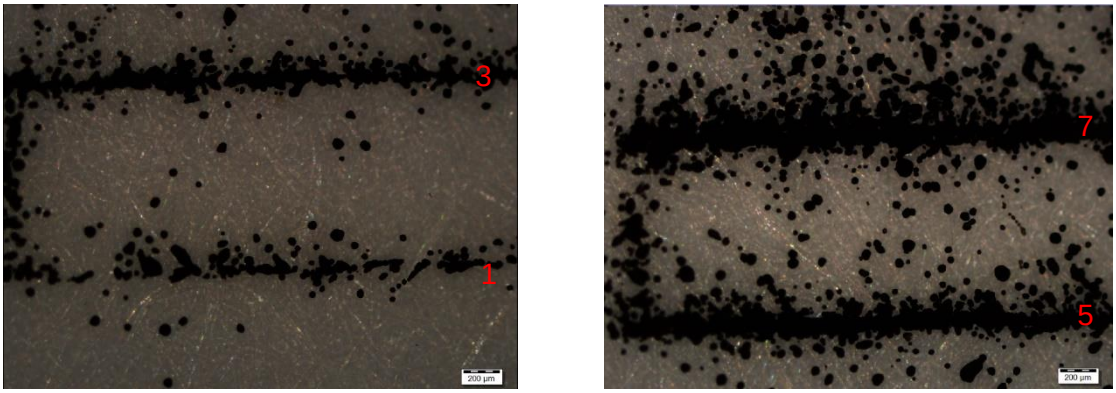


Figure 6-11: sumi-ink printed on premium paper, 144℃, when the same line was scanned at the same position for 1, 3 ,5 and 7 times, marked in the picture, when the line was repeated for 5 times, the line is not broken anywhere along the line

### *6.3.2 Printing results of $MoS_2$/cyclohexanone*

In this section, we demonstrated the printing of 2D materials of $MoS_2$/cyclohexanone on premium paper, glass and PET, which is widely used substrates for flexible electronics. Because of the high boiling temperature for cyclohexanone, and small contact angle, the ink will be quickly wetted on to the substrate and difficult for pattern formation at room temperature. We heated the substrates to 144℃ to accelerate the evaporation of the solvent and so as the drying process. A 200μm lines can be printed on paper. On PET and glass, we also demonstrate the printing with same condition, however, due to the slow drying process compared to porous paper substrates, the $MoS_2$ lines were wider than that on paper, see Fig. 6-12.

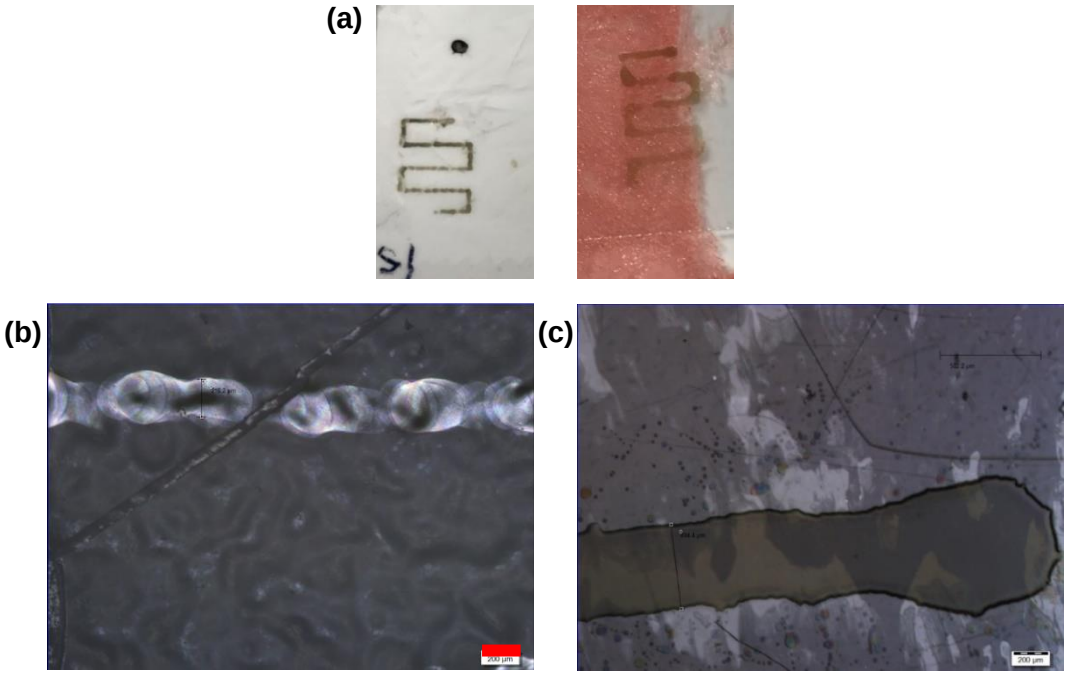


Figure 6-12: Printed $MoS_2$/cyclohexanone lines on paper and PET substrate at 250°C, and imaged with microscope 5X magnification, (a) $MoS_2$ printed lines on paper(left) and PET (right) with different average speed; (b) $MoS_2$ printed lines on paper; (c) $MoS_2$ printed lines on PET

## 6.4 Conclusions

In this chapter, we demonstrated the capability of the nozzle-free micro-jetting system achieved by laser generated focused ultrasound technologies using CS/PDMS PA lens and studied the jetting process. We concluded that the printing quality can be characterized by the drying of the ink and modeled the printing quality with a simplified cylindrical segment dependent on the jetting stream velocity, diameter(area), substrate moving speed and the contact angle. We demonstrated the printing of 2D material of $MoS_2$/cyclohexanone on substrates including paper, acetate, glass and PET at a relative low temperature. The future direction of the study is focused on study of the ink that provide the best uniformity and drying efficiency, and the substrate that provides good wetting and large contact angle to

improve the resolution. We will also optimize the jetting system to generate a more stable jets by control the liquid surface more accurately and the laser power more constant. We believe the technology has a good potential to fill the gap in the nozzle-free jet printing fields with resolutions of ~100μm level.

# Chapter 7

# Conclusions and Future Work

## 7.1 Conclusions

This thesis mainly discusses about the PA-based technologies including photoacoustic spectrum analysis and laser-generated-focused-ultrasound with its unique applications. The PASA equipped with micro-ring ultrasound detector, for the first time, is able to characterize cellular-size tissues (<6μm), by taking the advantage of the broad acoustic response bandwidth of microring. The system is applied to differentiating the shape difference of aged red blood cells and fresh red blood cells from analysis of the photoacoustic spectrum.

The LGFU, on the other hand, utilize the tight focusing of the photoacoustic wave and cavitation effect to achieve soft-tissue ablation and nozzle-free jet printing. We demonstrated the potential for selective and accurate treatment of acne and high-resolution jet printing of 2D materials. The problems need to be solved on the LGFU for acne treatment is mainly the treatment period is long limited by the repetition rate of the excitation laser. However, we are able to scale up the collapse energy and repetition rate by using a higher power, high repetition rate laser. Towards the printing applications, the challenge lies on the stability of jet stream which is highly dependent on the uniformity

and consistency of the input laser power from pulse to pulse. Also, we propose to build a database for the collection of most appropriate pair of ink and substrates for this technique. Considering the problems, we are coming up the following strategies to optimize the system as well as discussing about the future applications.

## 7.2 Future work

The section will be divided into two parts, first is the optimization of the current systems, second is the extended applications of the technologies.

### *7.2.1 System optimization*

For the PASA system, the sensitivity mainly depends on the ultrasound detector—microring's response to pressure, photodetector sensitivity and input light intensity. A larger sensitivity can be achieved if the input light of the microring is increased, therefore, a higher power tunable laser will benefit the sensitivity. At the same time, a lowered noise or larger gain photodetector also helps to the improve the system SNR. The improved SNR will help us release the requirement for averaging, therefore, increase the analysis speed of the system.

For LGFU techniques, the uniformity of the CS/PDMS layer deposition can be further optimized by using the flame spreader, which will flatten and spread the flame tip. Additionally, a higher power laser source and a higher repetition rate will enhance the ablation effect and make the treatment much faster.

Towards the jet printing experiments, however, we don't need to pursue a higher power, since the interference effect can help to achieve cavitation effect with a smaller generated PA wave. The system will be optimized by making a more stable laser pulse energy, by controlling the liquid surface height stable, and by using a circulation system to refresh the inks or solutions. The circulation is important for removing the generated bubbles in the solution immediately. Moreover, a more reliable packaging method to insert the plastic film in the PLA guide is preferable.

### *7.2.2 Future applications*

1) Cell disease detection microchannel chip

For the PASA, we propose it as a fast analysis tool to be used in flow cytometry with the help of microfluids technologies. A schematic is shown in the figure below. A PDMS guide will be used for the samples to flow across. It can be used to characterize the blood freshness, blood disease including anemia and circulating cancer cells (CTCs). The anemia will change the healthy biconcave shape red blood cells into irregular shapes, therefore the spectrum of the PA signal and the slope of the regression will show a difference. CTCs is important because there is current effective and sensitive way for detecting CTCs, mostly because the total number of circulating cancers are very rare. Since PASA provides a sensitive detection of the PA signals' change, it can be used for CTCs detection. Besides, cell counting, and size-comparing of optical absorbers will also be goals for PASA. A schematic showing the detection system is illustrated as below: A PDMS microchannel was fabricated above the microring chip, and a fiber is used to illuminate the central flow

channel. The excited PA signals will propagate downward and analyzed by the microring, therefore, to realize a fast detection of diseases or characterizing the cells shape and sizes.

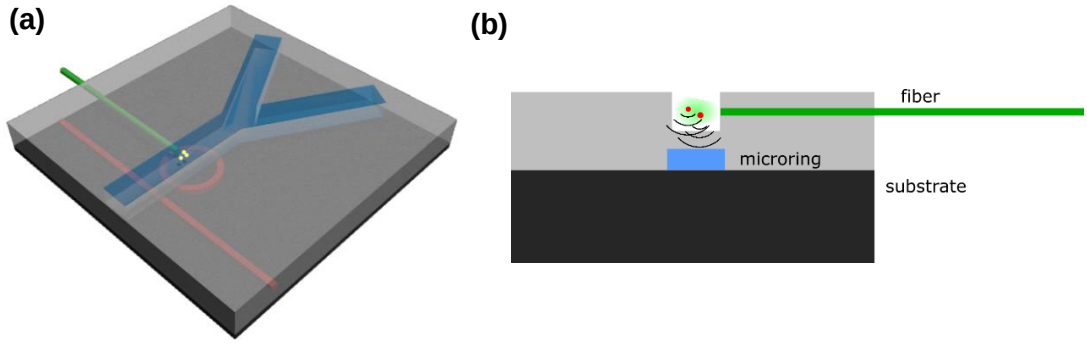


Figure 7-1: A PASA-based microfluidic channel disease detection system: (a) A PDMS microfluidic channel on microring chip, an optical fiber is inserted and illuminating the fluid for PA signal generation; (b)cross-section view of the microfluidic channel, the chromophores in the fluids generate PA signal, detected by the microring and analyzed by PASA for characterization

2) Acne treatment and other surface malignant tissue treatment

We've demonstrated *in vitro* and *ex vivo* experiments for both the treatment module and the 2D high resolution PAM imaging guidance module. However, the next step will be focused on combination of the two module and in *vivo* experiment on animal and then human volunteers. Even though an evaluation of oil amount under skin is one way to quantitate the treatment effect, it's difficult to tell the final turn-out of the treatment of acne. Moreover, side-effects and pain evaluation also need volunteers. Besides selective acne treatment, this non-invasive ablation technique also has the potential to treat OSSN and spider veins for cosmetics. Both disorder of unwanted neoplasia or veins are superficial tissues and can be mechanical ablated. Current treatment towards both issues either are expensive or can be effectiveness depend on cases.

3) Nozzle-free printing of functional device

For the nozzle-free jetting, we have already tested the printing of $MoS_2$ and graphene, which are semiconductor material and conducting material. We propose to demonstrate the system capability to print simple structures of a simple photodetector and an ohmic contact and study the electronic properties in the next step. In the future, a deep study of the proper ink for this technique will be conducted, including exploration of the boiling temperature, surface tension and viscosity's effect on resolution and drying effect. Also, we propose to print functional devices for potential applications such as thin film transistors, OLEDs, and so on.

4) Needless injection

Except for the current applications, we also propose a needless injection system. Despite the common use of needles and syringes for injection, needle-based methods come along with such as needle phobia, accidental needle-stick injury and reuse of needles and syringes, which leads to potential HIV and HBV infections. Therefore, needleless delivery is desirable for reasons including: improved safety, better compliance with immunization schedules, reduced injection site pain, easier and faster delivery and reduced cost. Conventional needleless liquid jet injectors have been used for parenteral delivery of vaccines and drugs to relieve some of the above problems [146, 147]. These injectors deliver liquid vaccine through a nozzle orifice and use a high-speed and micro-size thin liquid jet to penetrate the human skins. Compared to needle injection, jet injectors have proven an improved or at least equivalent immune responses. Jet injectors have been applied for gene delivery, insulin delivery, mass immunizations. However, due to the

nature of nozzle-based delivery, jet injectors are facing problems such as nozzle clogging, therefore injection failure and contamination will happen. The clogging will be severe during the injection of highly viscous solutions or large bio-molecules.

Because the jetting stream of LGFU mentioned above is thin and high-speed, the LGFU system is capable of needleless injection of large molecules or viscous solution. The injection mechanism is illustrated as shown in the following picture [146]. The picture shows four stages that describe how the jet streams are injected into the human skin model (represented by the top rectangular)

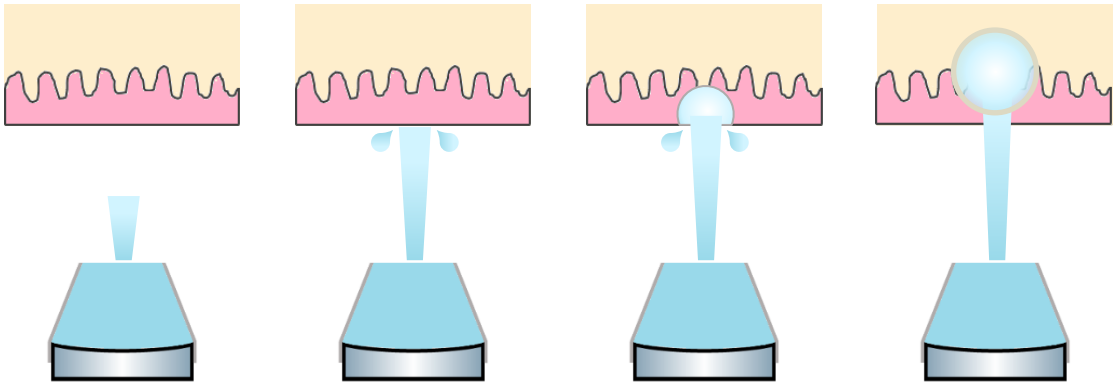

Figure 7-2: Schematic of the mechanism of needleless injection

At the beginning, the high-speed (>100m/s [146]) jet initiates a formation of hole in the skin through erosion/fracture or other skin failure modes. Then a continued impingement of the jet increases the depth of the hole. As the hole becomes deeper, the liquid accumulated in the hole slows down the incoming jet and the hole growth stopped, thus an equilibrium state is reached. At the end, the stagnation of jet disperses the liquid into the skin in a near-spherical shape. The speed of the stream is estimated by $v = \sqrt{2p/\rho}$ [148],

where the p is given by the pressure on the streams from the collapse of bubble, which is in the order of 30MPa, therefore, giving an estimated speed of ~244m/s, which fulfill the requirement for successful needless injection. Additionally, due to the short period of each jet stream, we expect less pain would be expected compared to existing jet injection methods. Last but not least, the waste of materials will be minimized because only a tiny amount of solution will be jetted, which helps to lower down the cost of medication when using expensive medicines or vaccines.

As a conclusion, the PA-related technologies have been applied to more areas other than conventional medical imaging fields. Additionally, the above studied PA technologies can be integrated easily into any other optical or PA systems, therefore, can accelerate the PA therapy and related technologies development more. I believe our studies will trigger more exploration of the PA effect and open up more possibilities in industry of printing and medical applications.

# Bibliography


[1] D. A. Hutchins, "Mechanisms of pulsed photoacoustic generation," *Canadian Journal of Physics,* vol. 64, pp. 1247-1264, 1986.

[2] M. Xu, and L. V. Wang, "Photoacoustic imaging in biomedicine," *Review of Scientific Instruments,* vol. 77, 2006.

[3] X. Wang, Y. Pang, G. Ku, X. Xie, G. Stoica, and L. V. Wang, "Noninvasive laser-induced photoacoustic tomography for structural and functional in vivo imaging of the brain," *Nature Biotechnology,* vol. 21, pp. 803-806, 2003.

[4] D. W. Ball, "Photoacoustic Spectroscopy," *Spectroscopy,* vol. 21, 2006.

[5] T. Feng, Q. Li, C. Zhang, G. Xu, L. J. Guo and X. Wang, "Characterizing cellular morphology by photoacoustic spectrum analysis with an ultra-broadband optical ultrasonic detector," *Optics Express,* vol. 24, pp. 19853-19862, 2016.

[6] L. Berquez, D. Marty-Dessus, and J. F. Franceschi, "Defect detection in silicon wafer by photoacoustic imaging," *Japanese Journal of Applied Physics,* vol. 42, 2003.

[7] H. Baac, J. G. Ok, A. Maxwell, K. Lee, Y. Chen, A. J. Hart, Z. Xu, E. Y, and L. J. Guo, "Carbon-nanotube optoacoustic lens for focused ultrasound generation and high-precision targeted therapy," *Scientific Reports,* vol. 2, p. 989, 2012.

[8] C. Zhang, K. Maslov, J. Yao, and L. V. Wang, "In vivo photoacoustic microscopy with 7.6-μm axial resolution using a commercial 125-MHz ultrasonic transducer," *Journal of Biomedical Optics*, vol. 17, p. 116016, 2012.

[9] L. Zhu, L. Li, L. Gao, and L. V. Wang, "Multi-view optical resolution photoacoustic microscopy," *Optica*, vol. 1, pp. 217-222, 2014.

[10] C. Zhang, T. Ling, S. Chen, and L. J. Guo, "Ultrabroad bandwidth and highly sensitive optical ultrasonic detector for photoacoustic imaging," *ACS Photonics*, vol. 1, pp. 1093-1098, 2014.

[11] J. Yao, and L. V. Wang, "Photoacoustic microscopy," *aser & Photonics Reviews*, vol. 7, pp. 758-778, 2013.

[12] T. Chaigne, B. Arnal, S. Vilov, E. Bossy, and O. Katz, "Super-resolution photoacoustic imaging via flow-induced absorption fluctuations," *Optica*, vol. 4, pp. 1397-1404, 2017.

[13] J. Xia, J. Yao, and L. V. Wang, "Photoacoustic tomography: principles and advances," *Progress in Electromagnetics Research*, vol. 147, pp. 1-22, 2014.

[14] S. Oladipupo, S. Hu, A. Santeford, J. Yao, J. Kovalski, R. Shohet, K. Maslov, L. V. Wang, and J. M. Arbeit,, "Conditional HIF-1 induction produces multistage neovascularization with stage-specific sensitivity to VEGFR inhibitors and myeloid cell independence," *Blood*, vol. 117, pp. 4142-4153, 2011.

[15] R. Bitton, R. Zemp, J. Yen, L. V. Wang, and K. Shung, "A 3-D high-frequency array based 16 channel photoacoustic microscopy system for in vivo micro-

vascular imaging," *IEEE Transactions Medical Imaging,* vol. 28, pp. 1190-1197, 2009.

[16] J. Xia, and L. V. Wang, "Small-animal whole-body photoacoustic tomography: a review," *IEEE Transactions on Biomedical Engineering,* vol. 61, pp. 1380-1389, 2014.

[17] J. Staley, P. Grogan, A. K. Samadi, H. Cui, M. S. Cohen, and X. Yang, "Growth of melanoma brain tumors monitored by photoacoustic microscopy," *Journal of Biomedical Optics,* vol. 15, p. 040510, 2010.

[18] S. Chen, T. Ling, S. Huang, H. Baac, and L. J. Guo, "Photoacoustic correlation spectroscopy and its application to low-speed flow measurement," *Optics Letters,* vol. 35, pp. 1200-1202, 2010.

[19] H. Cui, and X. Yang, "In vivo imaging and treatment of solid tumor using integrated photoacoustic imaging and high intensity focused ultrasound system," *Medical Physics,* vol. 37, pp. 4777-4781, 2010.

[20] A. de la Zerda, Z. Liu, S. Bodapati, R. Teed, S. Vaithilingam, B. T. Khuri-Yakub, X. Chen, H. Dai, and S. S. Gambhir, "Ultrahigh sensitivity carbon nanotube agents for photoacoustic molecular imaging in living mice," *Nano Letters,* vol. 10, pp. 2168-2172, 2010.

[21] L. Li, H. Zhang, R. J. Zemp, K. Maslov, and L. V. Wang, "Simultaneous imaging of a lacZ-marked tumor and microvasculature morphology in vivo by dual-wavelength photoacoustic microscopy," *Journal of Innovative Optical Health Sciences,* vol. 1, pp. 207-215, 2008.

[22] M. Li, J. Wang, J. A. Schwartz, K. L. Gill-Sharp, G. Stoica, and L. V. Wang, "In-vivo photoacoustic microscopy of nanoshell extravasation from solid tumor vasculature,," *Journal of Biomedical Optics,* vol. 14, p. 010507, 2009.

[23] M. Li, J. Oh, X. Xie, G. Ku, W. Wang, C. Li, G. Lungu, G. Stoica, and L. V. Wang, "Simultaneous molecular and hypoxia imaging of brain tumors in vivo using spectroscopic photoacoustic tomography," *Proceedings of the IEEE,* vol. 96, pp. 481-489, 2008.

[24] R. Olafsson, D. R. Bauer, L. G. Montilla, and R. S. Witte, "Real-time, contrast enhanced photoacoustic imaging of cancer in a mouse window chamber," *Optics Express,* vol. 18, pp. 18625-18632, 2010.

[25] S. Hu, K. Maslov, V. Tsytsarev, and L.V. Wang, "Functional transcranial brain imaging by optical-resolution photoacoustic microscopy," *Journal of Biomedical Optics,* vol. 14, p. 040503, 2009.

[26] X. Wang, G. Ku, M. A. Wegiel, D. J. Bornhop, G. Stoica, and L. V. Wang, "Noninvasive photoacoustic angiography of animal brains in vivo with near-infrared light and an optical contrast agent," *Optics Letters,* vol. 29, pp. 730-732, 2004.

[27] L. Liao, M. Li, H. Lai, Y. Shih, Y. Lo, S. Tsang, P. Chao, C. Lin, F. Jaw, and Y. Chen, "Imaging brain hemodynamic changes during rat forepaw electrical stimulation using functional photoacoustic microscopy," *Neuroimage,* vol. 52, pp. 562-570, 2010.

[28] V. Tsytsarev, S. Hu, J. Yao, K. Maslov, D. L. Barbour, and L. V. Wang, "Photoacoustic microscopy of microvascular responses to cortical electrical stimulation," *Journal of Biomedical Optics,* vol. 16, p. 076002, 2011.

[29] M. Nasiriavanaki, J. Xia, H. Wan, A. Q. Bauer, J. P. Culver, and L. V. Wang, "High-resolution photoacoustic tomography of resting-state functional connectivity in the mouse brain," *Proceedings of the National Academy of Silences of the United States of America,* vol. 111, pp. 21-26, 2014.

[30] F. V. Subach, L. Zhang, T. Gadella, N. G. Gurskaya, K. A. Lukyanov, and V. V. Verkhusha, "Red fluorescent protein with reversibly photoswitchable absorbance for photochromic FRET," *Chemistry & Biology,* vol. 17, pp. 745-755, 2010.

[31] S. Jiao, M. Jiang, J. Hu, A. Fawzi, Q. Zhou, K. Shung, C.A. Puliafito, and H. Zhang, "Photoacoustic ophthalmoscopy for in vivo retinal imaging," *Optics Express,* vol. 18, pp. 3967-3972, 2010.

[32] R. H. Silverman, F. Kong, Y. Chen, H. Lloyd, H. Kim, J. M. Cannata, K. Shung, and D. J. Coleman, "High-resolution photoacoustic imaging of ocular tissues," *Ultrasound in Medicine& Biology,* vol. 36, pp. 733-742, 2010.

[33] W. Song, Q. Wei, T. Liu, D. Kuai, J. M. Burke, S. Jiao, and H. Zhang, "Integrating photoacoustic ophthalmoscopy with scanning laser ophthalmoscopy, optical coherence tomography, and fluorescein angiography for a multimodal retinal imaging platform," *Journal of Biomedical Optics,* vol. 17, p. 061206, 2012.

[34] H. Zhang, K. Maslov, M. Li, G. Stoica, and L. V. Wang, "In vivo volumetric imaging of subcutaneous microvasculature by photoacoustic microscopy," *Optics Express*, vol. 14, pp. 9317-9323, 2006.

[35] C. P. Favazza, L. A. Cornelius, and L.V. Wang, "In vivo functional photoacoustic microscopy of cutaneous microvasculature in human skin," *Journal of Biomedical Optics*, vol. 16, p. 026004, 2011.

[36] C. Favazza, O. Jassim, L.V. Wang, and L. Cornelius, "In vivo photoacoustic microscopy of human skin," *Journal of Investigative Dermatology*, vol. 130, p. S145, 2011.

[37] L. Song, K. Maslov, K. Shung, and L. V. Wang, "Ultrasound-array-based real-time photoacoustic microscopy of human pulsatile dynamics in vivo," *Journal of Biomedical Optics*, vol. 15, p. 021303, 2010.

[38] J. Yao, K. I. Maslov, E. R. Puckett, K. J. Rowland, B. W. Warner, and L. V. Wang, "Double-illumination photoacoustic microscopy," *Optics Letters*, vol. 37, pp. 659-661, 2012.

[39] A. Taruttis, E. Herzog, D. Razansky and V. Ntziachristos, "Real-time imaging of cardiovascular dynamics and circulating gold nanorods with multispectral optoacoustic tomography," *Optics Express*, vol. 18, pp. 19592-19602, 2010.

[40] K. Narayanan, S. Chandani, T. Ramakrishna, and Ch. Mohan Rao, "Depth profiling of mammalian cells by photoacoustic spectroscopy: localization of ligands," *Biophysical Journal*, vol. 72, pp. 2365-2368, 1997.

[41] R. Bugs, and M. L. Cornélio, "A new biophysics approach using photoacoustic spectroscopy to study the DNA-ethidium bromide interaction," *European Biophysics Journal,* vol. 31, pp. 232-240, 2002.

[42] C. Lin, L. Cao, J. Wang, W. Zheng, Y. Chen, Z. Feng, A. Li, and J. Zhou, "Ultrasonic spectrum analysis for in vivo characterization of tumor microstructural changes in the evaluation of tumor response to chemotherapy using diagnostic ultrasound," *BMC Cancer,* vol. 13, p. 302, 2013.

[43] I. Varghese, and C. Cetinkaya, "Noncontact Photo-acoustic defect detection in drug tablets," *Journal of Pharmaceutical Sciences,* vol. 96, pp. 2125-2133, 2007.

[44] H. Baac, J. Ok, H. Park, T. Ling, S. Chen, A. J. Hart, and L. J. Guo, "Carbon nanotube composite optoacoustic transmitters for strong and high frequency ultrasound generation," *Applied Physics Letters,* vol. 97, p. 234104, 2010.

[45] H. Baac, J. Ok, T. Lee, and L. J. Guo, "Nano-structural characteristics of carbon nanotube-polymer composite films for high-amplitude optoacoustic generation," *Nanoscale,* vol. 7, pp. 14460-14468, 2015.

[46] W. Chang, W. Huang, J. Kim, S. Li, and X. Jiang, "Candle soot nanoparticles-polydimethylsiloxane composites for laser ultrasound transducers," *Applied Physics Letters,* vol. 107, p. 161903, 2015.

[47] J. Heremans, I. Rahim, and M. S. Dresselhaus, "Thermal-conductivity and Raman-spectra of carbon-fibers," *Physical Review B,* vol. 32, pp. 6742-6747, 1985.

[48] S. Park, S. Yang, M. S. Ahn, Y. Oh, Y. Kim, and K. Jeong, "Plasmon enhanced photoacoustic generation from volumetric electromagnetic hotspots," *Nanoscale,* vol. 8, pp. 757-761, 2016.

[49] H. Yang, J. Kim, S. Ashkenazi, M. O'Donnell, and L. J. Guo, "Optical generation of high frequency ultrasound using two-dimensional gold nanostructure," *Applied Physics Letters,* vol. 89, p. 093901, 2006.

[50] W. Chan, T. Hies, and C. D. Ohl, "Laser-generated focused ultrasound for arbitrary waveforms," *Applied Physics Letters,* vol. 109, p. 174102, 2016.

[51] S. Noimark, R. J. Colchester, B. J. Blackburn, E. Z. Zhang, E. J. Alles, S. Ourselin, P. C. Beard, L. Papakonstantinou, I. P. Parkin, and A. E. Desjardins, "Carbon-nanotube-PDMS composite coatings on optical fibers for all-optical ultrasound imaging," *Advanced Functional Materials,* vol. 26, pp. 8390-8396, 2016.

[52] M. D. Brown, J. Jaros, B. T. Cox, and B. E. Treeby, "Control of broadband optically generated ultrasound pulses using binary amplitude holograms," *Journal of the Acoustical Society of America,* vol. 139, pp. 1637-1647, 2016.

[53] K. Kieran, T. L. Hall, J. E. Parsons, J. S. Wolf Jr., J. B. Fowlkes, C. A. Cain, and W. W. Roberts, "Refining histotripsy: defining the parameter space for the creation of nonthermal lesions with high intensity, pulsed focused ultrasound of the in vitro kidney," *The Journal of Urology,* vol. 178, pp. 672-676, 2007.

[54] Z. Xu, J. B. Fowlkes, A. Ludomirsky, and C. A. Cain, "Investigation of intensity thresholds for ultrasound tissue erosion," *Ultrasound in Medicine and Biology,* vol. 31, pp. 1673-1682, 2005.

[55] T. Lee, W. Luo, Q. Li, H. Demirci, and L. J. Guo, "Laser-induced focused ultrasound for cavitation treatment: toward high-precision invisible sonic scalpel," *Small,* vol. 13, p. 1701555, 2017.

[56] L. M. Lyamshev, and K. A. Naugolnykh, "Optical-generation of sound-non-linear effects," *Soviet Physics Acoustics,* vol. 27, p. 357, 1981.

[57] M. W. Sigrist, and F. K. Kneubühl, "Laser-generated stress waves in liquids," *The Journal of the Acoustical Society of America,* vol. 64, p. 1652, 1978.

[58] H. M. Lai, and K. Young, "Theory of the pulsed optoacoustic technique," *The Journal of the Acoustical Society of America,* vol. 72, p. 2000, 1982.

[59] E. F. Carome, N. A. Clark, and C. E. Moeller, "Generation of acoustic signals in liquids by ruby laser-induced thermal stress transients," *Applied Physics Letters,* vol. 4, p. 95, 1964.

[60] G. J. Diebold, T. Sun and M. I. Khan, "Photoacoustic Monopole Radiation in one, two, and three dimensions," *Physical Review Letters,* vol. 67, pp. 3384-3387, 1991.

[61] L. M. Lyamshev, "Opotoacoustic sources of sound," *Soviet Physics Uspekhi*, vol. 24, pp. 997-995, 1981.

[62] G. V. Ostrovskaya, and A. N. Zaĭdel, "Laser spark in gases," *Soviet Physics Uspekhi,* vol. 16, pp. 834-855, 1974.

[63] C. G. Morgan, "Laser-induced breakdown phenomena," *Science Progress,* vol. 65, pp. 31-50, 1978.

[64] R. G. Brewer, and K. E. Rieckhoff, "Stimulated brillouin scattering in liquids," *Physical Review Letters,* vol. 13, p. 334, 1964.

[65] D. C. Emmony, "Interaction of IR laser radiation with liquids," *Infrared Physics,* vol. 25, pp. 133-139, 1985.

[66] N. Bloembergen, "Laser-induced electric breakdown in solids," *IEEE Journal of Quantum Electronics,* vol. 10, pp. 375-386, 1974.

[67] S. R. J. Brueck, H. Kildal, and L. J. Belanger, "Photo-acoustic and photo-refractive detection of small absorptions in liquids," *Optics Communications,* vol. 34, pp. 199-204, 1980.

[68] C. K. N. Patel, and A. C. Tam, "Pulsed optoacoustic spectroscopy of condensed matter," *Reviews of Modern Physics,* vol. 53, p. 517, 1981.

[69] L. V. Wang, and H. Wu, Biomedical Optics: principles and imaging, John Wiley & Sons,, 2007.

[70] B. Lautrup, Physics of Continuous Matter: Exotic and Everyday Phenomena in the Macroscopic World 2nd Edition, CRC Press , 2011.

[71] J. E. Kennedy, "High-intensity focused ultrasound in the treatment of solid tumors," *Nature Reviews Cancer,* vol. 5, pp. 321-327, 2005.

[72] Q. F. Zhou, C. Sharp, J. M. Cannata, and K. K. Shung, "Self-focused high frequency ultrasonic transducers based on ZnO piezoelectric films," *Applied Physics Letters,* vol. 90, p. 113502, 2007.

[73] C. Chang, K. Firouzi and K. Park, "Acoustic lens for capacitive micromachined ultrasonic transducers," *Journal of Micromechanics and Microengineering,* vol. 24, p. 85007, 2014.

[74] L. Zigoneanu, B. Popa, and S. A. Cummer, "Design and measurements of a broadband two-dimensional acoustic lens," *Physical Review B,* vol. 84, p. 024305, 2011.

[75] M. Frenz, G. Paltauf, and H. Schmidt-Kloiber, "Laser-generated cavitation in absorbing liquid induced by acoustic diffraction," *Physical Review Letters,* vol. 76, p. 3546, 1996.

[76] G. Paltauf, H. Schmidt-Kloiber, and M. Frenz, "Photoacoustic waves excited in liquids by fiber-transmitted laser pulses," *The Journal of the Acoustical Society of America,* vol. 104, pp. 890-897, 1998.

[77] T. Lee, J. Ok, L. J. Guo, and H. Baac, "Low f-number photoacoustic lens for tight ultrasonic focusing and free-field micro-cavitation in water," *Applied Physics Letters,* vol. 108, p. 104102, 2016.

[78] D. Cannell, G. Nikolaenko, M. Giglio, A. Vailati, F. Croccolo, and W. Meyer, "Shadowgraph study of gradient driven fluctuations," *Sixth Microgravity Fluid Physics and Transport Phenomena Conference,* vol. 1, pp. 325-344, 2002.

[79] A. J. Hart and A. H. Slocum, "Force output, control of film structure, and microscale shape transfer by carbon nanotube growth under mechanical pressure,," *Nano Letters,* vol. 6, pp. 1254-1260, 2006.

[80] A. L. McKenzie, "Physics of thermal processes in laser-tissue interaction," *Physics in Medicine & Biology,* vol. 35, pp. 1175-1209, 1990.

[81] Z. Su, W. Zhou, and Y. Zhang, "New insight into the soot nanoparticles in a candle flame," *Chemical Communications,* vol. 47, pp. 4700-4702, 2011.

[82] J. Staudenraus, and W. Eisenmenger, "Fibre-optic probe hydrophone for ultrasonic and shock-wave measurements in water," *Ultrasonics,* vol. 31, pp. 267-273, 1993.

[83] V. A. Khokhlova, J. B. Fowlkes, W. W. Roberts, G. R. Schade, Z. Xu, T. D. Khokhlova, T. L. Hall, A. D. Maxwell, T. Wang, and C. A. Cain, "Histotripsy methods in mechanical disintegration of tissue: towards clinical applications," *International Journal of Hyperthermia,* vol. 31, pp. 145-162, 2015.

[84] H. W. Baac, J. G. Ok, T. Lee, and L. J. Guo, "Nano-structural characteristics of carbon nanotube-polymer composite films for high-amplitude optoacoustic generation," *Nanoscale,* vol. 7, pp. 14460-14468, 2015.

[85] H. W. Baac, J. G. Ok, H. J. Park, T. Ling, S. Chen, A. J. Hart, and L. J. Guo, "Carbon nanotube composite optoacoustic transmitters for strong and high frequency ultrasound generation," *Applied Physics Letters,* vol. 97, p. 234104, 2010.

[86] A. R. Williams, D. L. Miller, and D. R. Gross, "Haemolysis in vivo by therapeutic intensities of ultrasound," *Ultrasound in Medicine & Biology,* vol. 12, pp. 501-509, 1986.

[87] M. Canney, V. Khokhlova, J. H. Hwang, T. Khokhlova, M. Bailey, and L. Crum, "Tissue erosion using shock wave heating and millisecond boiling in HIFU fields," *AIP Conference Proceedings,* vol. 1215, p. 36, 2010.

[88] R. Devanagondi, X. Zhang, Z. Xu, K. Ives, A. Levin, H. Gurm, and G.E.Owens, "Hemodynamic and hematologic effects of histotripsy of free-flowing blood: implications for ultrasound-mediated thrombolysis," *Journal of Vascular and Interventional Radiology,* vol. 26, pp. 1559-1565, 2015.

[89] T. L. Hall, C. R. Hempel, K. Wojno, Z. Xu, C. A. Cain, and W. W. Roberts, "Histotripsy of the prostate: dose effects in a chronic canine model," *Urology,* vol. 74, pp. 932-937, 2009.

[90] B. E. Noltingk and E. A. Neppiras, "Cavitation produced by ultrasonics," *Proceedings of the Physical Society. Section B,* vol. 63, pp. 674-685, 1950.

[91] H. Lamb, Hydrodynamics (6th edition), Dover publications, 1945.

[92] H. Poritsky, "The growth or collapse of a spherical bubble or cavity in a viscous fluid," *Proceedings of the first U.S. National Congress of Applied Mathematics,* p. 813, 1952.

[93] E. A. Neppiras, "Acoustic cavitation thresholds and cyclic processes," *Ultrasonic,* vol. 18, p. 201, 1980.

[94] R. E. Apfel, "Acoustic cavitation prediction," *The Journal of the Acoustical Society of America,* vol. 69, p. 1624, 1981.

[95] R. E. Apfel, "Acoustic cavitation," *Methods in Experimental Physics,* vol. 19, pp. 355-411, 1981.

[96] Adam D. Maxwell, Charles A. Cain, Timothy L. Hall, J. Brian Fowlkes, and Zhen Xu, "Probability of cavitation for single ultrasound pulses applied to tissues and tissue-mimicking materials," *Ultrasound in Medicine and Biology,* vol. 39, pp. 449-465, 2013.

[97] Z. Xu, A. Ludomirsky, L. Y. Eun, T. L. Hall, B. C. Tran, J. B. Fowlkes, and C. A. Cain, "Controlled ultrasound tissue erosion," *IEEE Transactions on Ultrasonics, Ferroselectrics, and Frequency Control,* vol. 51, pp. 726-736, 2004.

[98] H. Ju, R. A. Roy, and T. W. Murray, "Gold nanoparticle targeted photoacoustic cavitation for potential deep tissue imaging and therapy," *Biomedical Optics Express,* vol. 4, pp. 66-76, 2013.

[99] B. C. Tran, J. Seo, T. L. Hall, J. B. Fowlkes, and C. A. Cain, "Microbubble-enhanced cavitation for noninvasive ultrasound surgery," *IEEE Transactions on Ultrasonics, Ferroelectrics, and Frequency Control,* vol. 50, pp. 1296-1304, 2003.

[100] H. Cui, T. Zhang, and X. Yang, "Laser-enhanced cavitation during high intensity focused ultrasound: An in vivo study," *Applied Physics Letters,* vol. 102, p. 133702, 2013.

[101] P. W. Power, and J. A. Schoonees, "Understanding background mixture models for foreground segmentation," in *Proceedings Image and Vision Computing New Zealand 2002,* Auckland, 2002.

[102] N. Friedman, and S. Russell, "Image segmentation in video sequences: a probabilistic approach," in *Proceedings of the 13th Conference on Uncertainty in Artificial Intelligence*, Rhode Island, 1997.

[103] R. E. Kumon, C. X. Deng, and X. Wang, "Frequency-domain analysis of photoacoustic imaging data from prostate adenocarcinoma tumors in a murine model," *Ultrasound in Medicine & Biology,* vol. 37, pp. 834-839, 2011.

[104] Y. Yang, S. Wang, C. Tao, X. Wang, and X. Liu, "Photoacoustic tomography of tissue subwavelength microstructure with a narrowband and low frequency system," *Applied Physics Letters,* vol. 101, p. 034105, 2012.

[105] S. Wang, C. Tao, X. Wang, and X. Liu, "Quantitative detection of stochastic microstructure in turbid media by photoacoustic spectral matching," *Physics Letters,* vol. 102, p. 114102, 2013.

[106] G. Xu, I. A. Dar, C. Tao, X. Liu, C. X. Deng, and X. Wang, "Photoacoustic spectrum analysis for microstructure characterization in biological tissue: A feasibility study," *Applied Physics Letters,* vol. 101, p. 221102, 2012.

[107] E. M. Strohm, I. Gorelikov, N. Matsuura, and M. C. Kolios, "Modeling photoacoustic spectral features of micron-sized particles," *Physics in Medicine & Biology,* vol. 59, pp. 5795-5810, 2014.

[108] G. Xu, Z. X. Meng, J. D. Lin, C. X. Deng, P. L. Carson, J. B. Fowlkes, C. Tao, X. Liu, and X. Wang, "High resolution physio-chemical tissue analysis: towards non-invasive in vivo biopsy," *Scientific Reports,* vol. 6, p. 16937, 2016.

[109] M. P. Patterson, C. B. Riley, M. C. Kolios , and W. M. Whelan, "Optoacoustic signal amplitude and frequency spectrum analysis laser heated bovine liver ex vivo," *2011 IEEE International Ultrasonics Symposium (IUS),* pp. 300-303, 2011.

[110] R. K. Saha, and M. C. Kolios, "“A simulation study on photoacoustic signals from red blood cells," *The Journal of the Acoustical Society of America,* vol. 129, pp. 2935-2943, 2011.

[111] M. P. Patterson, C. B. Riley, M. C. Kolios, and W. M. Whelan, "Optoacoustic characterization of prostate cancer in an in vivo transgenic murine model," *Journal of Biomedical Optics,* vol. 19, p. 056008, 2014.

[112] G. Xu, M. C. Davis, J. Siddiqui, S. A. Tomlins, S. Huang, L. P. Kunju, J. T. Wei, and X. Wang, "Quantifying Gleason scores with photoacoustic spectral analysis:feasibility study with human tissues," *Biomedical Optics Express,* vol. 6, pp. 4781-4789, 2015.

[113] E. M. Strohm, E. S. Berndl, and M. C. Kolios, "Probing red blood cell morphology using high-frequency photoacoustics," *Biophysical Journal,* vol. 105, pp. 59-67, 2013.

[114] E. M. Strohm, M. J. Moore, and M. C. Kolios, "Single cell photoacoustic microscopy: a review," *IEEE Journal of Selected Topics in Quantum Electronics,* vol. 22, pp. 1-15, 2016.

[115] J. W. Hunt, M. Arditi, and F. S. Foster, "Ultrasound transducers for pulse-echo medical imaging," *IEEE Transactions on Biomedical Engineering,* vol. 30, pp. 453-481, 1983.

[116] R. E. Davidsen, and S. W. Smith, "Two-dimensional arrays for medical ultrasound using multilayer flexible circuit interconnection," *IEEE Transactions on Ultrasonics, Ferroelectrics, and Frequency,* vol. 45, pp. 338-348, 1998.

[117] F. S. Foster, K. A. Harasiewicz, M. D. Sherar, "A history of medical and biological imaging with polyvinylidene fluoride (PVDF) transducers," *IEEE Transactions on Ultrasonics, Ferroelectrics, and Frequency,* vol. 47, pp. 1363-1371, 2000.

[118] C. Zhang, S.Chen, T. Ling,and L. J. Guo, "Review of imprinted polymer microring as ultrasound detector: fabrication, characterization and applications," *IEEE Sensors Journal,* vol. 15, pp. 3241-3248, 2015.

[119] T. Ling, S. Chen, and L. J. Guo, "Fabrication and characterization of high Q polymer micro-ring resonator and its application as a sensitive ultrasonic detector," *Optics Express*, vol. 19, pp. 861-869, 2011.

[120] Z. Xie, S. Chen, T. Ling, L. J. Guo, P. L. Carson, and X. Wang, "Pure optical photoacoustic microscopy," *Optics Express*, vol. 19, pp. 9027-9034, 2011.

[121] B. Hsieh, S. Chen, T. Ling, L. J. Guo, and P. Li, "All-optical scanhead for ultrasound and photoacoustic dual-modality imaging," *Optics Express,* vol. 20, pp. 1588-1596, 2012.

[122] S. Chen, Y. Chang, C. Zhang, J. Ok, T. Ling, M. T. Mihnev, T. B. Norris, and L. J. Guo, "Efficient real-time detection of terahertz pulse radiation based on photoacoustic conversion by carbon nanotube nanocomposite," *Nature Photonics,* vol. 8, pp. 537-542, 2014.

[123] B. E. Saleh, M. C. Teich, and B. E. Saleh, Fundamentals of Photonics(2nd Edition), Wiley-Interscience, 2007.

[124] G. XU, J. B. FOWLKES, C. TAO, X. LIU, and X. WANG, "Photoacoustic spectrum analysis for microstructure characterization in biological tissue: analytical model," *Ultrasound in Medicine and Biology*, vol. 41, pp. 1473-1480, 2015.

[125] A. H. Gandjbakhche, P. Mills, and P. Snabre, "Light-scattering technique for the study of orientation and deformation of red blood cells in a concentrated suspension," *Applied Optics*, vol. 33, pp. 1070-1078, 1994.

[126] E. M. Strohm, E. Hysi, and M. C. Kolios, "Photoacoustic measurements of single red blood cells," *2012 IEEE International Ultrasonics Symposium (IUS) (IEEE, 2012)*, pp. 1406-1409, 2012.

[127] M. Nakao, T. Nakao, and S. Yamazoe, "Adenosine triphosphate and maintenance of shape of the human red cells," *Nature*, vol. 187, pp. 945-946, 1960.

[128] M. Musielak, "Red blood cell-deformability measurement: review of techniques," *Clinical Hemorheology and Microcirculation*, vol. 42, pp. 47-64, 2009.

[129] Y. Park, C. A. Best, K. Badizadegan, R. R. Dasari, M. S. Feld, T. Kuriabova, M. L. Henle, A. J. Levine, and G. Popescu, "Measurement of red blood cell mechanics during morphological changes," *Proceedings of the National Academy of Sciences of the United States of America*, vol. 107, pp. 6731-6736, 2010.

[130] M. M. Brandão, A. Fontes, M. L. Barjas-Castro, L. C. Barbosa, F. F. Costa, C. L. Cesar, and S. T. Saad, "Optical tweezers for measuring red blood cell elasticity: application to the study of drug response in sickle cell disease," *European Journal of Haematology*, vol. 70, pp. 207-211, 2003.

[131] C. Zhang, H. Subbaraman, Q. Li, Z. Pan, J. Ok, T. Ling, C. Chung, X. Zhang, X. Lin, R. T. Chen, and L. J. Guo, "Printed photonic elements: nanoimprinting and beyond," *Journal of Materials Chemistry C*, vol. 4, pp. 5133-5153, 2016.

[132] I. Toytman, A. Silbergleit, D. Simanovski, and D. Palanker, "Multifocal laser surgery: Cutting enhancement by hydrodynamic interactions between cavitation bubbles," *Physical Review E,* vol. E, p. 046313, 2010.

[133] T. J. Dubinsky, C. Cuevas, M. K. Dighe, O. Kolokythas and J. Hwang, "High-Intensity Focused Ultrasound: Current Potential and Oncologic Applications," *American Journal of Roentgenology,* vol. 190, pp. 191-199, 2008.

[134] I. Aslam, A. Fleischer, and S. Feldman, "Emerging drugs for the treatment of acne," *Expert Opinion on Emerging Drugs,* vol. 20, pp. 91-101, 2015.

[135] J. C. Vary, "Selected disorders of skin appendages - acne, alopecia, hyperhidrosis," *The Medical Clinics of North America,* vol. 99, pp. 1159-1211, 2015.

[136] K. Bhate, and H. C. Williams, "Epidemiology of acne vulgaris," *The British Journal of Dermatology,* vol. 168, pp. 474-485, 2013.

[137] S. M. Tuchayi, E. Makrantonaki, R. Ganceviciene, C. Dessinioti, S. R. Feldman, C. C. Zouboulis, "Acne vulgaris," *Nature Reviews Disease Primers,* vol. 1, p. 15029, 2015.

[138] R. J. Hay, N. E. Johns, H. C. Williams, I. W. Bolliger, R.P. Dellavalle, D. J. Margolis, R. Marks, L. Naldi, M.A. Weinstock, S.K. Wulf, C. Michaud, C. Murray, M. Naghavi, "The global burden of skin disease in 2010: An analysis of

the prevalence and impact of skin conditions," *The Journal of Investigative Dermatology,* vol. 134, pp. 1527-1534, 2013.

[139] M. Mujadzic, E. F. Ritter, K. S. Given, "A Novel Approach for the Treatment of Spider Veins," *Aesthetic Surgery Journal,* vol. 35, pp. 221-229, 2015.

[140] Pe'er, Jacob, Singh, Arun D., Clinical Ophthalmic Oncology [electronic resource] : Eyelid and Conjunctival Tumors, Berlin: Springer Berlin Heidelberg, 2014.

[141] F. Meurens, A. Summerfield, H. Nauwynck, L. Saif, and V. Gerdts, "The pig: a model for human infectious diseases," *Trends in Microbiology,* vol. 20, pp. 50-57, 2012.

[142] D. A. Kumar, and A. Agarwal, "Sub-1 Millimeter—700 Micron Cataract Surgery," *US Ophthalmic Review,* vol. 4, pp. 92-96, 2011.

[143] J. Park, T. Kim, D. Stryakhilev, J. Lee, S. An, Y. Pyo, D. Lee, Y. Mo, D. Jin, and H. Chung, "Flexible full color organic light-emitting diode display on polyimide plastic substrate driven by amorphous indium gallium zinc oxide thin-film transistors," *Applied Physics Letters,* vol. 95, p. 013503, 2009.

[144] P. Maury, D.Turkenburg, N. Stroeks, P. Giesen, I. Barbu, E. Meinders, A. van Bremen, N. Iosad, R. van der Werf, and H.Onvlee, "Roll-to-roll UV imprint lithography for flexible electronics," *Microelectronic Engineering,* vol. 88, pp. 2052-2055, 2011.

[145] D. Shavit, "The developments of LEDs and SMD Electronics on transparent conductive Polyester film," *Vacuum, International,* 2007.

[146] B. J. de Gans, P. C. Duineveld, and U. S. Schubert, "Inkjet Printing of Polymers: State of the Art and Future Developments," *Advanced Materials,,* vol. 16, pp. 203-213, 2004.

[147] S. Mandal, G. Purohit, and M. Katiyar, "Inkjet Printed Organic Thin Film Transistors: Achievements and Challenges," *Materials Science Forum,* vol. 736, pp. 250-274, 2012.

[148] H. Lu, J. Lin, N. Wu, S. Nie, Q. Luo, C. Ma, and Z. Cui, "Inkjet printed silver nanowire network as top electrode for semi-transparent organic photovoltaic devices," *Applied Physics Letters,* vol. 106, p. 093302, 2015.

[149] F. Villani, P. Vacca, G. Nenna, O. Valentino, G. Burrasca, T. Fasolino, C. Minarini, and D. della Sala, "Inkjet printed polymer layer on flexible substrate for OLED applications," *The Journal of Physical Chemistry C,* vol. 113, pp. 13398-11402, 2009.

[150] T. Lee, H. Bacc, J. G. Ok, H. Youn, and L. J. Guo, "Nozzle-free liquid micro jetting via homogeneous bubble nucleation," Physical Review Applied, vol. 3, 044007, 2015.